ABSTRACT

Title of Thesis: Measurements of the Size Distribution and Aerodynamic Properties of Soot

Name of degree candidate: Thomas George Cleary

Degree and Year: Master of Science in Chemical Engineering, 1989

Thesis directed by: Dr. James W. Gentry
Professor
Department of Chemical and Nuclear Engineering

The particle size distribution and aerodynamic properties of soot agglomerates formed by the combustion of acetylene is studied. A positive pressure soot generator was constructed which allowed for the characterization of the soot aerosol. Nearly monodisperse particles (10 to 20 nm in diameter) have been observed at low acetylene flow rates. The mean size and width of the distribution are confirmed with a diffusion battery and a differential mobility analyzer. Size distribution measurements of soot agglomerates have been obtained from optical and electron microscopy for a range of acetylene flow rates. The electron microscopy results are compared to model predictions of the cluster size distribution. Friction coefficient measurements from electrical mobility classified agglomerates have been made and are compared to fractal models for clusters. Aerodynamic diameters of impacted agglomerates are related to the geometric mean size form optical microscopy. These results suggest that the geometric mean size can replace the spherical diameter if a particle density of 0.1 g/cc is assumed.

MEASUREMENTS OF THE SIZE DISTRIBUTION AND AERODYNAMIC PROPERTIES OF SOOT

by

Thomas George Cleary

Thesis submitted to the Faculty of the Graduate School
of The University of Maryland in partial fulfillment
of the requirements for the degree of
Master of Science
1989

Advisory Committee:

Professor James W. Gentry, Chairman/Advisor
Professor Richard V. Calabrese
Professor Thomas J. McAvoy

TABLE OF CONTENTS

LIST OF TABLES

LIST OF FIGURES

I. INTRODUCTION

The mechanisms of smoke formation and the physicochemical properties of smoke particles are of interest to investigators in the fields of fire research, fossil fuel energy conversion, environmental science, and military concerns. Smoke toxicity, decreased visibility from light absorption and scattering of smoke, property damage due to particulate deposition, and the thermal radiation from soot particles are some concerns in fire research. The effectiveness of certain smoke detectors depends on smoke properties. On-line measurement of combustion particulates can be part of a control scheme for efficient energy conversion (Burtcher, 1987). Soot from diesel engines affects the engine efficiency and is a health concern (Yu, 1987). Mass fires that would result from a major nuclear exchange could produce enough smoke to change the global climate of the earth (so called nuclear winter scenario (Penner, 1989). This has motivated research on the extent of light scattering and absorption from soot particles.

Soot agglomerates from flaming combustion characteristically have a tenuous low density structure. Ultra-fine primary particles stick together in a random fashion yielding a chainlike agglomerate. Agglomerates larger than one mm in overall dimensions may be formed. The mechanism of soot formation is complex and not fully understood. The basic steps of soot formation include nucleation, surface growth and coalescence, and agglomeration of small primary particles to form low density structures. Oxidation of particles after they have

formed may also occur. The examination of soot formation in flames is an active area of research (Santoro, 1983, 1987 ; Dobbins, 1987).

This study focuses on measurements of the size distribution and aerodynamic properties of soot particles (primary particles and agglomerates) from a laminar coannular diffusion flame burner. The following paragraphs summarize the major accomplishments of this study.

A positive pressure output soot generator has been designed and constructed which has a stable output for at least an hour. The generator is capable of producing a wide range of mean agglomerate sizes which is controlled by varying the fuel flow rate. It was observed for the first time the steady state generation of nearly mono-size 10-20 nm diameter size particles from a flame system. This observation could be confirmed only for an acetylene flame. The measurement of the particle size distribution has been performed with both a GCAF diffusion battery and a differential mobility classifier. These independent measurements verify the existence of the mono-size particles.

In recent years, there has been quite a bit of progress in terms of modelling the structure, size distribution, and properties of low density agglomerates in terms of fractal concepts. This study represents one of the first studies to quantitatively address the validity of these new concepts as applied to smoke agglomerates. The specific issues addressed include model predictions of the

cluster size distribution, and properties of agglomerates including agglomerate friction coefficients, aerodynamic size, charging, and the effects of agglomerate restructuring.

The structural size distribution has been measured with electron and optical microscopy. The size distribution from electron microscopy is compared to model predictions of the cluster size distribution.

Aerodynamic properties of agglomerates are investigated by comparing the structural size of agglomerates that were inertially classified with a cascade impactor to the aerodynamic size.

Friction coefficient measurements of electrical mobility classified agglomerates were compared to the results of other researchers. These measurements were compared to model predictions of the friction coefficient of fractal agglomerates in free molecular and continuum flow conditions. Measurements of mass equivalent diameters for electrical mobility classified agglomerates were also obtained.

Quantitative measurements have been made on the effects the restructuring of agglomerates has on the aerodynamic behavior of agglomerates. Increases in the agglomerate's fractal dimension are brought about by the restructuring of the agglomerate in a condensation/evaporation cycle. After restructuring, the

agglomerate's electrical mobility is increased, which corresponds to a decrease in the electrical mobility equivalent diameter.

Measurements of diffusion coefficients of mobility classified agglomerates gives information on the steady state charge level obtained for agglomerates of a given size.

I.1 Fractal Analysis of Agglomerates

The concept of fractals has been applied to characterize the structure of low density agglomerates and aggregates (Samson, 1987). Mandelbrot (1983) defines the fractal dimension as a cluster property (i.e. perimeter, area, volume) which has a Hausdorff-Besicovitch dimension which is not an integer. The Hausdorff-Besicovitch (H-B) dimension is determined from the relationship

$$N = (L)^{-Df} \qquad (I.1)$$

where N is the number of line segments of length L in one dimension required to cover the entire set of points of a cluster, Df is the fractal (H-B) dimension. For two and three dimensional sets, N is the number of circles or spheres of radius L needed to cover the set. The fractal dimension of a fractal object will always be less than the Euclidean dimension.

For clusters, the scaling property observed is usually a power law relationship between the mass of a cluster and a measure of

cluster size. Samson (1987) detailed the measurement of fractal dimensions of soot agglomerates. The soot agglomerates are made up of spherules with a fairly narrow primary particle size range and a mean primary particle diameter around 30 nm. For clusters made up of 5 to 200 primary particles, Samson observed a power law relationship between the number of primaries in a cluster and the overall size of the cluster. This relationship is expressed as

$$N_p = k\, R^{Df} \qquad (I.2)$$

N_p is the number of primary particles in the cluster, and R is the size of the cluster, either the radius of gyration or a geometric mean size given by the square root of the overall length times the width. Df is the fractal dimension, and k is a constant of proportionality. In this case Samson obtains the fractal dimension of a two dimensional (2-D) projection (from electron micrographs) of the agglomerate. A log-log plot of the number of primary particles in each cluster versus the radius of gyration or geometric mean size is fitted to a straight line. The slope is equal to the fractal dimension and the intercept is the constant of proportionality. It has been argued that some 2-D and 3-D fractal dimensions are the same. Mandelbrot proposes that a true 3-D fractal object with $Df < 2.0$ is transparent, which means upon viewing a 2-D projection all particles in a cluster are visible (no particles are screened by other particles). It is believed that little overlap in mass occurs upon projection of soot agglomerates. The fractal dimensions Samson reported are 1.61 for the geometric

mean size and 1.49 for the radius of gyration. Since the acetylene burner used in this and Samson's study is the same, Samson's results on the power law relationship for the agglomerates will be used here.

I.2 Aerodynamic Behavior of Aerosol Particles

The particle equation of motion is given by

$$m \frac{d\mathbf{v}}{dt} = -\mathbf{v}\, B - \Sigma \mathbf{F}_i \qquad (I.3)$$

where m is the particle mass, $\mathbf{v}$ is the particle velocity relative to the fluid velocity, B is the particle mobility, and $\mathbf{F}_i$'s are external forces. External forces include gravitational and electrical forces. Drag force is given by the particle mobility times the velocity, Stokes law for the drag force can be used for spheres when non-continuum effects of the fluid can be ignored. The drag force is not considered an external force. Particle-particle interactions can usually be ignored.

The Stokes-Einstein equation for particle diffusion is

$$D = \frac{k\ T\ C}{3\ \pi\ \eta\ dp} \qquad (I.4)$$

where D is the particle diffusion coefficient, T is absolute temperature, C is the Cunningham slip correction factor, η is the

fluid viscosity and dp is the particle diameter. For a spherical particle, the particle mobility is given by

$$B = \frac{C}{3 \pi \eta \, dp} \tag{I.5}$$

The particle mobility is related to the fluid drag. The Cunningham slip correction factor is an empirical correction factor which takes into account the non-continuous behavior of the resisting fluid as the particle diameter approaches molecular sizes. The relationship between the particle diameter, mean free path of the carrier gas, and the Cunningham slip correction factor is

$$C = 1 + \frac{2.51 \lambda}{dp} + \frac{0.87 \lambda}{dp} \exp\left\{ \frac{-0.44 \, dp}{\lambda} \right\} \tag{I.6}$$

where λ is the mean free path of the gas molecules.

Charged particles in an electric field experience an electrical force. In a constant electric field, the steady relative velocity a particle reaches is given by

$$v_x / E_x = q \, n \, B \tag{I.7}$$

E_x is the component of the electric field, q is the elementary charge of an electron which may be positive or negative, and n is the number of charges. Information on particle size and charge can be determined by examination of the particle drift velocity in an

electric field. v_x/E_x is called the electrical mobility (Z_p) of the particle.

When an air stream carrying particles changes direction suddenly, the inertia of the particles tends to carry the particles along the original path. The distance the particles travel in the original direction is given by the stopping distance of the particle. The stopping distance (x) is defined as

$$x = v_{x0}/\tau \qquad (I.8)$$

v_{x0} is the original velocity, and τ is the particle relaxation time which is given by the product of the particle mass and mobility (B).

A cascade impactor separates particles according to their inertial properties. Gravitational settling is also related to the particle relaxation time.

For spherical particles, Stokes law with the Cunningham slip correction factor adequately predicts the frictional resistance. Problems arise when trying to describe the aerodynamic properties of non-spherical particles. It would be useful to relate the measurements from diffusion batteries, electrostatic classifiers, cascade impactors and other instruments to the structure of non-spherical particles.

Whitlaw-Gray's (1932) experimental work with metallic smokes pointed out that the apparent density of smokes can be much less than the true density of the material that makes up the smoke. The experiment consisted of measuring settling and rise velocity of particles in an electric field. For example, gold aerosol particles produced by vaporization of gold in an electric arc seem to have apparent densities of 0.2-8.0 g/cc versus 19.3 g/cc for solid gold. The apparent density depends on how the primary particles in a cluster arrange. Compact, isometric structures have aerodynamic properties close to those of the volume equivalent diameter, while aerodynamic properties of chainlike agglomerates are much different than those of the volume equivalent diameter.

Fuchs (1964) defined the dynamic shape factor (k) of a non-spherical particle as the ratio of frictional drag of the non-spherical particle to that of a spherical particle having the same volume.

$$\frac{F_D \text{ non-spherical}}{F_D \text{ spherical}} = k \qquad \text{(I.9)}$$

The frictional resistance for a non-spherical particle (neglecting non-continuum effects) is

$$F_D = v_x \, k \, / 3 \, \pi \, \eta \quad Dve \qquad \text{(I.10)}$$

Where Dve is the volume equivalent diameter of the particle.

Thus,dynamic shape factors can be calculated for a cluster if the cluster volume and frictional resistance is known.

Whitby and Vomela (1967) measured the electrical mobilities of copper oxide (mean primary particle diameter $\bar{d}p = 0.042$ μm and $\sigma_g = 1.3$) and smoke ($\bar{d}p = 0.032$ μm and $\sigma_g = 1.44$) chain agglomerates. For each agglomerate, an electrical mobility equivalent diameter with a slip correction based on that diameter was calculated. Their conclusion was that the electrical mobility equivalent diameter is approximately equal to the volume equivalent diameter of the agglomerate (over the range of 3 to 300 primary particles per cluster). The effects of an increase in surface area of a non-spherical particle is offset by a larger slip correction which tends to keep drag force constant for particles of this volume. This result may only hold for electrical mobility measurements because it has been observed that linear chains of particles tend to align along the longest axis in an electric field.

Odumade (1983) measured electrical mobilities of propane smoke particles with a differential mobility analyzer (DMA). Analysis of individual particles from electron microscopy yielded: the number of primary particles, volume mean diameter of the primaries, the volume equivalent diameter, and the net charge on the clusters. The data set consisted of 25 different particles with electrical mobility equivalent diameters ranging from 0.10 to 0.15 μm. Dynamic shape factors were calculated for each agglomerate. The results were fitted to an equation for the dynamic shape factor as a function of

the net charge, volume equivalent diameter, electrical mobility, number mean primary size, volume mean primary size, the number of primaries, and a slip correction based on the volume equivalent diameter of the agglomerate. His simplified equation for the prediction of the electrical mobility of a cluster is

$$Z_p = \frac{4.50 \times 10^{-6} \; p}{DPN^{1.836} \; N_p^{0.620} \; k} \qquad (I.11)$$

DPN is the number mean primary particle diameter, p is the number of charges, Np is the number of primaries, and k is the dynamic shape factor. This equation can be simplified by substituting in a mean dynamic shape factor of 1.4872. The fit is good, but the useful range is narrow.

Kops et.al. (1977) measured the aerodynamic diameters of iron oxide and gold aggregates composed of up to one hundred thousand primary particles with an inertial spectrometer. The aerosols were produced by an exploding wire. The aerodynamic diameter is related to the particle settling velocity. The definition of aerodynamic diameter is, the diameter of a unit density sphere with the same terminal settling velocity as the non-spherical particle. The relationships Kops obtains are

$$d_{ae} = a \; N^{1/6} \; d_{1g} \; \exp(2 \; \ln^2(\sigma_{1g})) \qquad (I.12)$$

for "linear" aggregates and

$$d_{ae} = b\ N^{1/3}\ d_{1g}\ \exp(1.5\ \ln^2(\sigma_1{}^g)) \qquad (I.13)$$

for "cluster" aggregates. Where "linear" aggregates contain less than 10,000 primary particles and "cluster aggregates contain over 10,000 primaries. d_{ae} is the aerodynamic diameter, d_{1g} is the number mean primary diameter, σ_{1g} is the geometric standard deviation of the primary particles, and a and b are constants. The range of the aerodynamic diameters is 0.2 to 1.0 μm. This result implies that there is some structural feature that is constant for the two regions. Since Dve^3 is proportional to N, for "linear" aggregates, d_{ae} is proportional to $\sqrt{Dve}$ and for "cluster" aggregates, d_{ae} is proportional to Dve.

Fractal analysis allows one to quantify the structural arrangement of agglomerates, which in turn can be used to examine the relationship between the geometric size and the aerodynamic properties. The fractal dimension ties together the geometric size and the mass or volume of the agglomerate. Models for aerodynamic properties of agglomerates, incorporating the fractal dimension can be compared to measured properties. In terms of simulations, clusters with constant fractal dimensions, which would better represent real agglomerates, can be simulated and used to test theoretical models for aerodynamic properties such as the friction coefficient or aerodynamic diameter.

II. EXPERIMENTAL DESIGN

In order to carry out controlled experiments on a well defined sample of soot agglomerates, a generator capable of producing a uniform, steady stream of particles is required. The generator chosen for this study is a laminar flow coannular diffusion burner. The fuel, which was selected for its high sooting tendencies, is 99.9% pure acetylene. The laminar diffusion flame is very stable in terms of the soot volume fraction output. The flow field in and around the flame is characterized as laminar flow. Fuel and air are not mixed prior to combustion. The main controllable variable in this arrangement is the fuel flow rate which controls the soot volume fraction and the average size of the agglomerates.

A number of instruments are used to characterize the soot output of the generator. Some instrumentation allows for the classification of particles in terms of aerodynamic properties, while other instrumentation is capable of measuring number and mass concentrations of soot particles. The sampling of soot particles is an important aspect in the characterization of representative samples of the soot particles from microscopy. Instrumentation and sampling techniques for microscopy are discussed section II.2.

II.1 Design of the Generator

The soot generator is composed of two main components, the burner and the enclosing chimney. A schematic diagram of the

generator is shown in Figure II.1. The burner is similar in design to the Santoro burner (Santoro, 1983). The main controllable parameters are the fuel, combustion air, and dilution air flow rates. The fuel flows through the center tube and is laminar and fully developed by the time it reaches the end of the tube. The fuel flow rate is controlled by a calibrated rotameter, and is varied from 20 cc/min to 70 cc/min. The air flows through a dispersion section that is packed with 6.4 mm diameter glass beads. The air then flows through a ceramic honeycomb one inch thick with 1 mm square channels. The exiting air flow is laminar and forms a sheath around the exiting fuel. At standard operating conditions, the air flow (controlled with a mass flow meter) is fixed at 44 l/min. This implies an excess air ratio of 176 to 44 for the range of fuel flow rates (20-70 cc/min).

The fuel is ignited with a match and a yellow flame appears above the fuel outlet. The flame is called a diffusion flame since no premixing of fuel and air is allowed before combustion. The oxygen and fuel transport into the combustion zone takes place by diffusion. At acetylene flow rates lower than 39.5 cc/min, no visible soot is emitted from the flame. While at higher fuel flow rates, a thread of soot is visible leaving the flame. This thread thickens with increasing fuel flow.

A chimney is placed over the burner. Samson (1987) used a glass chimney in his study. Here, both a glass chimney and a brass chimney were used. The brass chimney is similar in design to the

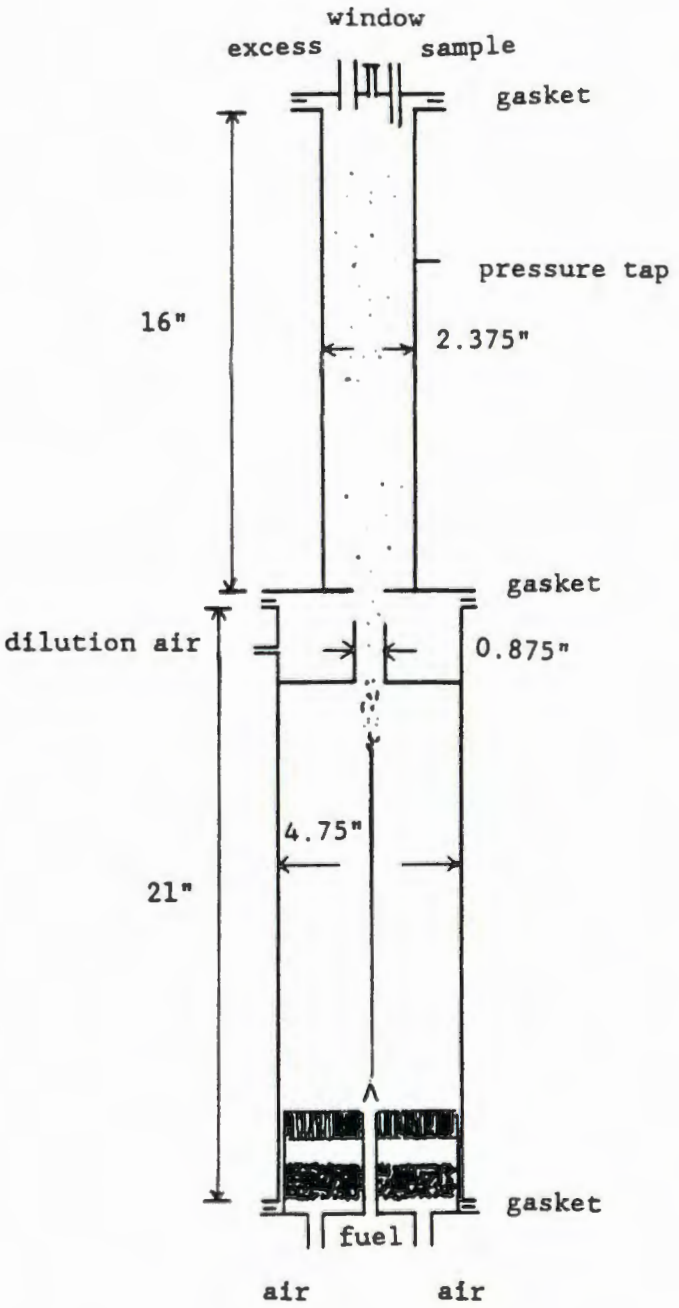

Figure II.1. Schematic diagram of soot generator.

glass chimney. The main difference between the two chimneys is that the brass chimney can be sealed to the burner, so that the burner can operate at a positive pressure (0.02 atm above ambient conditions) without leaking. This allows the burner to produce a constant output aerosol at a positive pressure which is ideal for characterization by standard aerosol instrumentation.

The smoke thread passes straight up the chimney. As it reaches the top of the lower section of the chimney, approximately 41 cm above the fuel exit, there is a constriction. Some recirculation, indicated by wiggling and break up of the thread, occurs here. The smoke passes through the 3/4 inch diameter tube that is approximately 3 inches long and then is mixed with dilution air. The dilution air is fixed at 40 l/min with a rotameter. A 7/8 inch diameter orifice plate causes turbulent mixing of the smoke and dilution air. The smoke is well mixed by the time it reaches the upper section of the chimney. A pressure tap is located in the upper section of the chimney. At the top of the upper section there is a top plate with a main flow outlet, a sample outlet and a viewing port. The main flow outlet is 1/2 inch in diameter and extends 5/8 inches down from the lower surface of the top plate. The sample outlet is 1/4 inch in diameter and extends 1.5 inches down from the lower surface of the top plate. The tube thickness is 1/8 of an inch. At a sampling volumetric flow rate of 1 l/min, the mean velocity in the sampling tube is approximately equal to the mean velocity in the upper section of the chimney. The viewing port is centered on the top plate so that the flame can be visually

monitored. The viewing port is a piece of plexiglass cemented over a small length of tubing that extends through the top plate.

The chimney is constructed from brass. The top plate is bolted to the upper section, upper and lower sections are bolted together, and the whole assembly is bolted to the burner after the fuel is ignited. Rubber gaskets between sections insure an air tight system.

A valve was placed on the main flow outlet so that when measurements are taken the pressure in the upper section can be fixed at 2030 Pa (20 cm water) above ambient pressure.

To summarize, the acetylene flow rate ranged between 20 and 70 cc/min with an overall dilution ratio of 176 to 44 (total air to stoichiometric air). The operating pressure was fixed at 2030 Pa (20 cm water) above ambient pressure.

II.2 Instrumentation

In this section, details on the instrumentation and experimental techniques used in this study are described. A schematic diagram that shows the configurations for all experimental set-ups is shown in Figure II.2. The specifics of certain experiments are explained in detail in following sections.

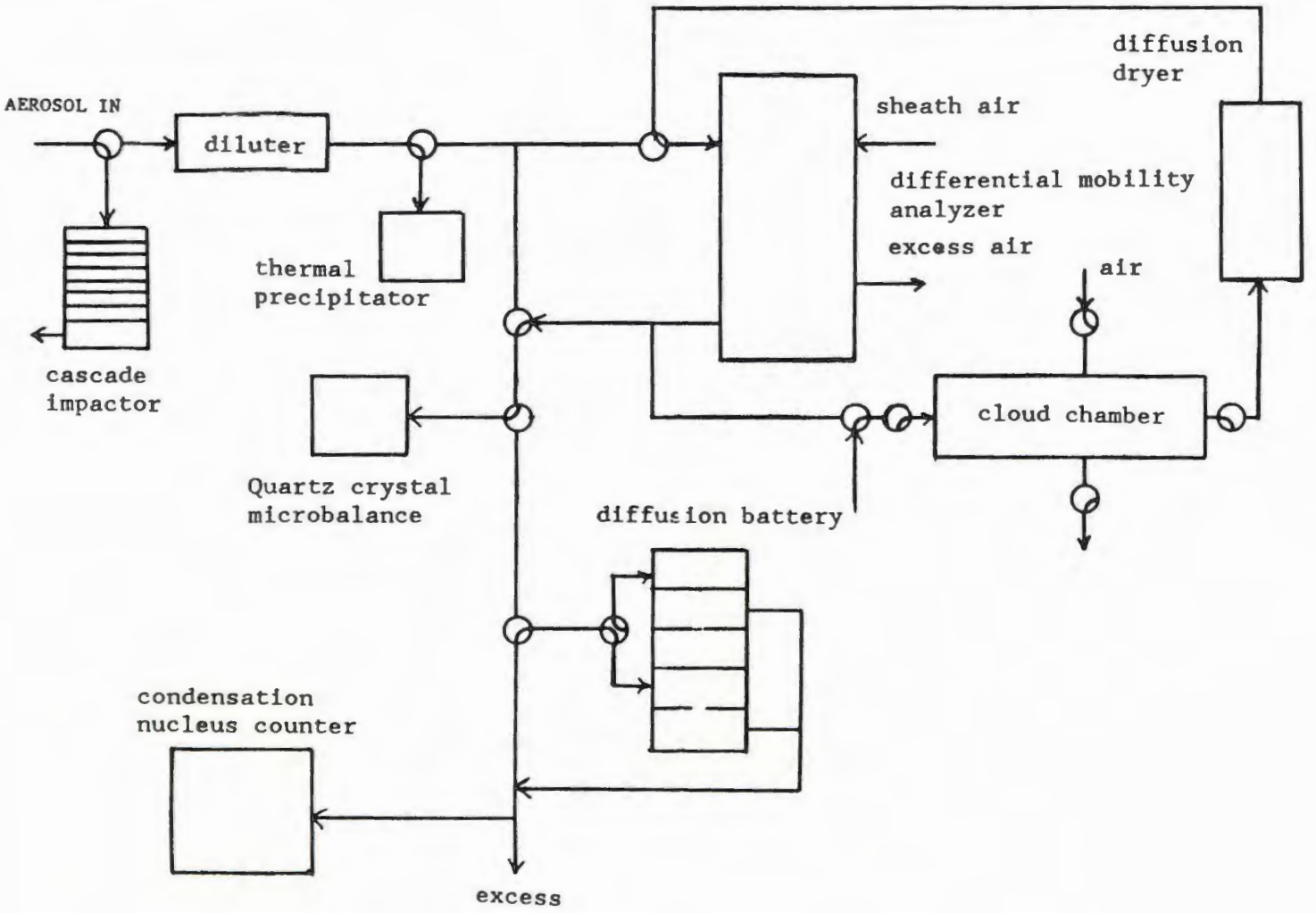

Figure II.2. Schematic diagram of experimental setup.

Generally, it is necessary to further dilute the aerosol stream exiting the soot generator. Thus, down stream from the generator, diluters are located. One type of diluter employed is a porous tube type diluter (Ranade, 1976). Basically, the aerosol flow passes through a porous sintered steel tube. Dilution air is forced through the walls of the tube and joins the aerosol stream. The advantages of this diluter are that a precise dilution ratio can be maintained, and the dilution is performed in such a way as to eliminate problems associated with splitting the aerosol stream. A second type of diluter employed is a pleated membrane filter with a small bypass. This diluter typically yields dilution ratios of 100:1, but the dilution ratio is a function of the flow rate through the diluter and must be calibrated for a given flow rate.

A condensation nuclei counter (CNC) measures the total number concentration of the aerosol stream. The instrument used in this study is a TSI model 3020 continuous flow CNC (Model 3020, TSI, St. Paul, Minn.). The continuous flow rate to the CNC is 0.3 l/min. Basically, the principle concepts of the CNC are as follows. An aerosol stream is introduced into a tube that has been saturated with alcohol vapor. The aerosol stream is then cooled and the alcohol vapor condenses on the particles. The final droplet size is nearly independent of the initial particle size. The particle number concentration is related to the light scattering from these nearly constant size droplets. Concentrations as high as high as 10^5 particles/cc can be measured.

cascade impactor and the collection time. The flow rate to the cascade impactor is 28.3 cc/min.

The cascade impactor classifies particles in terms of their aerodynamic diameter (diameter of a unit density sphere with the same settling time as the given particle). The cascade impactor used in this study is a seven stage model with a backup filter that traps all particles below a minimum size (Model 2000, Anderson, Atlanta, Ga.). The flow rate to the impactor is 28.3 cc/min. A more detailed discussion of the impactor is given in chapter VI.

The differential mobility classifier (DMA) classifies particles according to their electrical mobility. An important feature of this instrument is that the classified particles remain suspended in an exit stream. A schematic diagram of the commercial instrument (Model 3071, TSI, St. Paul, Minn.) is shown in Figure II.3. The controllable variables for the DMA are the sheath air, the aerosol flow, the excess air flow, and the rod voltage. The DMA consists of two sections, a charging section and a classifying section. First, particles are exposed to a high concentration of bipolar ions for a sufficiently long time such that the aerosol obtains a steady state charge distribution. The aerosol then flows between a rod and outer cylinder. Smooth laminar flow of the aerosol and sheath air keeps the streamlines parallel to the axis of the rod. A voltage potential between the rod and the cylinder sets up an electric field. Charged particles with the correct polarity will cross the sheath air streamlines and deposit on the rod. At the bottom of the

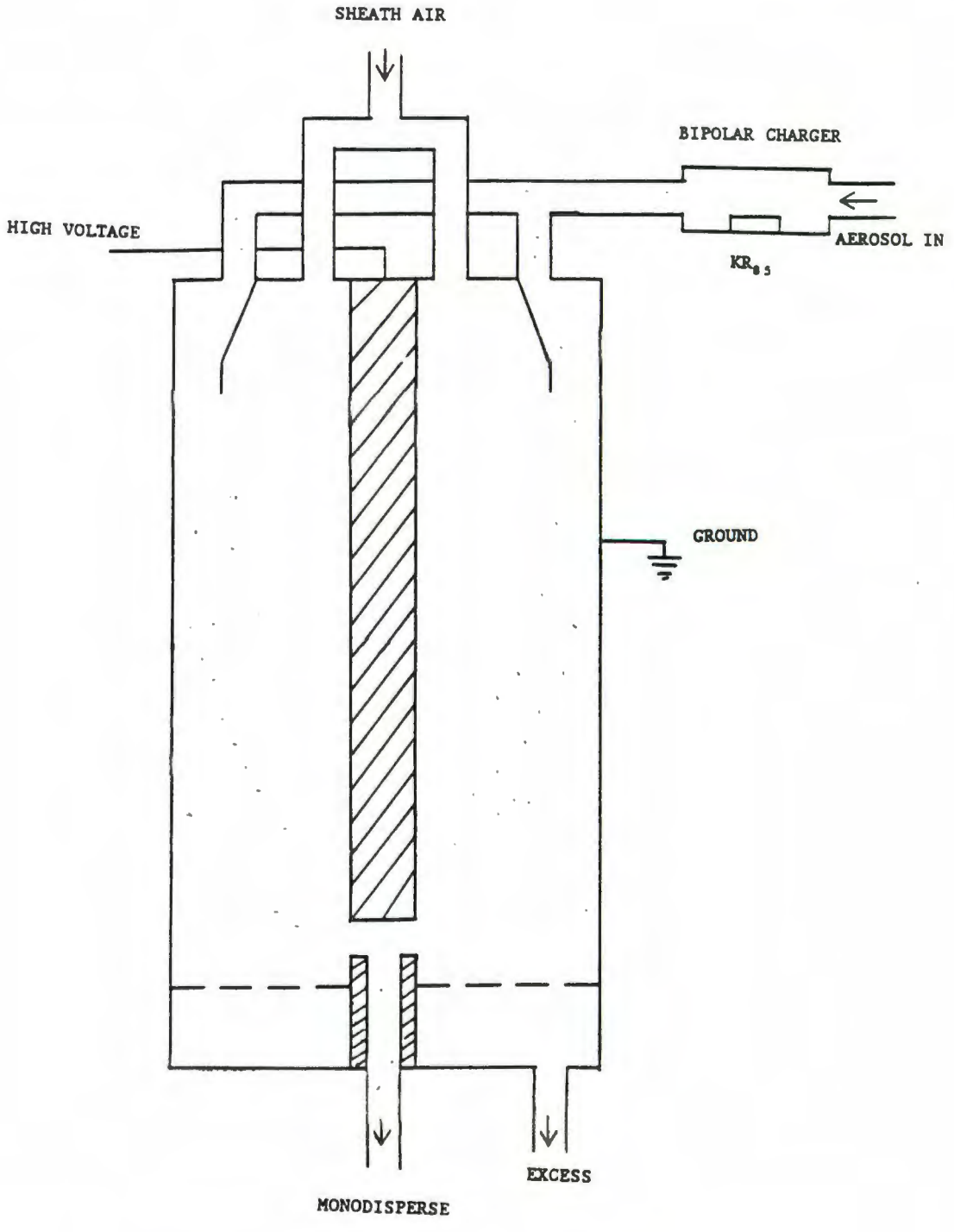

Figure II.3. Schematic diagram of the differential mobility analyzer.

rod is a slot through which aerosol particles with a narrow electrical mobility range are extracted. The electrical mobility is a function of the number of charges on a particle and the particle mobility. The flow rates through the DMA and voltages on the rod will be cited later for the specific experiments.

For an electron microscopy sample, the particles were collected on a transmission electron microscopy (TEM) grid. The TEM grid is approximately 3 mm in diameter, and is made up of fine copper wires running horizontally and vertically. The space between the wires is covered with a carbon film. The distance spanning the wires is on the order of 0.1 mm. For optical microscopy samples, the particles were collected on a glass cover slip.

Two sampling techniques were used to collect particles for microscopy. The first technique is to directly sample the particles from the top of the lower section of the burner. The collection surface is held in the aerosol stream for one second, then removed. This motion is repeated until the proper sample loading is achieved. The particles are drawn to the surface primarily by thermophoretic force, since the collection surface is cooler than the hot air stream that contains the particles. The thermophoretic velocity is almost independent of particle size, so all particle sizes are collected. It is possible that very large clusters impact on the surface which could result in a bias toward the larger sizes. The second technique is to use a thermal precipitator to collect the microscopy sample. A schematic diagram of the precipitator is shown

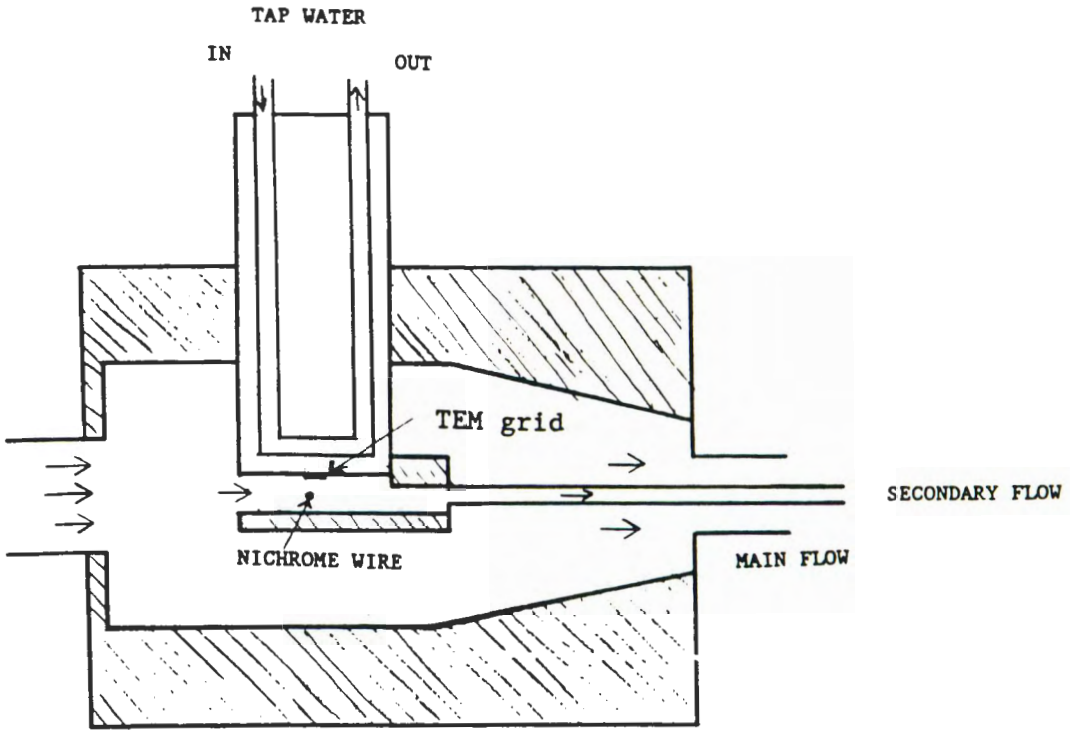

Figure II.4. Schematic diagram of the thermal precipitator.

in Figure II.4. This instrument is based on the design of Small (1987). The thermal precipitator also relies on thermophoresis to draw the particles to the collection surface. The main flow to the thermal precipitator was fixed at 3 l/min. The secondary flow was fixed at 70 cc/min. The secondary flow is exposed to a temperature gradient set up by the nichrome wire which is heated to 100°C, and the brass cylinder which has cold tap water circulating through it. The temperature gradient drives the particles to the cold surface where they are collected. The band of deposited particles is approximately 1 mm wide, and located directly opposite of the nichrome wire. The disadvantage of this arrangement is that it is necessary to pipe the aerosol from the generator. So, larger particles may be lost in the tubing through impaction or sedimentation and small particles by diffusion.

The diffusion battery is a glass capillary array filter (GCAF) tube type battery (Brown, 1984). This type of battery is capable of measuring diffusion coefficients of particles in the size range of 5 to over 100 nm in diameter. Each stage of the diffusion battery contains a glass capillary array except for the blank stage which is used for a reference. The flow enters the stage tangentially to the glass capillary array. The array is positioned at the bottom of the stage sitting on an orifice. The controllable variables are the orifice diameter, the pore diameter, the thickness of the array, and the flow rate through the assembly. The fractional penetration is determined by measuring the ratio of concentrations for the aerosol passing through the array and the blank stage.

III. NUMBER AND MASS CONCENTRATION

The soot generator is capable of producing a relatively stable aerosol stream. The amount of soot produced and the average cluster size can be controlled by the acetylene flow rate. An increase in the acetylene flow rate produces an increase in both the amount of soot produced and the average cluster size. The acetylene flow rate can be adjusted to conditions where no visible soot is seen leaving the flame, to conditions where a dark thread is seen leaving the flame. The flow rate where the soot thread is just visible will be labeled the "visible sooting point". The acetylene flow rate at the visible sooting point is about 39.5 cc/min. It seems that agglomeration continues as the soot travels up the length of the chimney, since at a high fuel flow rate, individual clusters are visible at the top of the lower section on the chimney. After the thread is dispersed and the soot is mixed with the dilution air, the agglomeration is slowed down considerably.

Particle number concentrations are measured by a continuous flow condensation nuclei counter. The background concentration of particles from the generator with the fuel and air flow on, but prior to ignition is less than 5 particles/cc. The number concentration of particles produced by the generator is out of the operating range of the CNC. The particle stream was diluted by a factor of 100 to 1 so that the number concentration was within the operating range of the CNC. The reported values have been corrected

for this dilution. The number concentration was measured for different acetylene flow rates. Over the entire range of acetylene flow rates, (22 to 67.5 cc/min) the number concentration was of the same order of magnitude (approximately 10^6 particles/cc).

In Figure III.1, the particle number concentration is plotted versus the acetylene flow rate. At first there is an increase in the number of countable nuclei as the acetylene flow rate is increased. The number concentration goes through a maximum then decreases rapidly to a slight minimum. The ratio of the maximum to minimum number concentration is approximately 3.5, with the ratio of the acetylene flow rates approximately 1.25. The number concentration then slowly increases as the fuel flow rate increases. There is a 20% increase in number concentration for a corresponding increase in the acetylene flow rate of 75%.

The mass concentration was measured with the microbalance at low concentrations (low fuel flow rates). It is estimated that the uncertainty of the mass concentration measurement is about to ± 25%. Because of the low concentration of the soot particles. At high concentrations, the mass concentration was obtained from the total net weight of particles deposited on the various stages of the cascade impactor and the sampling flow rate and time. The flow uncertainty limits the accuracy of the mass concentration measurements to about ± 10%.

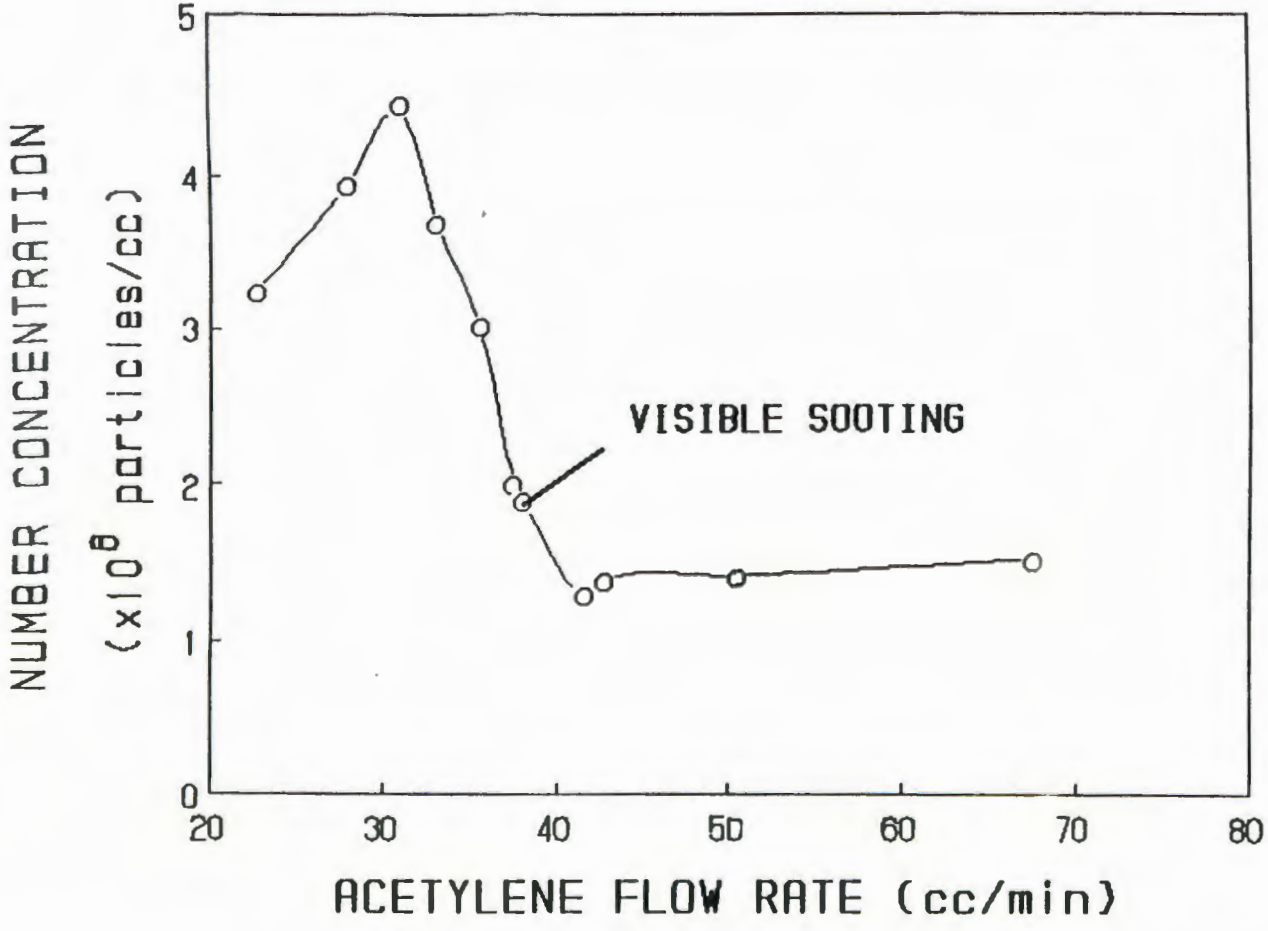

Figure III.1. Number concentration from the CNC versus the acetylene flow rate.

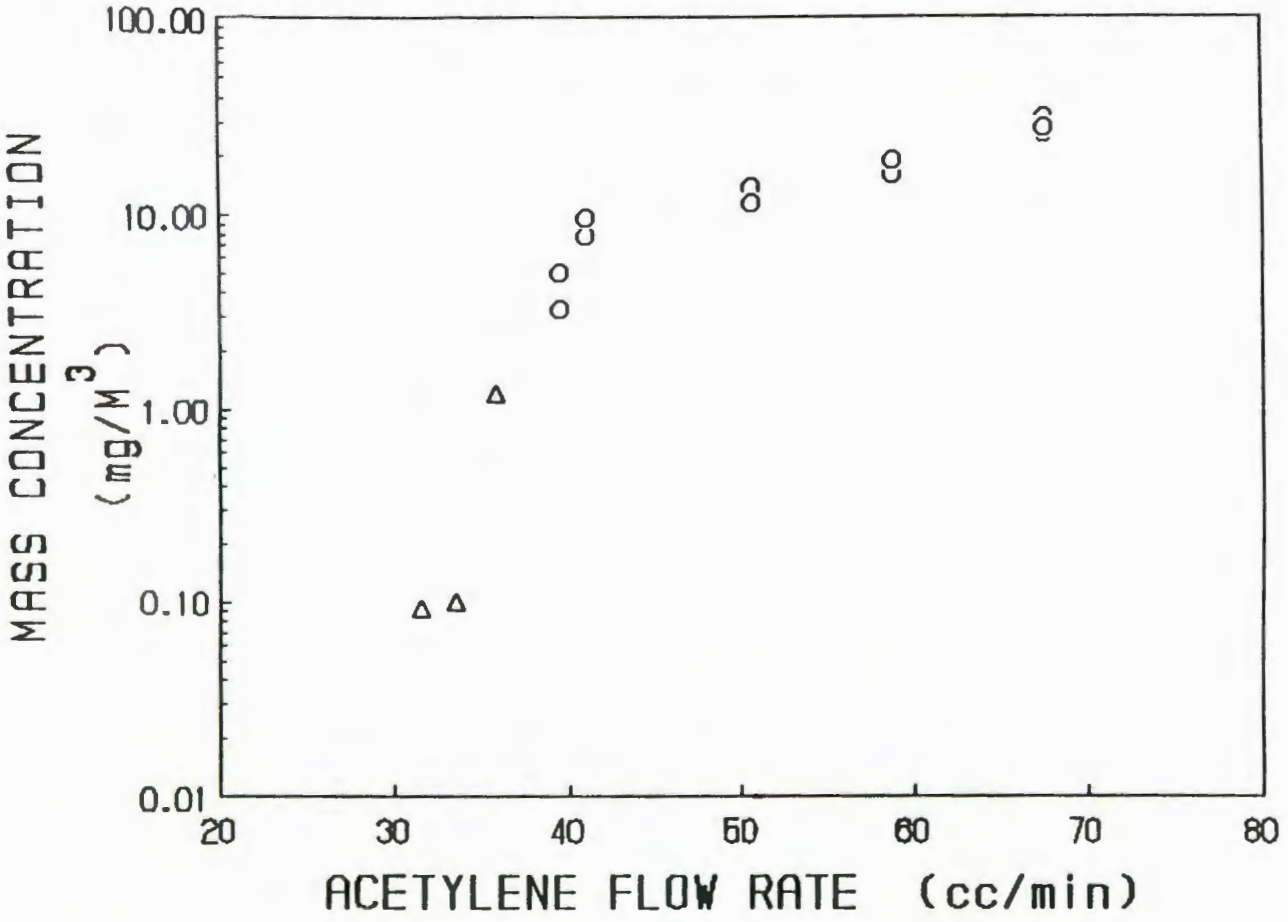

Figure III.2. Mass concentration versus the acetylene flow rate (circles indicate glass fiber filter deposits, triangles indicate microbalance measurements).

Figure III.2 is a plot of the mass concentration of the soot as a function of acetylene flow rate. At low acetylene flow rates, the mass concentration is very low. A sharp increase in soot production is observed as the acetylene flow rate is increased from 34 to 42 cc/min. Soot production increases as the fuel flow rate increases from 42 to 70 cc/min, but at a rate much lower than the rate observed between 34 and 42 cc/min.

It is of interest to express the mass concentration data as soot yield. The soot yield is the mass of soot produced per unit mass of fuel burned. Figure III.3 is a plot of the soot yield versus the acetylene flow rate. Soot yield gives an indication of the burning efficiency of the fuel. The variation of soot yield about the mean value for a given fuel flow rate is less than 15% for most values, with sampling times varying from 2.5 to 60 minutes. This result shows the that the soot emission is fairly stable for a given fuel flow rate.

Figures III.1 and III.2 together indicate that there is particle growth occurring. At fuel flow rates between 34 and 42 cc/min, the number concentration decreases rapidly while the mass concentration increases rapidly. These observations are consistent with particle growth and coagulation increasing the average size of the soot particles while decreasing the number concentration. At the high fuel flow rates, the number concentration is almost constant, only slightly increasing, while the mass concentration is still increasing. These observations are consistent with higher initial

particle concentrations and particle growth and agglomeration accounting for increases in the average size.

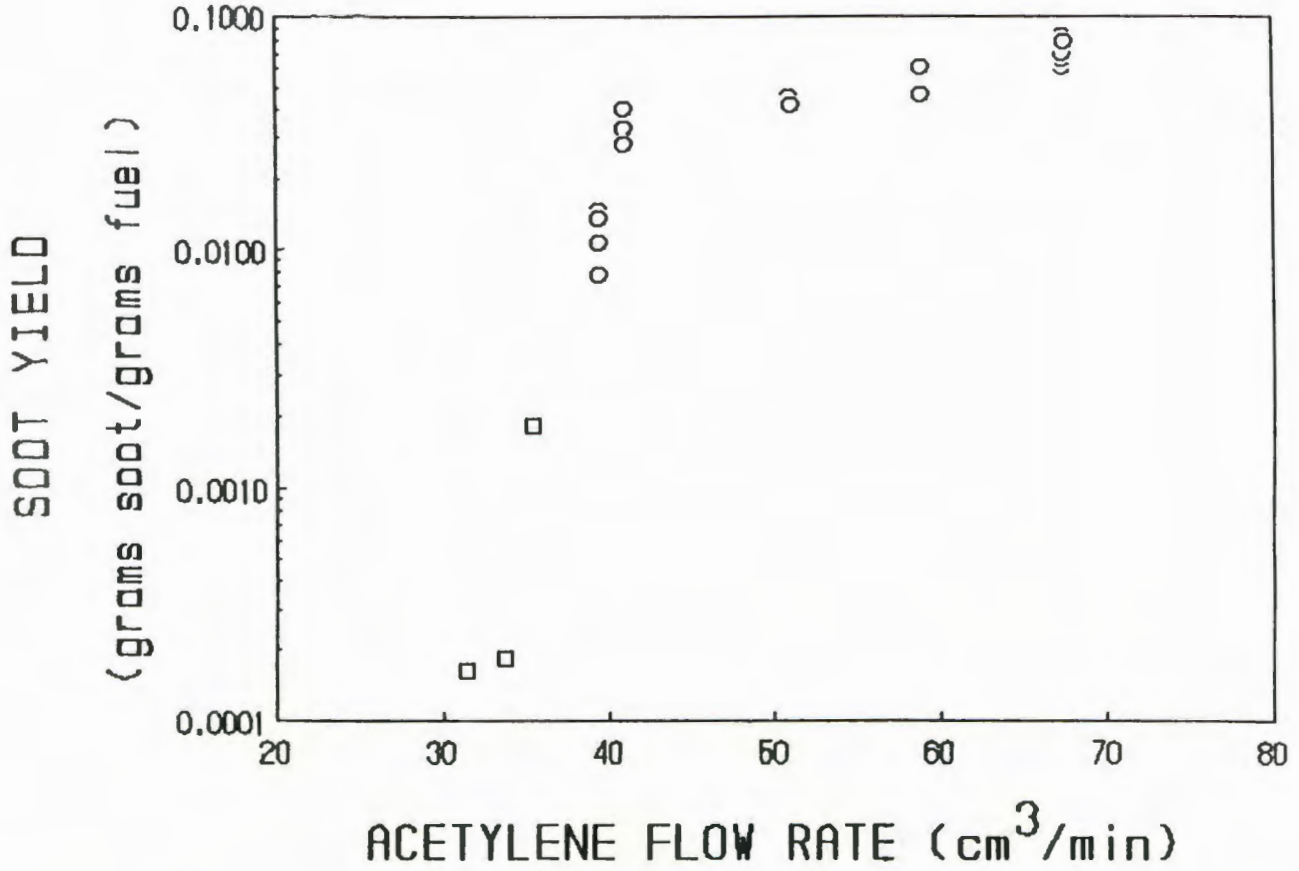

Figure III.3. Soot yield versus the acetylene flow rate (circles indicate glass fiber filter deposits, triangles indicate microbalance measurements).

IV. DIFFUSION COEFFICIENT MEASUREMENTS

For small spherical particles, the diffusion coefficient can be related to particle size through the Stokes-Einstein equation (I.4). In this chapter, diffusion coefficient measurements are related to the size distribution of particles formed at acetylene flow rates below the visible sooting point (less than 39.5 cc/min). These mean diffusion coefficients correspond to spherical particle sizes ranging from 10 to 17 nm for different acetylene flow rates and experimental designs.

Diffusion coefficients of ultra-fine aerosols can be obtained by measuring the penetration through a cylindrical tube. For laminar flow through cylindrical tubes, the penetration is a function of the inverse Peclet number, where the Peclet number is the ratio of the convective forces to forces due to random thermal motion (diffusivity). The fractional penetration is defined as the ratio of the number concentration after and before the diffusion battery. Gormley and Kennedy (1949) give the following asymptotic solution for penetration as a function of inverse Peclet number assuming laminar, fully developed parabolic flow in circular tubes. Only losses due to diffusion to the tube walls is considered. The expressions are

$$Pt = 0.819\exp(-3.65\phi)+0.097\exp(-22.3\phi)+0.035\exp(-57\phi) \quad \phi>0.04 \qquad (IV.1)$$

$$Pt = 1 - 2.56\,\phi^{2/3} + 1.2\,\phi + 0.177\,\phi^{4/3} \quad \phi<0.04 \qquad (IV.2)$$

$$\phi = \frac{\pi N D L}{Q} \qquad \text{(IV.3)}$$

ϕ is the inverse of the Peclet number, N is the number of tubes, L is tube length, and Q is the total flow rate. For monodisperse aerosols, D is obtained by iteratively solving for ϕ with either equation IV.1 or IV.2 then solving for D from equation IV.3. When the aerosol is polydisperse, the data analysis is more complicated.

The physical parameters of the GCAF used as stages in the diffusion battery are, the pore diameter, pore shape, pore length, and porosity. Though the pore size for each diffusion battery stage (GCAF) is fairly uniform and is assumed to be equal to the stated nominal value quoted by the manufacturer, the number of pores or porosity is uncertain. For most cases, the length of a pore is sufficiently long such that the velocity profile at standard operating flow rates is estimated to be a fully developed parabolic profile (Brown, 1985). Thus, the Hagen-Poiseulle equation can be used to confirm the actual number of capillaries for a given GCAF.

$$Q = \pi N (P_1 - P_0) R^4 / 8 \eta L \qquad \text{(IV.4)}$$

Q is the total flow rate, N is the number of capillaries, $(P_1 - P_0)$ is the pressure drop across the stage, R is the pore radius, and L is the capillary length. The measurement of the pressure drop was

performed for each stage at specific flow rates and the number of pores for a given stage was determined. With N determined, the inverse Peclet number can be determined from equation IV.3.

Inversion algorithms for diffusion battery data usually require an assumption about the form of the aerosol size distribution. The algorithm used in the following data analysis is the Apparent Size Method (Park, 1980). With this algorithm, the logarithm of the apparent diffusion coefficient (the diffusion coefficient calculated from equations IV.1 or IV.2, and IV.3 assuming a monodisperse source) is plotted against the measured penetration. The area under the smooth curve passing through the data points is equal to the log mean diffusion coefficient. For spherical particles, this is directly related to the log mean diameter by the Stokes-Einstein equation. The variance for the log-normal distribution is proportional to the difference of the log mean diffusion coefficient and the intercept of the penetration curve at penetration equal to one.

The soot produced at acetylene flow rates below the visible sooting point is made up of sufficiently small particle size so that the GCAF diffusion battery can be used to examine the size distribution. The soot from the generator is diluted, then passes to the diffusion battery, then to the CNC. The CNC requires a constant 0.3 l/min of aerosol flow, so this sets the minimum flow rate through any stage of the diffusion battery. Flow controllers connected to house vacuum maintained the proper flow rate through

the battery. The four way valve controlled the aerosol flow so that it is shunted through either the diffusion battery stage or the blank stage.

The procedure for measuring penetration was as follows: the number concentration (from the CNC) was measured at a constant flow rate through the blank, then through the selected stage, then through the blank again. The two concentrations through the blank were averaged. The repeated measurement through the blank allows one to determine if a large variation in the number concentration of the source occurred during the measurement sequence, or to correct for a systematic drift in the source concentration. The penetration is computed as the ratio of the number concentration through the test stage normalized with the value through the blank stage.

Measurements were taken with different generators, one with a glass chimney and the other with a brass chimney. The pressure inside the upper section of the brass chimney was 2030 Pa (20 cm water) above atmospheric pressure. Although pressure measurements were not made in the glass chimney, the pressure is assumed to be lower (approximately atmospheric) than the brass chimney due to the larger exhaust opening. All other operating conditions, including, air flow, the dilution flow rate, and acetylene flow rate were the same.

It was observed in both sets of measurements that the apparent diffusion coefficient drops off at high penetrations (Pt greater

than 0.8). Other than this observation, there seems to be no apparent trend in the penetration data. It is expected that the apparent diffusion coefficient will approach a limiting value as the penetration approaches unity. The observed drop off in penetration appears to be a systematic error that occurs at high penetrations. An analysis of the Gormley-Kennedy equations, IV.1 and IV.2, give some insight as to why experimental measurements of the diffusion coefficients at high penetrations are susceptible to large magnifications in random and systematic errors. If the true penetration of an aerosol through a stage of a battery is 80%, a +6% error in the measured penetration would yield a measured value of 85%. The ϕ calculated by equation IV.3 would be underestimated by 35%. This would lead to a 35% underestimation in the apparent diffusion coefficient. On the other hand, a +6% error at 40% penetration leads to 11% underestimation in the diffusion coefficient. Therefore, at high penetrations errors are magnified. The observed error would correspond to an overestimation in the measured penetration. It is not fully understood what is causing this error, but it appears to be systematic. Only one GCAF stage is capable of such high penetrations, but it appears to work well at low penetrations. Only the data points with penetrations ranging from 0 to 80% will be included in the data analysis.

The raw data is presented in Appendix 1. The physical dimensions of the different GCAF stages, including the estimated number of capillaries per stage is also included.

Figures IV.1 and IV.2 are apparent diameter plots for sets of data taken at a fuel flow rate of 31.5 cc/min with the glass and brass burner configuration respectively. The left ordinate is the apparent diffusion coefficient, while the right ordinate is the apparent diameter. The apparent diffusion coefficients are scattered around $2x10^{-4}$ cm^2/sec with the glass burner configuration and $6x10^{-4}$ cm^2/sec with the metal burner configuration. The measurements are consistent with a nearly monodisperse aerosol. For a monodisperse aerosol, the points of the apparent diffusion coefficient should fall on a horizontal line. The dashed line corresponds to hypothetical diffusion coefficient measurements for a monodisperse aerosol with twice the estimated log mean particle volume. This would correspond to a particle diameter 26 % greater than the log mean value. Therefore, the GCAF diffusion battery is sensitive to the particle size.

An estimate of the log mean diffusion coefficient is calculated by averaging the apparent diffusion coefficients over the penetrations range from 0 to 80 %. A 95% confidence level for the measured mean diffusion coefficient is calculated assuming the apparent diffusion coefficients are normally distributed about the mean (from Student's t distribution (Hogg, 1977)). The results indicate a fairly narrow size distribution in each case and log mean diffusion coefficients corresponding to diameters on the order of 11 and 16 nm.

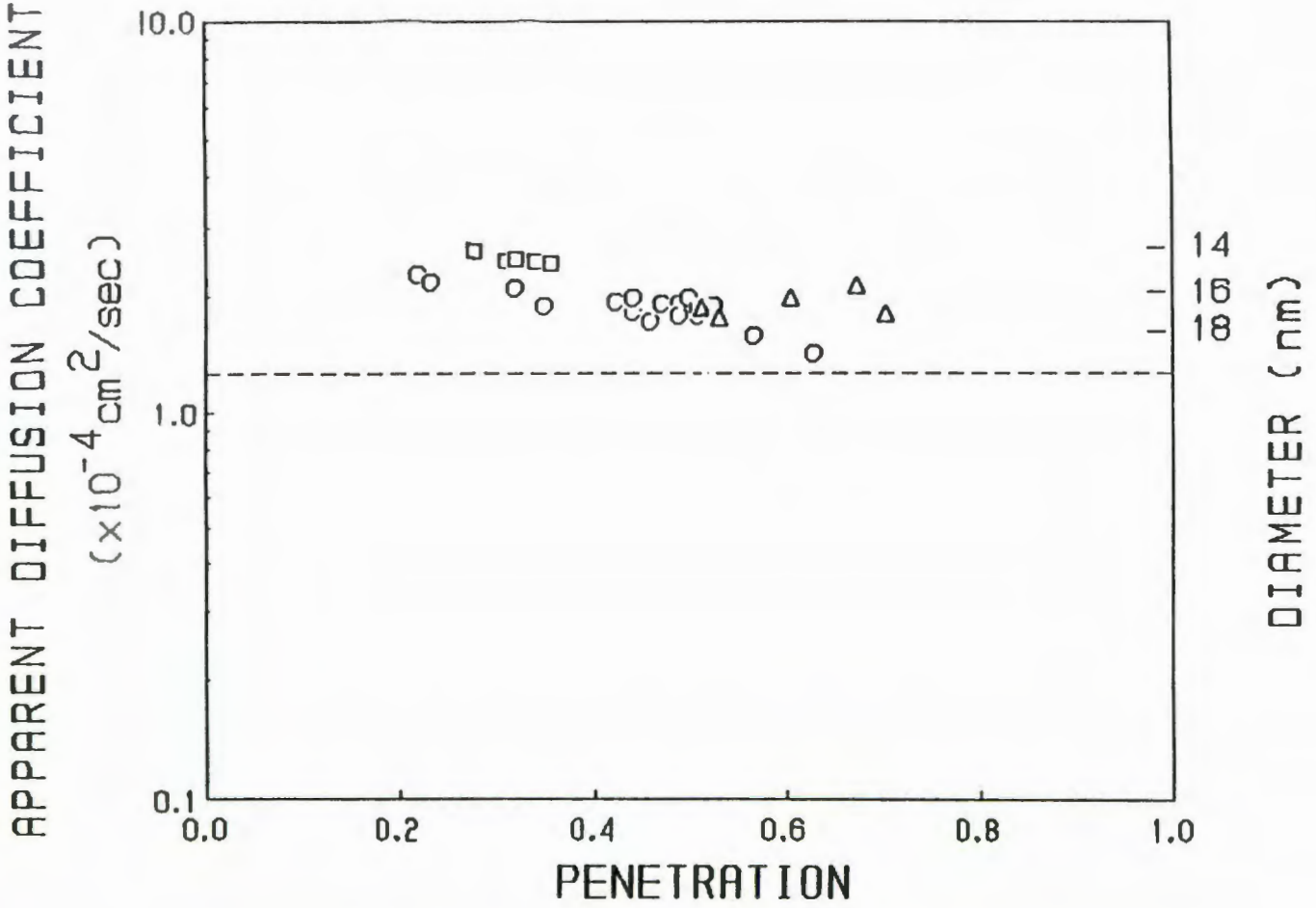

Figure IV.1. Apparent diffusion coefficient versus penetration (glass chimney configuration) with an acetylene flow rate of 31.5 cc/min. The different symbols indicate different diffusion battery stages, the dashed line corresponds to the diffusion coefficient of particles with twice the volume of the mean size.

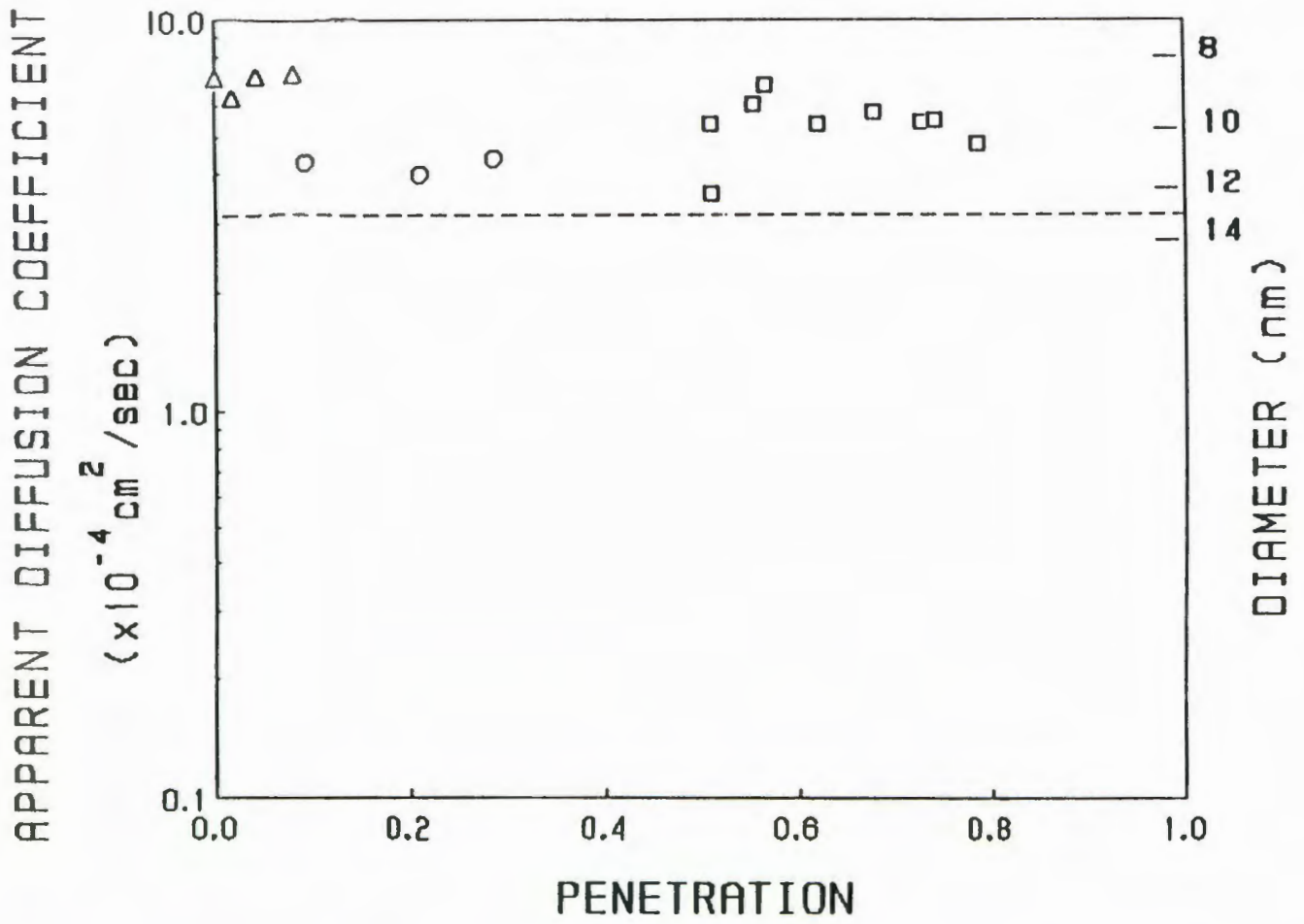

Figure IV.2. Apparent diffusion coefficient versus penetration (brass chimney configuration) with an acetylene flow rate of 31.5 cc/min. The different symbols indicate different stages of the diffusion battery, the dashed line corresponds to the diffusion coefficient of particles with twice the volume of the mean size.

Measurements of the log mean diffusion coefficients at different acetylene flow rates were performed. Plots of the log mean diffusion coefficient versus the acetylene flow rate are shown in Figures II.3 and II.4 for the glass burner configuration and the brass burner configuration respectively. The left ordinate is the mean diffusion coefficient, while the right ordinate is the mean diameter. In the experimental setup with the glass chimney, the mean diffusion coefficients correspond to number mean particle diameters ranging from 15.7 to 17.3 nm. In the experimental setup with the brass burner (at slightly elevated pressure) the number mean particle diameters range from 10.1 to 11.7 nm. It is not understood what causes the difference between the mean sizes for the two cases. There is a slight pressure difference, and the materials of the chimney are also different. Also different acetylene cylinders were used for the two sets of measurements which raises questions about the purity of the different fuels. For either case, it is seen that the mean particle size is only weakly a function of fuel flow rate. These particles appear to be narrowly distributed. The results indicate that increases in the acetylene flow rate (below the visible sooting point) do not increase the mean particle size much.

For such a narrowly distributed aerosol, it is difficult to get an accurate estimation of the geometric standard deviation from the penetration data due to the scatter in the individual values. At this size range, an aerosol with a mean diameter of 10 nm and a geometric standard deviation in terms of diffusion coefficients of

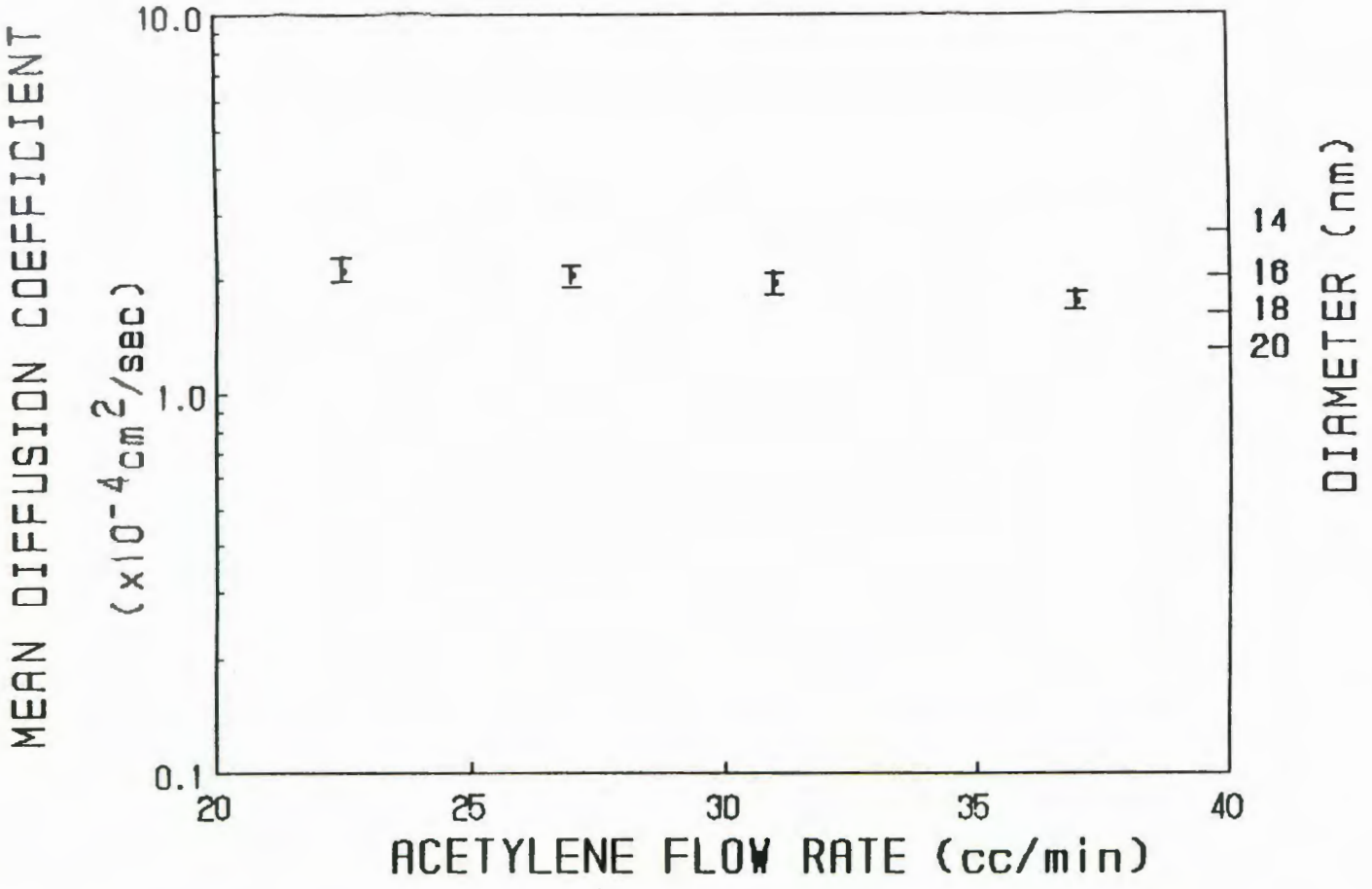

Figure IV.3. Log mean diffusion coefficient versus the acetylene flow rate (glass chimney configuration). Particle diameter is indicated on the right ordinate.

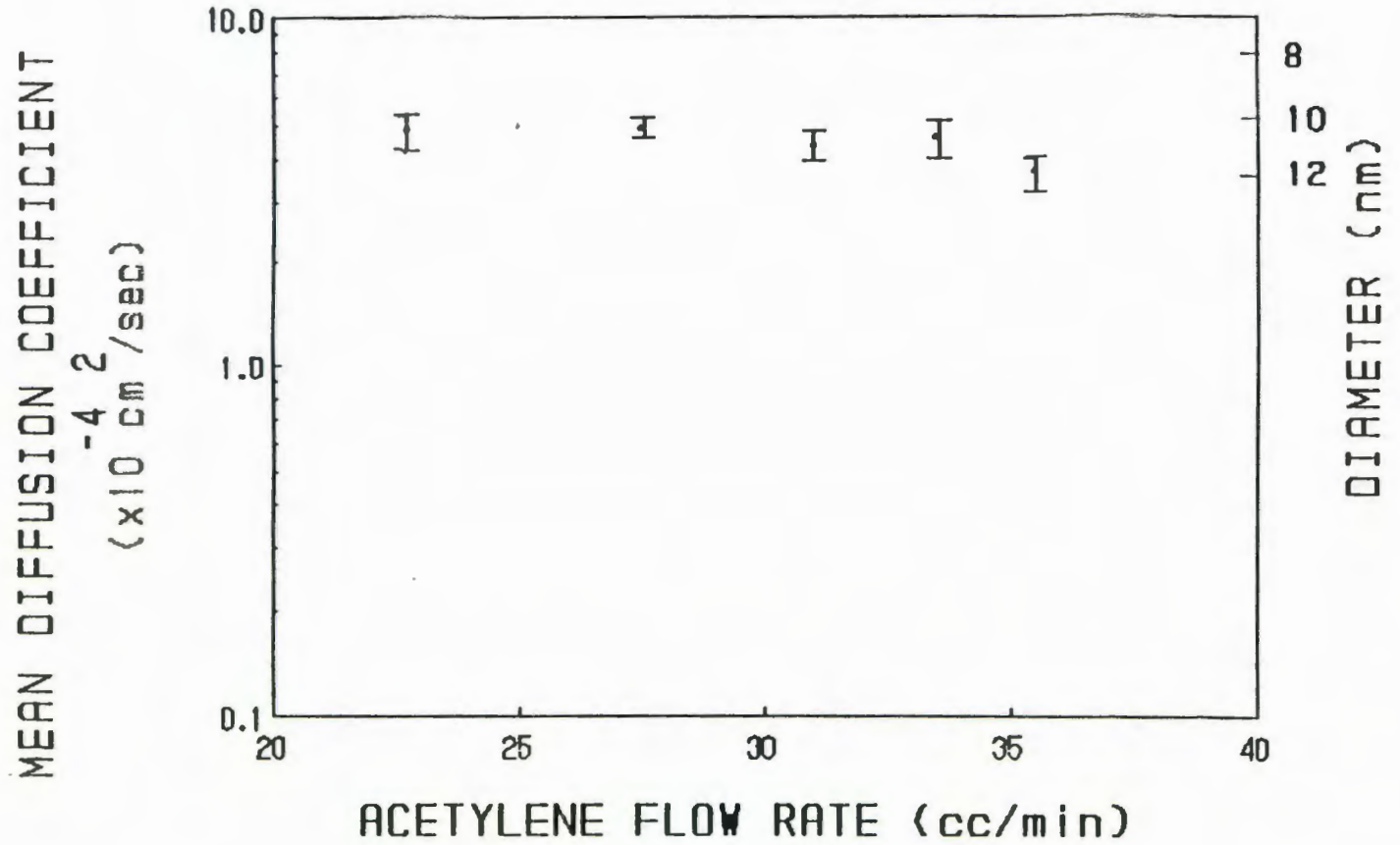

Figure IV.4. Log mean diffusion coefficient versus the acetylene flow rate (brass chimney configuration). Particle diameter is indicated on the right ordinate.

1.14 has an intercept value (at Pt=1.0) of the apparent diffusion coefficient only 0.65% greater than the log mean diffusion coefficient. Figures IV.5 and IV.6 show simulated penetration curves for aerosols with number mean diameters of 10 and 15 nm and σ_g's of 1.14, 1.23, 1.34, and 1.58. At best upper bound on σ_g may be inferred from experimental penetration curves. Here, it is estimated from comparisons of the simulated to the experimental penetration curves that the σ_g's are less than 1.34 for the measured size distribution since there is no discernable trend in the penetration data as Pt approaches 0.

In conclusion, the measurement of the mean particle size was performed with the diffusion battery for particles formed at acetylene flow rates below the visible sooting point. A surprising result is that the particles are present in the first place. This is the first observation of steady state generation of nearly monodisperse 10-20 nm particles from a flaming system. This observation has been confirmed only for an acetylene flame. With other hydrocarbon flames, (i.e. ethylene) the small primary particles formed in the pre-sooting conditions appear to be completely oxidized before they leave the flame zone (Santoro, 1987) (Dobbins, 1987). The observed trend of nearly constant mean particle size with different acetylene flow rates below the sooting point is inconsistent with the formation of clusters. The variation between the two burners points out that the observed mean particle sizes are sensitive to conditions other than fuel flow rate. The reasons for the different measured particle sizes with slightly

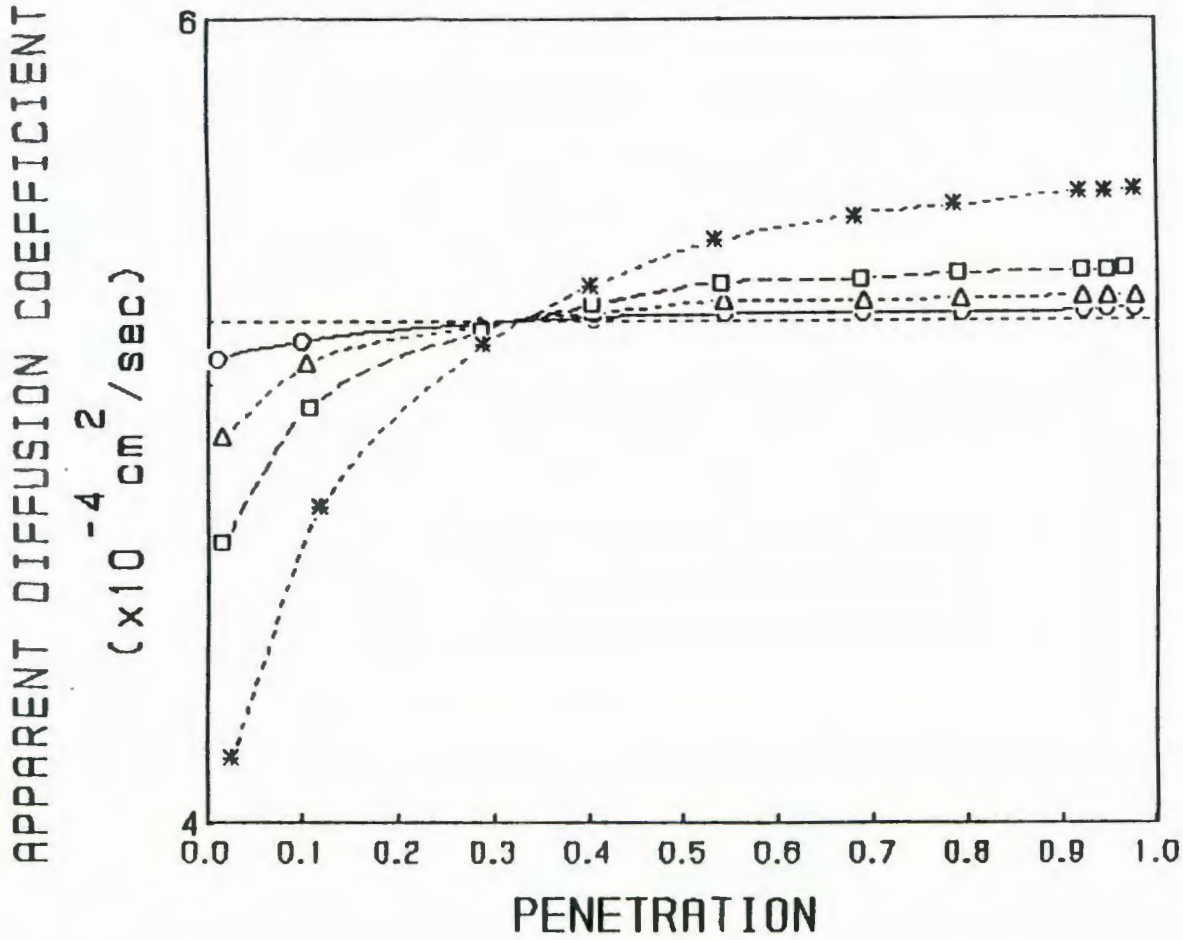

Figure IV.5. Simulated penetration curves of an aerosol with a log mean diameter of 10 nm (σ_g for circles = 1.14, for triangles = 1.23, for squares = 1.34, and for stars = 1.58).

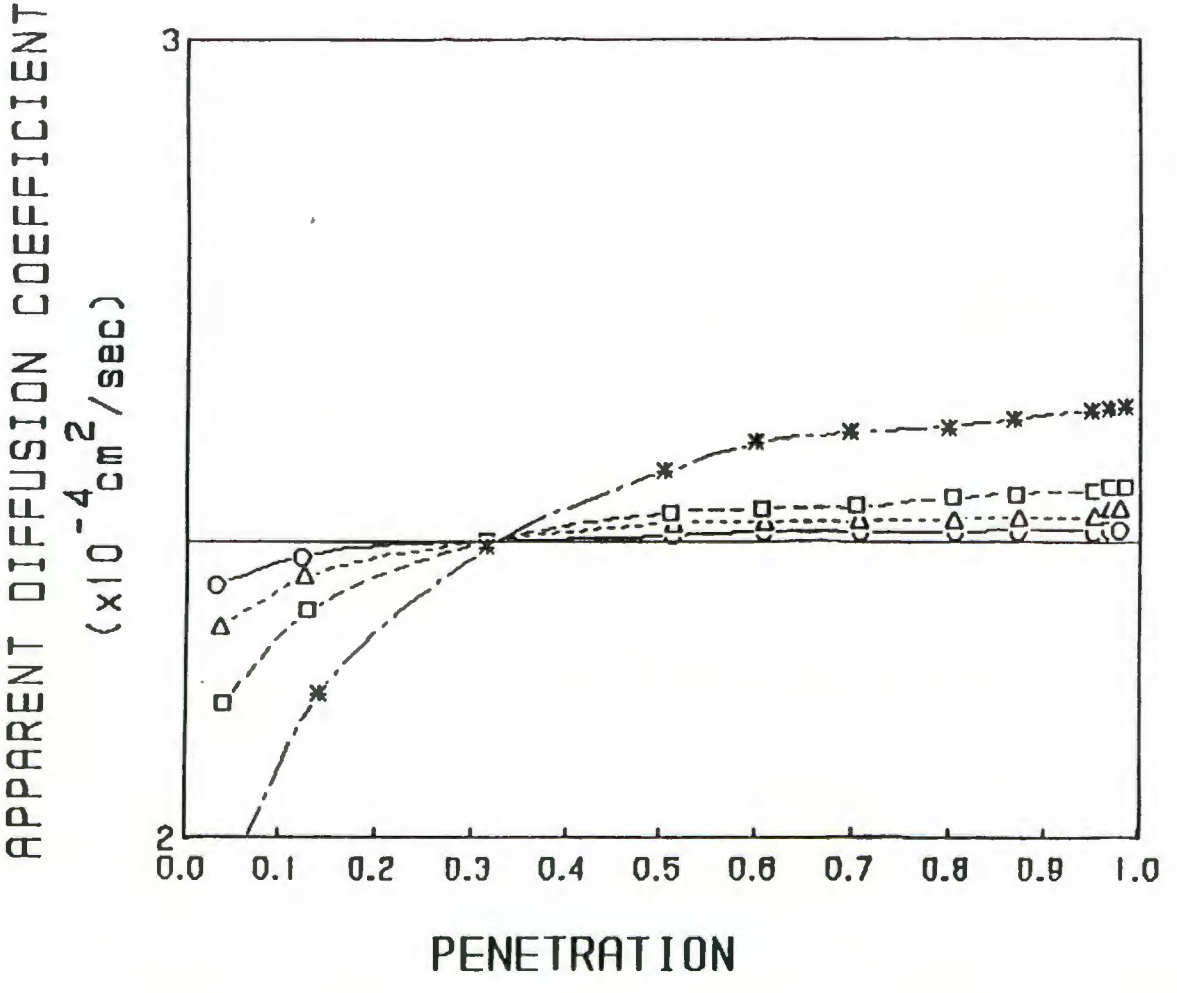

Figure IV.6. Simulated penetration curves of an aerosol with a log mean diameter of 15 nm (σ_g for circles = 1.14, for triangles = 1.23, for squares = 1.34, and for stars = 1.58).

different conditions are not quite clear and it is beyond the scope of this thesis to try to explain the reasons.

V. SIZE DISTRIBUTION

The size distributions of soot agglomerates obtained from microscopy and electrical mobility measurements are presented in this chapter. The data is presented in terms of discrete counts of particles that have sizes that lie in bins of certain size ranges. The size of an agglomerate from microscopy will be presented as a geometric mean of the longest length and width of the agglomerate. This measure of particle size has been shown to be useful in characterizing the fractal dimension of an agglomerate (Samson, 1987). Samson has shown that this size is related to the number of primary particles in an agglomerate through a power law relationship involving the fractal dimension (eq. I.2). Electron microscopy is used to size small agglomerates from a weakly sooting flame (fuel flow rate 39.5 cc/min) and optical microscopy is used to size large agglomerates from a heavily sooting flame (fuel flow rate 67.5 cc/min). Optical microscopy is also used to size large agglomerates from a heavily sooting flame that have been classified by an inertial impactor. The electrical mobility distributions will be presented as the number concentration of particles with a given electrical mobility versus DMA rod voltage. This data is converted to a particle size distribution in terms of electrical mobility equivalent diameters.

The results from electron and optical microscopy show that the agglomerate geometric mean size distributions are broad at these fuel flow rates. From the weakly sooting flame, the overall

geometric mean size distribution has a log mean size of 0.16 μm with a geometric standard deviation (σ_g) of 2.2. From the heavily sooting flame, the overall geometric mean size distribution for particles with a size greater than 5 μm has a log mean size of 41 μm with a σ_g of 1.8. There is also a large number of agglomerates with sizes below the resolution limit of the optical microscope which are not measured.

The measured size distribution of agglomerates impacted on different stages of an inertial impactor suggests that the log mean agglomerate size is roughly proportional to the mean aerodynamic diameter for a given stage. The range of log mean agglomerate sizes is 2.7 to 36.0 μm. The corresponding mean aerodynamic diameter range is 0.5 to 11.0 μm.

The electrical mobility distributions for four different acetylene flow rates were measured. The mean electrical mobilities were 1.07×10^{-2}, 1.12×10^{-4}, 6.28×10^{-5}, 5.08×10^{-5} cm^2/volt-sec which would correspond to mean particle diameters of 0.014, 0.17, 0.25, 0.29 μm if the particles were all singly charged spheres, for fuel flow rates of 31.5, 39.5, 43.3, 67.5 cc/min respectively.

V.1 Electron Microscopy

Agglomerates from a weakly sooting flame with an acetylene flow rate of 39.5 cc/min were sized with electron micrographs. Figures V.1 to V.3 are micrographs of soot agglomerates viewed at 3

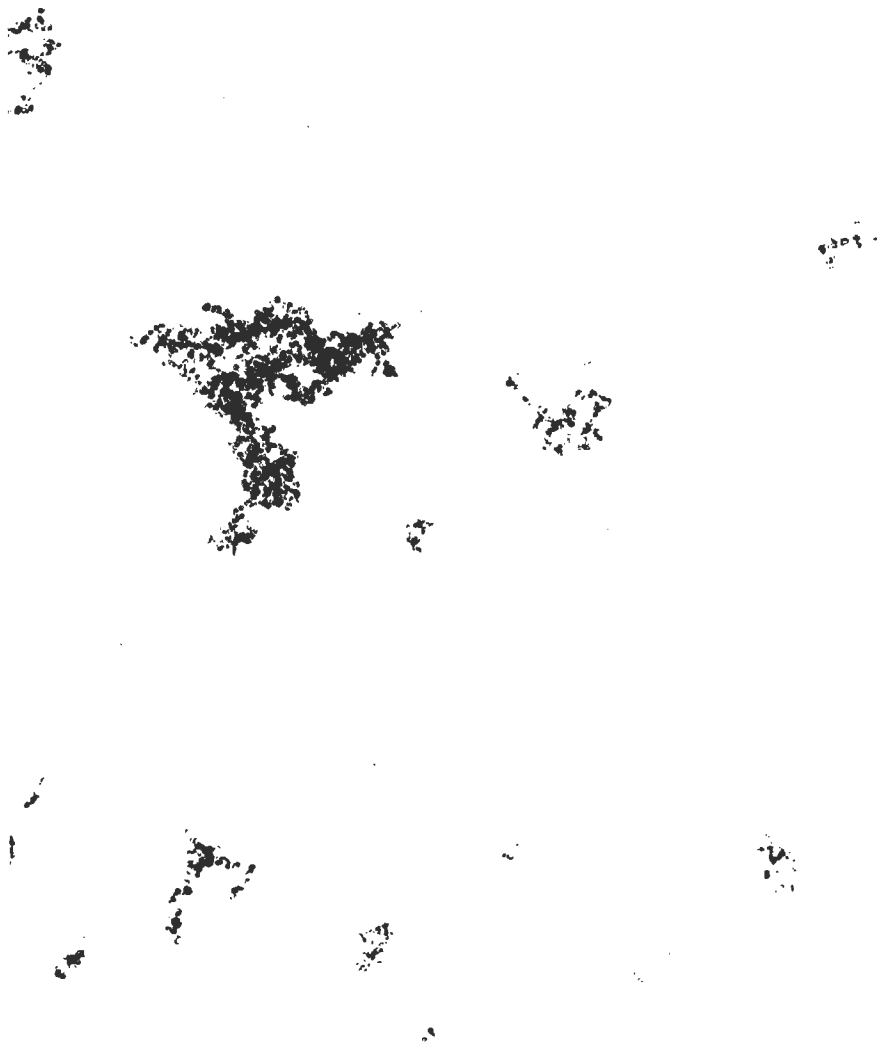

Figure V.1. Electron micrograph at a magnification of 9700X of soot agglomerates collected with the thermal precipitator. The acetylene flow rate was 39.5 cc/min.

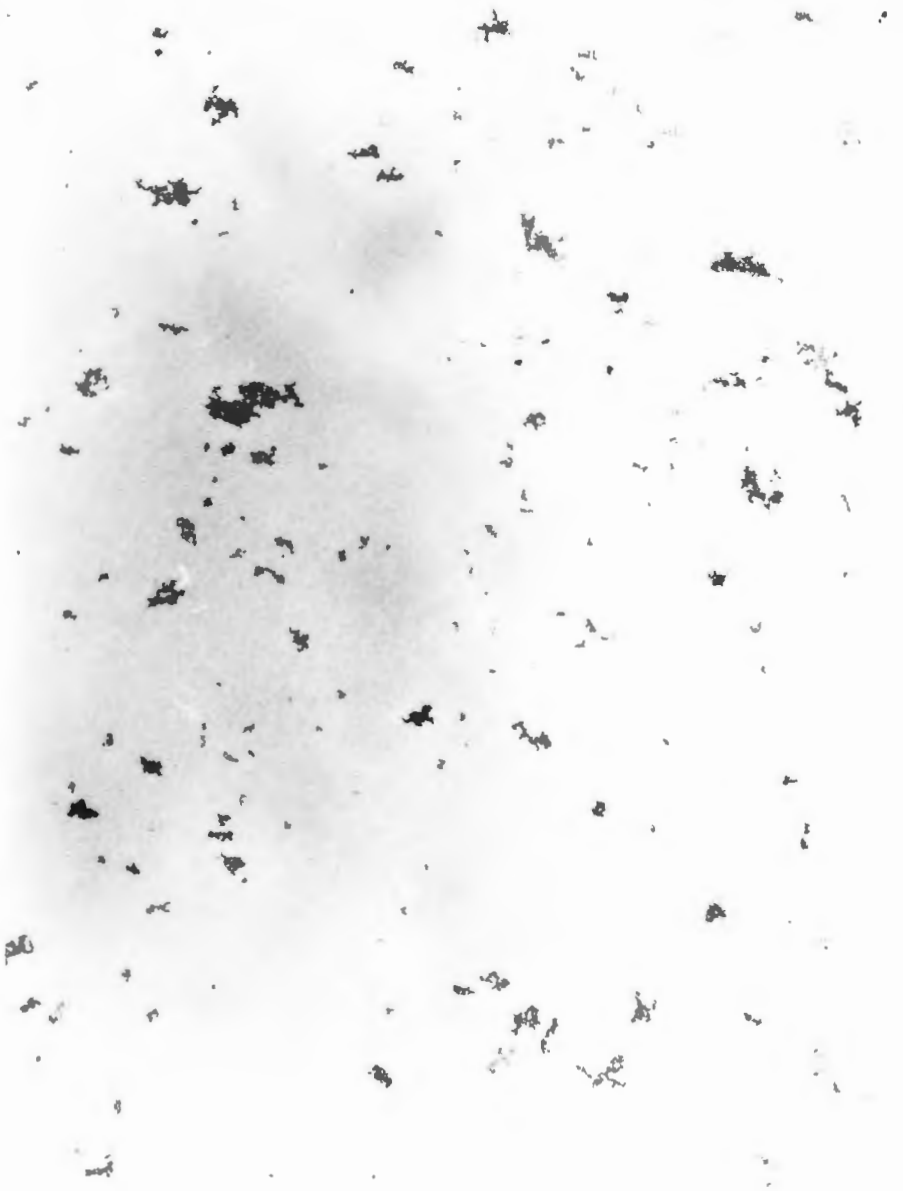

Figure V.2. Electron micrograph at a magnification of 2100X of soot agglomerates collected with the thermal precipitator. The acetylene flow rate was 39.5 cc/min.

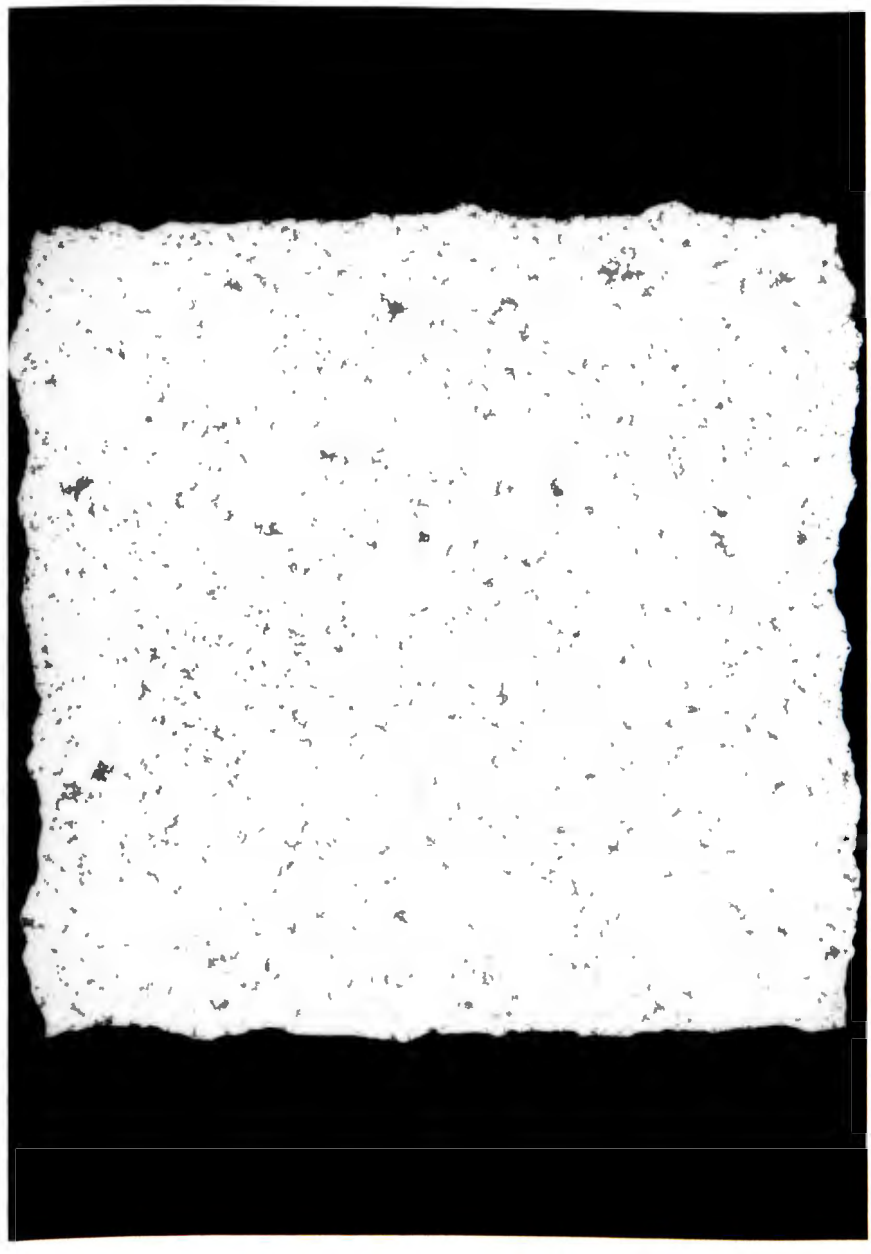

Figure V.3. Electron micrograph at a magnification of 490X of soot agglomerates collected with the thermal precipitator. The acetylene flow rate was 39.5 cc/min.

different magnifications, 9700X, 2100X, and 490X. The particles which deposit on the carbon film between the copper wires of the TEM are visible under the electron microscope. The entire range of particle sizes was visible with the electron microscopy. No clusters larger than 3 μm were observed over the entire field of view of 2 TEM grids with at least 10,000 clusters visible.

In obtaining the size distribution by microscopy, the following issues need to be considered (Cadle, 1975) : sample selection bias of the microscopist, the number of size intervals and the limits, the number of particles counted in each size interval, and the use of low magnification micrographs to improve the statistics of large (infrequent) particles. In order to obtain an unbiased representation of the sample, a pre-determined set of areas on the TEM grid are photographed. This procedure removes the microscopist from the selection process. The pre-determined viewing areas are selected over the entire sample surface and are spaced at equal distances from one another. The variations of the individual viewing areas at a given magnification will be checked for statistical consistency. Three different magnification were specified, 9700X, 2100X, and 490X. The difference in the viewing area between 9700X to 2100X and 2100X to 490X is approximately a factor of twenty. Collection times for samples taken with the thermal precipitator were 1, 3, and 6 minutes. Visual inspection of each sample determines the best loading. For this case, the sample with the collection time of 3 minutes was chosen. The ten pre-selected viewing areas were photographed at the three different

magnifications then, 8X10 black and white glossy photos are made from the TEM negatives. In order to assess the effect of loading on the sample, 10 pre-selected viewing areas of the sample with the one minute collection time were photographed at a magnification of 2100X. This sample will be compared to the higher loading sample.

The structural size distribution of the soot agglomerates is fairly broad, with the measured geometric mean size spanning three decades. This broad range, which is typical of many aerosol systems, is best analyzed based on a logarithmic size scale (Reist, 1984). The size range is separated into discrete size bins. The bins were chosen such that the difference in the logarithm of the upper size limit divided by the logarithm of the lower size limit ($\Delta(\log dp)$) is a constant. The bin size was chosen such that a statistically significant number of counts, typically at least 25 counts, in the middle size range bins were obtained. In practice, the lower and higher size bins had fewer counts. The lower magnification micrographs were used to view larger areas so that the counting statistics on the larger cluster sizes was improved. The standard technique is to size all of the particles at the highest magnification, then to decrease the magnification and size the particles that would fall in the larger size bins, then to again decrease the magnification and size particles that fall in still larger size bins. The reasoning behind this method is that the sample statistics for the large size bins are improved. It would be impossible to size all of the particles at the lowest magnification

because, first many particles would be to small to be sized, and second, the total number of particles would be too large.

The results for the number distribution are presented in a histogram. The y axis is the number of particles sized that fall in the respective size bin. Since the size bins have a constant spacing on a log scale, (Δ(log d) = 0.176) the plotted results are proportional to the number distribution defined as $\Delta N/\Delta(\log d)$. The x axis (log scale) gives the midpoint of the bin size.

The histograms in Figures V.4 to V.6 show the actual number counts for each magnification. With the 9700X micrographs, the log mean size is calculated to be 0.160 μm. At 2100X, the log mean size is calculated to be 0.692 μm. At 490X, the log mean size is calculated to be 1.41 μm.

The variation of the mean and standard deviation (σ) for the separate viewing areas at the same magnification is analyzed. Table V.1 gives the mean, σ_g, and population size for individual viewing areas at a given magnification. The analysis of variance method is used to test the equality of means (Hogg, 1977). At a 5% level of significance, the hypothesis that the samples are drawn from the same universe is not rejected. This means that based on the measured mean and standard deviation of the samples, it appears that there is no significant difference in the mean values. This implies that there is little or no sampling bias due to different sized

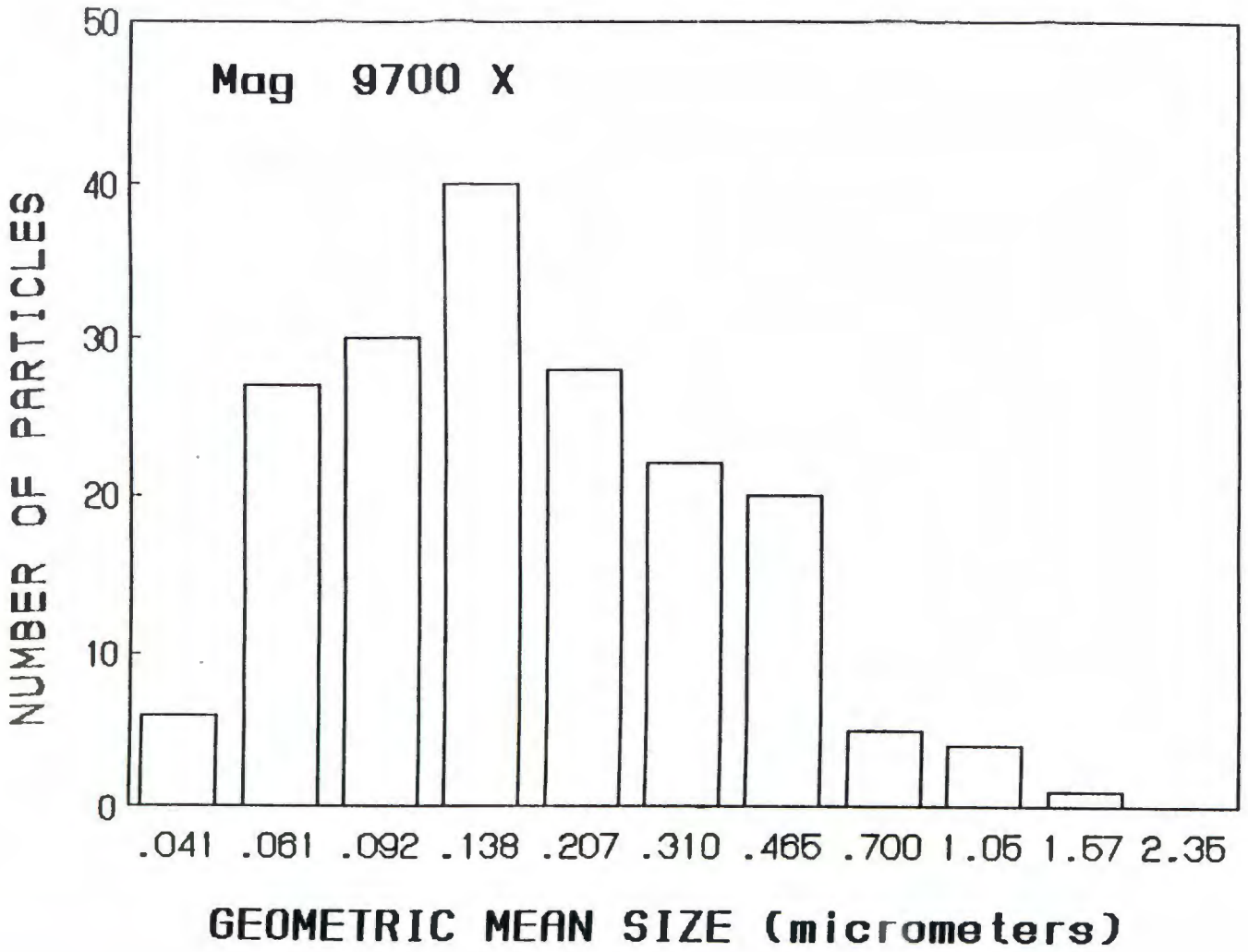

Figure V.4. Geometric mean size distribution from electron micrographs at 9700X (acetylene flow rate of 39.5 cc/min).

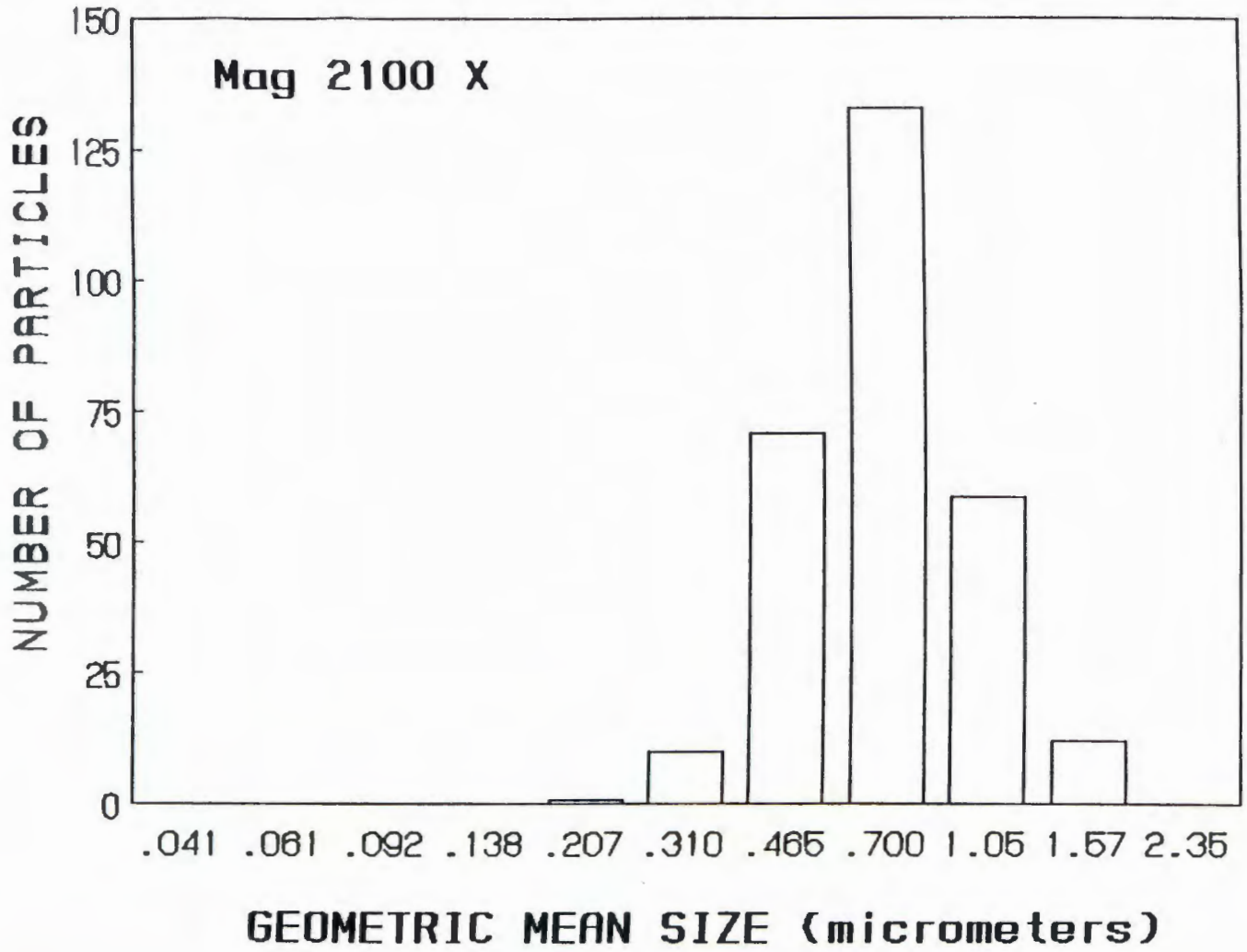

Figure V.5. Geometric mean size distribution from electron micrographs at 2100X (acetylene flow rate of 39.5 cc/min).

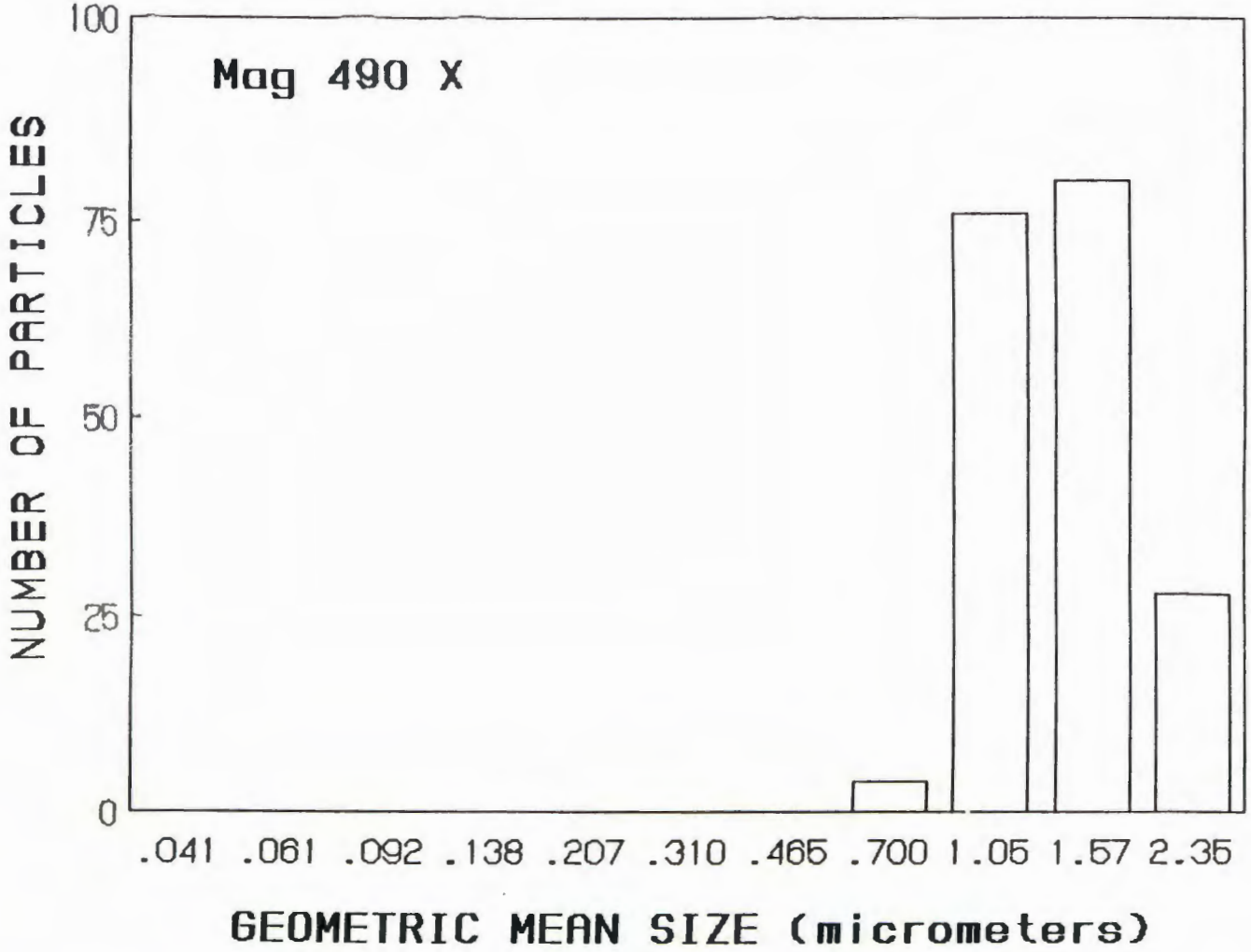

Figure V.6. Geometric mean size distribution from electron micrographs at 490X (acetylene flow rate of 39.5 cc/min).

Magnification	Sample size	Log mean size (μm)	σ_g
9700X	24	0.1284	1.86
-	27	0.1538	2.01
-	24	0.1885	2.23
-	20	0.1322	2.25
-	26	0.1706	2.43
-	27	0.1982	2.30
-	35	0.1557	2.02
2100X	26	0.7092	1.30
-	52	0.6076	1.43
-	35	0.7062	1.41
-	33	0.6229	1.49
-	53	0.7239	1.42
-	40	0.7941	1.35
-	47	0.7056	1.33
490X	7	1.297	1.13
-	26	1.461	1.32
-	16	1.248	1.22
-	18	1.746	1.28
-	17	1.249	1.16
-	16	1.439	1.22
-	23	1.454	1.32
-	17	1.594	1.23
-	21	1.401	1.31
-	28	1.274	1.23

Table V.1. Log mean size and geometric standard deviation of different fields of view from electron microscopy (acetylene flow rate 39.5 cc/min).

particles selectively depositing on a certain area of the TEM grid.

Figure V.7 is a plot of the size distributions for all three magnifications with the number of counts at different magnifications scaled to represent equal areas. A comparison can be made between the different size distributions to determine which best represents the true number of counts for a given bin. For the first 7 bins, the values from the 9700X micrographs are determined to be the best estimates of the true values. Except for the first bin size, the number of counts in each bin is 20 or greater. For the rest of the bins, the number of counts drops to 5 or lower. For the next two bins, (8,9) values from the 2100X micrographs are determined to be best. Bin 8 includes 133 measurements and bin 9 includes 59 particles. Bin 7 includes 71 measurements, but is discounted because the smallest size that could be conveniently measured from the TEM micrograph was larger than the lower limit of the bin. Thus the number of particles sized that fall in this bin is under-counted. For the last two bins (10,11), the values from the 490X micrographs were determined to be best. At 2100X, the number of counts in bin 10 is 12, and in bin 11 is 0. While at 490X, the counts in bin 10 is 80 and the counts in bin 11 is 28. Again, The effects of the cut-off in measured sizes appears in bin sizes 8 and 9 at 490X so these values are not used. It would be desired to have more overlap in the bin sizes for the different magnification samples, but since the magnification selection was made before the size measurement was performed it was possible only to estimate the magnifications that would give the desired overlap. For any

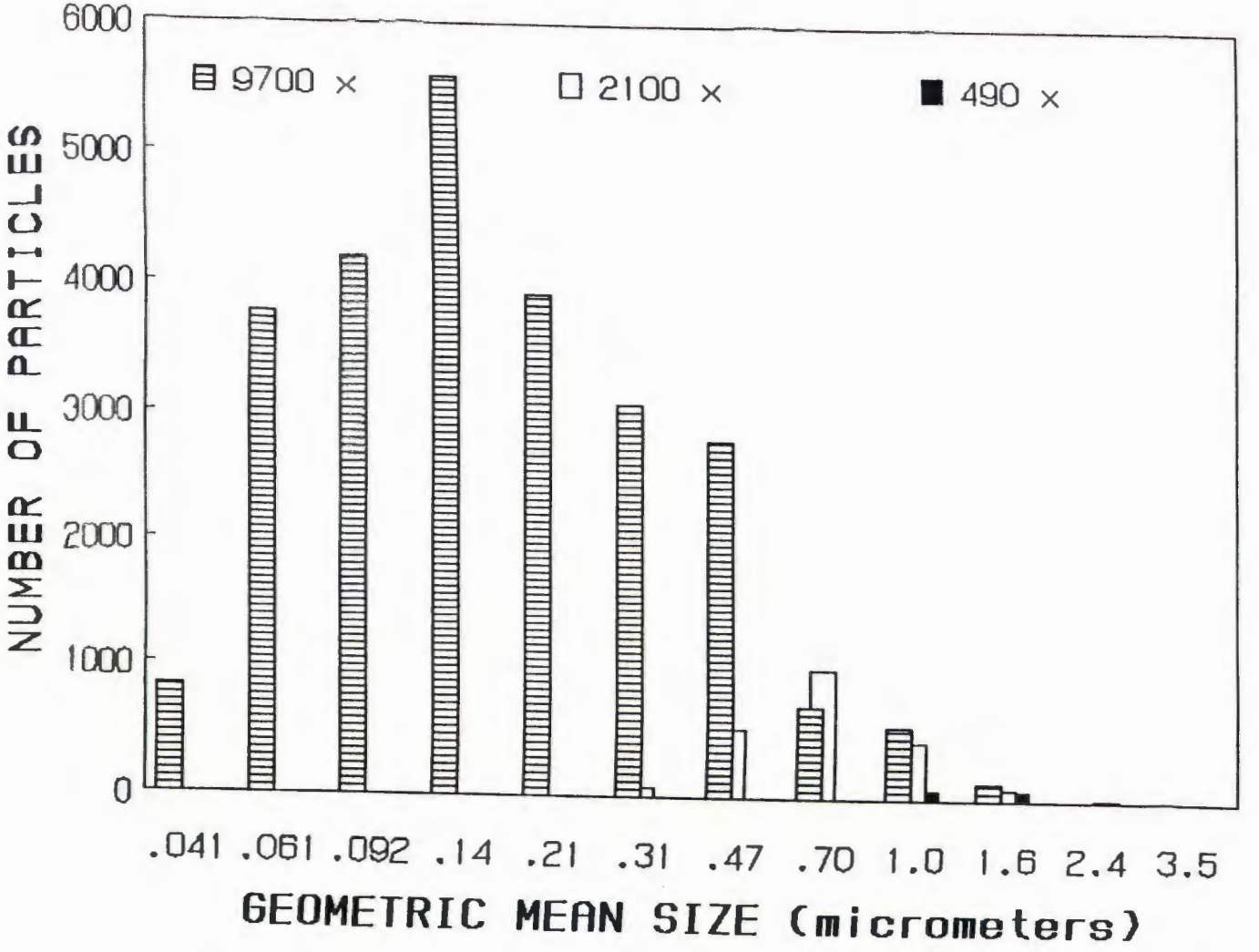

Figure V.7. Geometric mean size distribution from all three magnifications.

measurements of future size distributions of similar particles, a tighter magnification range should be specified. This combination of data yields the best representation of the true size distribution. The values for the log mean size and σ_g for this combination are 0.16 μm and 2.2 respectively.

To obtain an accurate representation of the cluster size distribution, the particle loading on the TEM grid must not be too high. At high loading the frequency of individual clusters overlapping is increased. This would tend to skew the cluster size distribution to larger sizes. On the other hand, for the sake of efficiency, it is desired to prepare the sample with relatively high loading so fewer samples (electron micrographs) are needed to obtain good sample statistics.

The effect of particle loading on the TEM grid was examined. A sample was taken at one third the loading (sampling time of one minute) and the size distribution at 2100X was measured. Figure V.8 is a plot of the size distributions for both data sets at 2100X. For low loading sample, the log mean size was found to be 0.50 μm with a σ_g of 1.64. Comparing this directly to the higher loading sample at the same magnification, the log mean diameter at this magnification is 30% less than the value at the higher loading. The data set from the low loading sample consists of 175 cluster measurements, while the data set from the high loading sample consists of 286 cluster measurements. Thus, the difference in the means appears to be due to differences in the samples and not just

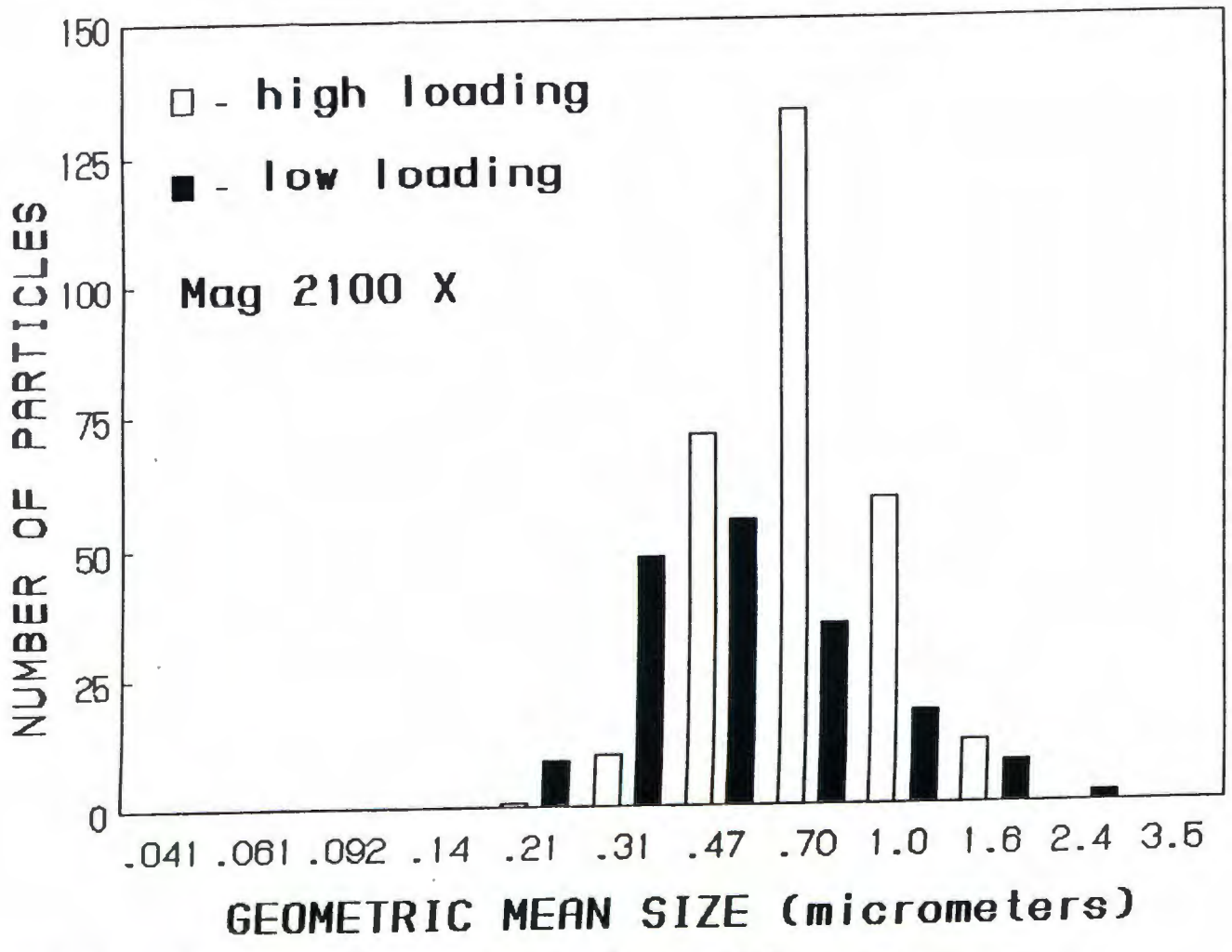

Figure V.8. Geometric mean size distribution at 2100X magnification for two different thermal precipitator samples, high loading corresponds to a collection time of 3 minutes, low loading corresponds to a collection time of 1 minute.

to variations in measured means from very similar populations. This difference is attributed to an overestimation of the log mean size of the high loading sample. At the high loading conditions, increased particle overlap results in overestimation of measured individual cluster sizes.

In an attempt to quantify the loading of particles on the different surfaces, a fractional coverage of the viewed surfaces was defined as the percentage of area covered by measured agglomerates. The area covered by an agglomerate is defined to be the measured length times width. The total area is the sum of the viewing areas of all micrographs. The fractional coverage of measured particles is 1.9% for the high loading sample and 1.05% for the low loading sample. The difference is approximately a factor of two. It is surprising to have such a large apparent loading effect of such low loadings.

Because the optical properties of aerosol particles depends on the mass distribution, it is useful to estimate what the mass distribution would be for the agglomerates. The agglomerate mass is obtained by first calculating the number of primaries in an agglomerate from equation I.2, then calculating the mass as the product of the number of primaries times the mass of an individual primary particle. The average primary diameter is estimated to be 0.03 μm with a density of 1.8 g/cc. The mass distribution from the combined number distribution is plotted in Figure V.9. The mass median geometric size is approximately 0.45 μm.

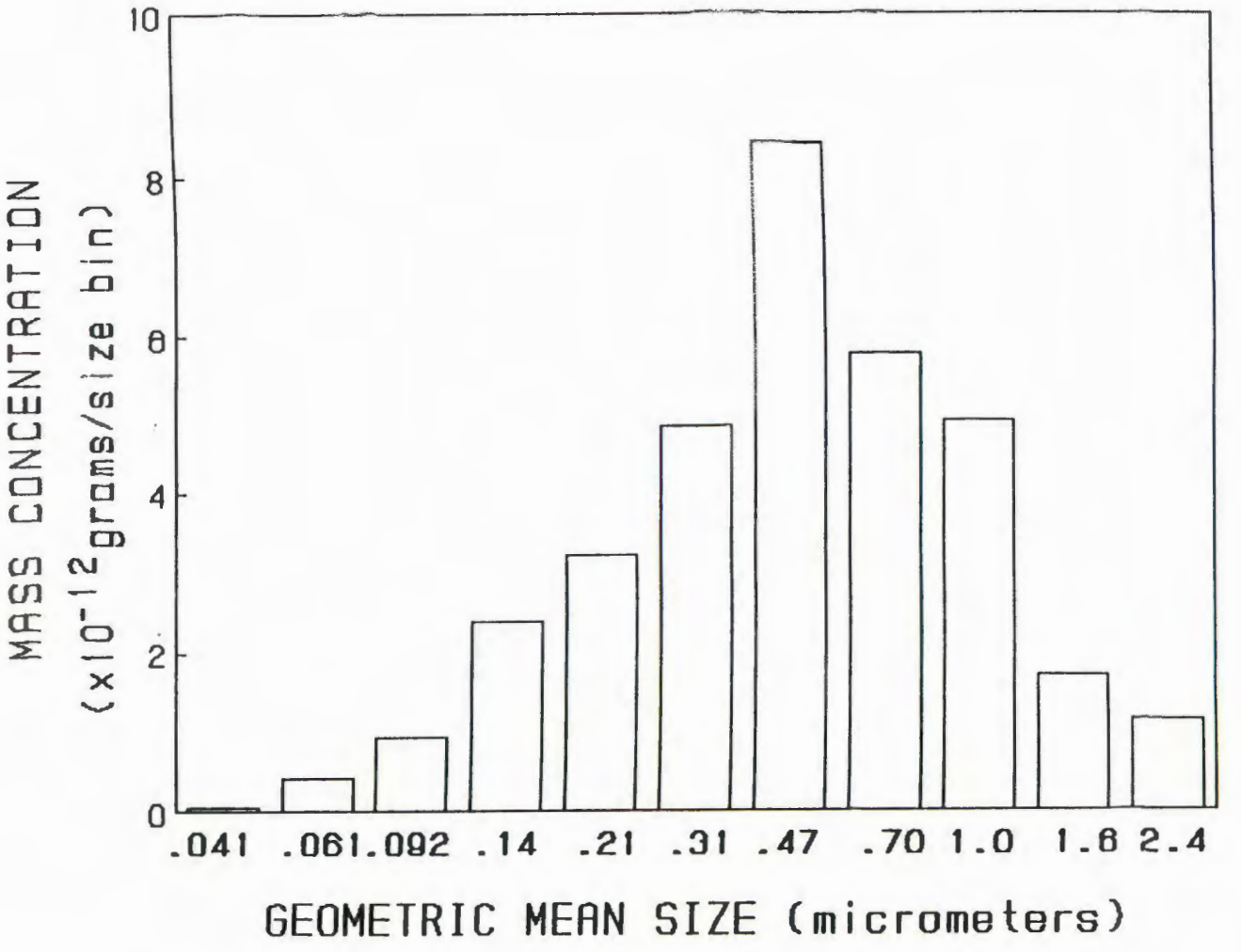

Figure V.9. Mass distribution from the combined geometric mean size distribution.

V.2 Optical Microscopy

Large clusters were sized using an optical microscope. Clusters with gross sizes on the order of 2 μm and greater can be effectively sized with the optical microscope. A fuel setting of 67.5 cc/min was used to produce mean cluster sizes on the order of 20 μm. The particle collection methods are the same as those used for the electron microscopy study. The only difference was that a glass cover slip is used as the collection surface instead of the TEM grid.

Three separate samples at different loading were collected. Two samples were collected with the thermal precipitator with sampling times of 1 and 3 minutes each. Another sample was collected by directly sampling above the flame. The optical microscope magnifications were 50X and 200X. Figures V.10 and V.11 are micrographs of particles at the two different magnifications. The observed size range is broad. Besides the large particles, many small particles are observed at high magnification. These particles are evident with the use of dark field microscopy, but are to small to be sized. It appears that the size difference between the large clusters and the much smaller clusters suggests a bimodal distribution. The cascade impactor data of soot from the same flame also points to this observation. Roughly, one third of the total mass collected from a sample ends up on the back-up filter which

Figure V.10. Optical micrograph of soot particles at a magnification of 50X, collected with the thermal precipitator for 1 minute. The acetylene flow rate was 67.5 cc/min.

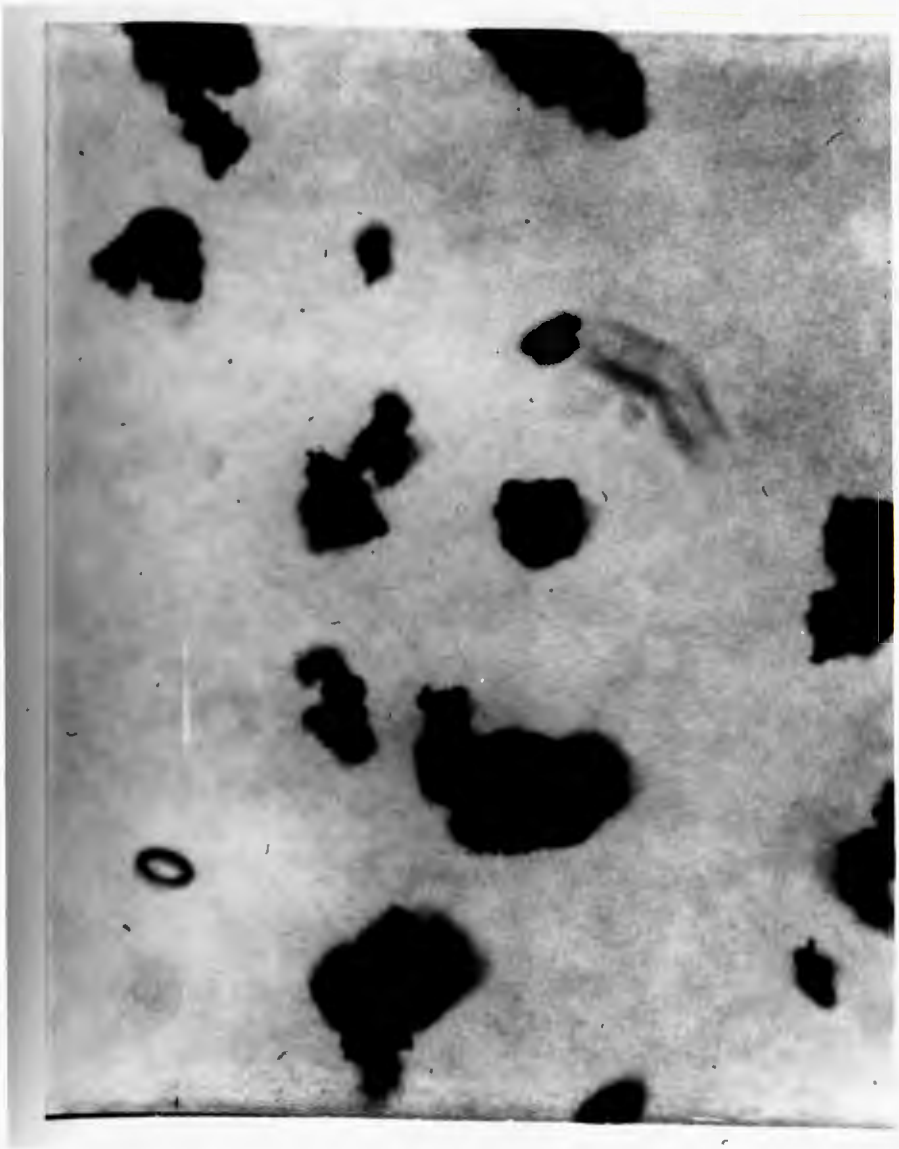

Figure V.11. Optical micrograph of soot particles at a magnification of 200X, collected with the thermal precipitator for 1 minute. The acetylene flow rate was 67.5 cc/min.

would include the small particles, while one third of the mass ends up on the first two stages at this acetylene flow rate.

The bin sizes are selected exactly the same way as explained in the electron microscopy section above. The only difference is that the starting bin size is much larger in this case.

Figures V.12 and V.13 are histograms of the results for clusters collected with the thermal precipitator with collection times of 1 and 3 minutes respectively. The values at each magnification are presented separately on each of the histograms. Figure V.14 is a histogram for clusters collected above lower section of the burner chimney. Here, only one magnification (50X) was examined. Values for the log mean size and σ_g for each of these separate distributions are given in Table V.2.

An overall size distribution is obtained by combining the results from the different magnifications for the low loading thermal precipitator sample. For the first 4 bin sizes, the values from the 200X sample best estimate the true values, and for the last 5 bin sizes, the values from the 50X micrographs best estimate the true values (Figure V.15). The log mean size for the overall distribution is 38.9 μm with a σ_g of 1.8.

The analysis of variance method was not used here to test the equality of means of different viewing areas because, essentially, the entire surface where particles were deposited on was examined.

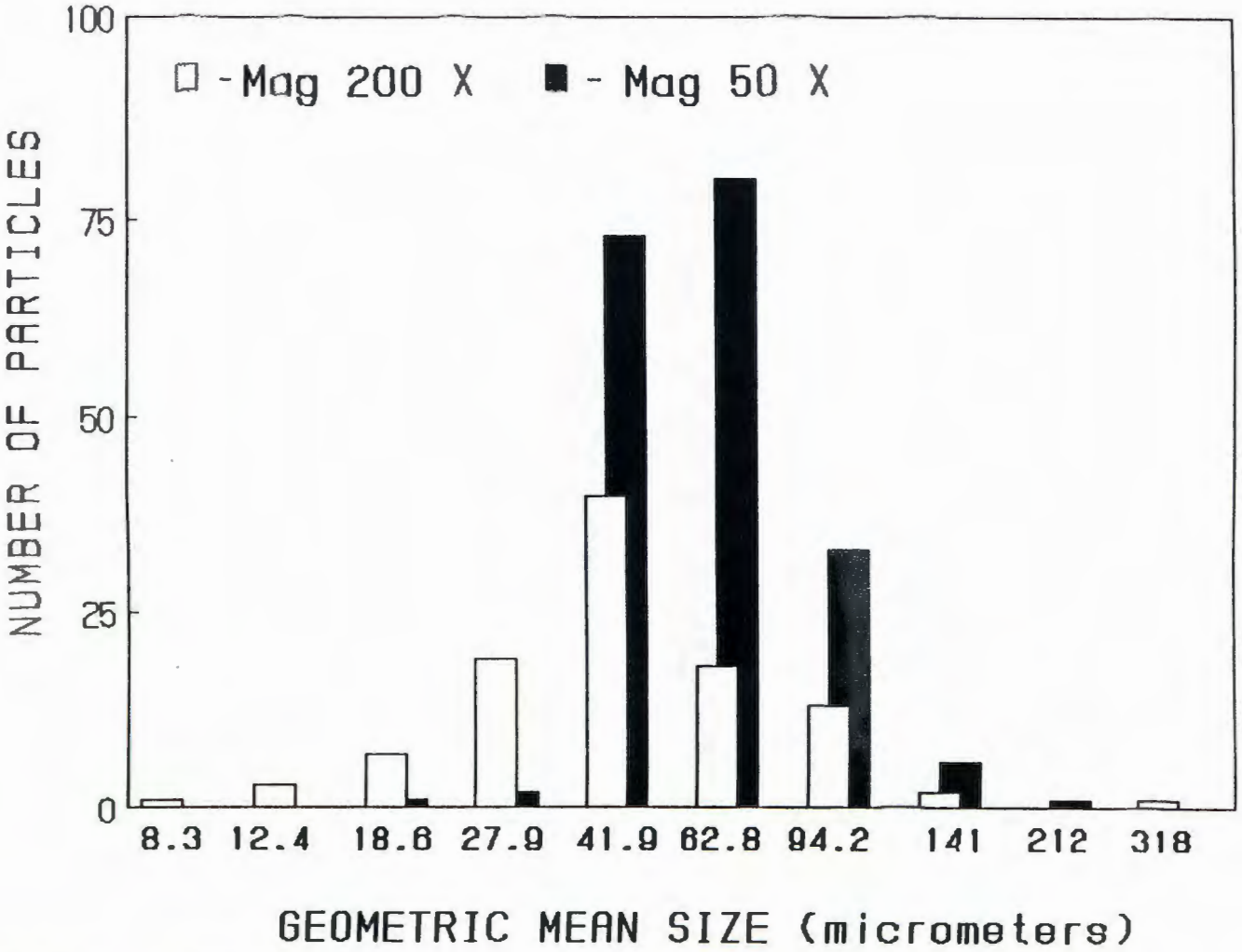

Figure V.12. Geometric mean size distribution from optical microscopy of soot particles collected with the thermal precipitator with a sampling time of 1 minute. The acetylene flow rate was 67.5 cc/min.

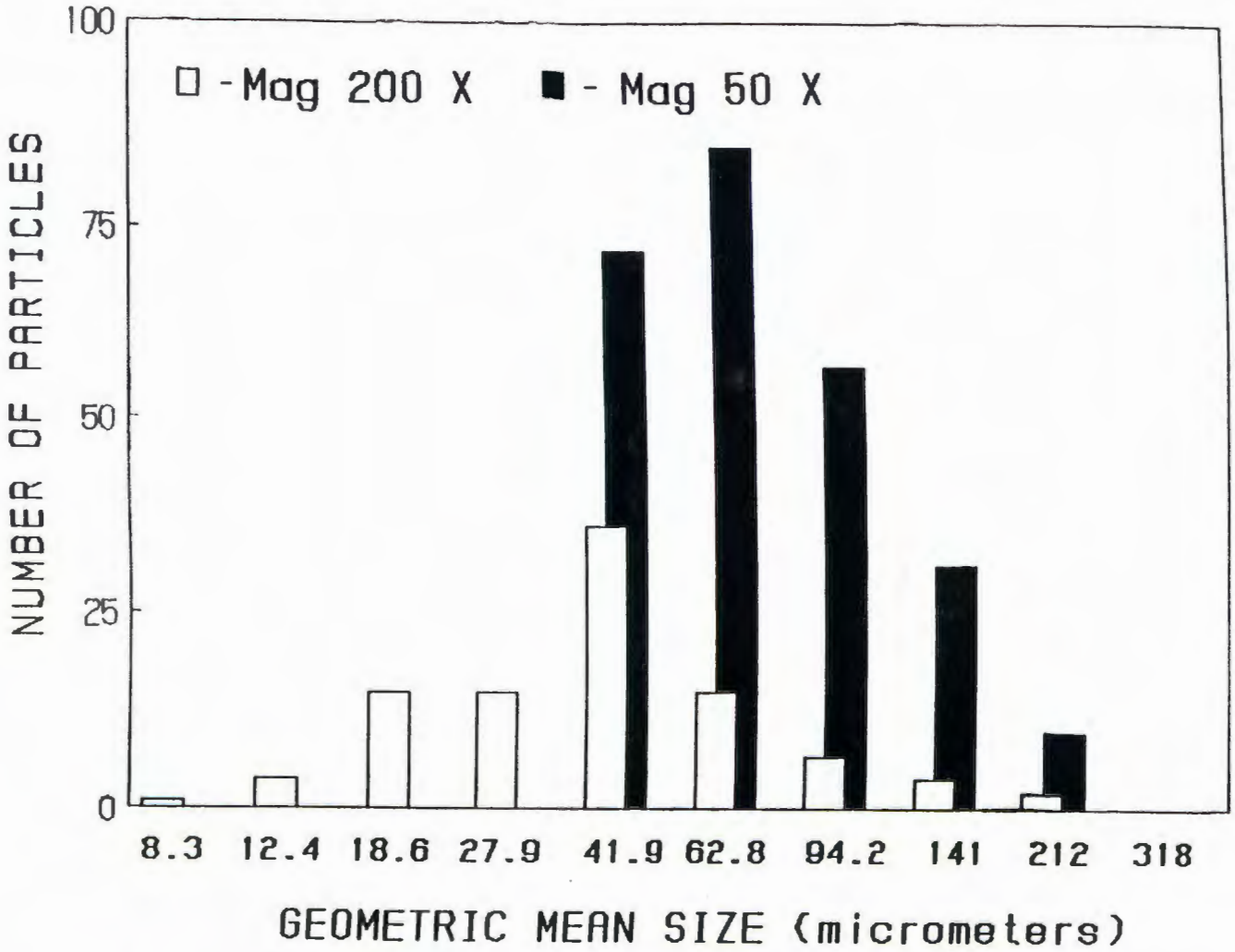

Figure V.13. Geometric mean size distribution from optical microscopy of soot particles collected with the thermal precipitator with a sampling time of 3 minutes. The acetylene flow rate was 67.5 cc/min.

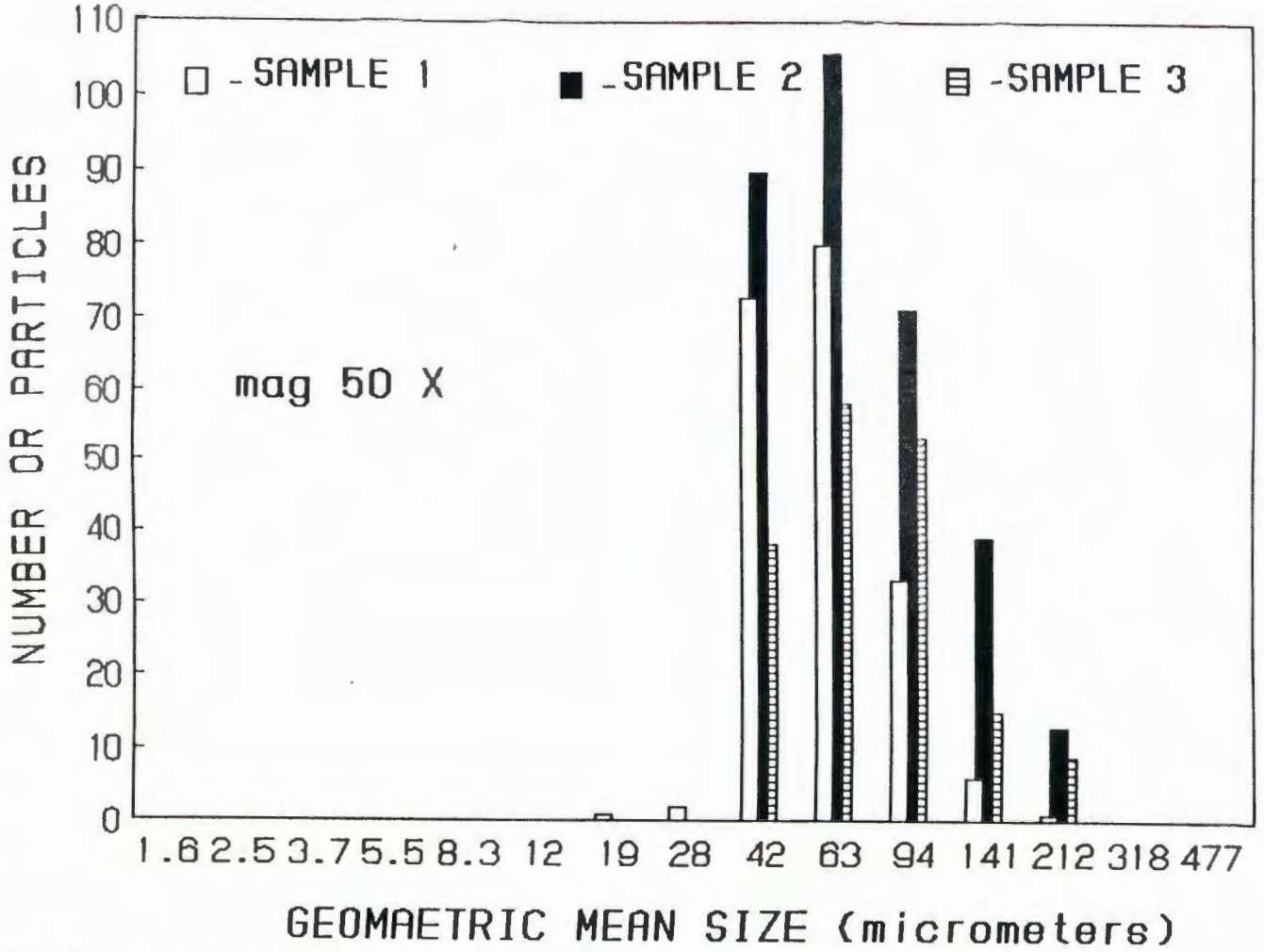

Figure V.14. Geometric mean size distribution from optical microscopy of soot particles collected by directly sampling above the flame (sample 3). Sample one and sample two are the low and high loading thermal precipitator samples respectively. The acetylene flow rate was 67.5 cc/min.

Sample	Magnification	Sample Size	Log Mean Size (μm)	σ_g
1	50X	196	58.9	1.39
1	200X	103	44.5	1.73
2	50X	255	72.2	1.56
2	200X	99	39.7	1.84
3	50X	173	76.2	1.56

Table V.2. Log mean size and geometric standard deviation of different samples from optical microscopy (acetylene flow rate 67.5 cc/min).

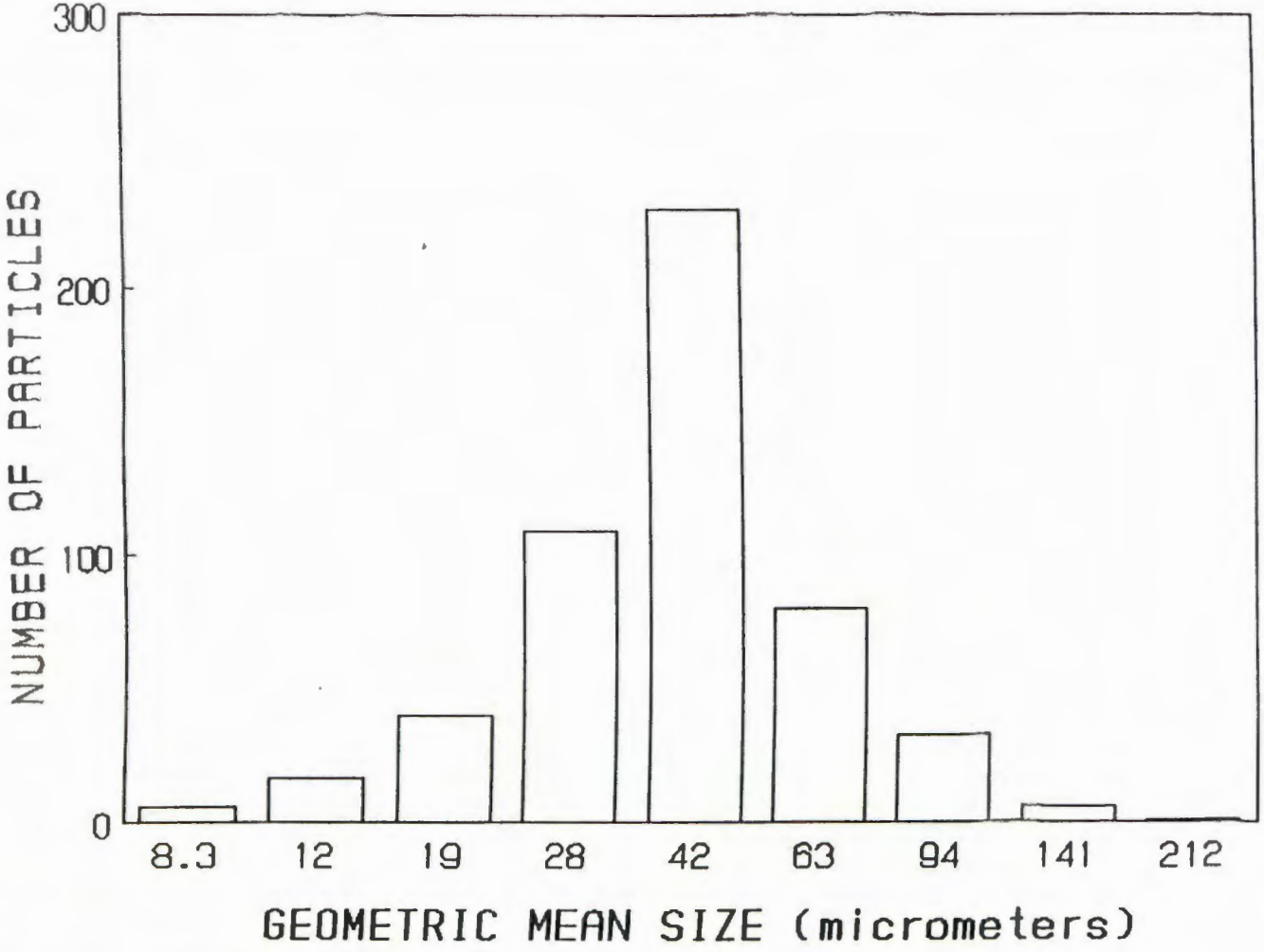

Figure V.15. Combined geometric mean size distribution from optical microscopy at 50X and 200X magnifications of soot particles collected with the thermal precipitator for one minute (sample one).

The loading appears to effect the measured mean size. At 50X, the different mean sizes for the low loading and high loading thermal precipitator, and the directly collected samples are 58.8, 72.2, and 76.2 μm. The total number of particles measured in each sample is greater than 175. There is good agreement between the high loading thermal precipitator sample and the directly collected sample means, while the two thermal precipitator samples represents the largest difference in the means. The surface coverage for the low loading and high loading thermal precipitator samples is 4.3 and 12% respectively. Again, it is assumed that the difference in the means is explained by the increased particle overlap occurring at high loading.

V.3 Inertially Classified Soot

The size distribution of impacted soot was examined to relate the structural size of the soot agglomerates to the aerodynamic size given by the cascade impactor stage cut-off size. The measurements are related to model predictions of the aerodynamic properties of soot agglomerates that include the fractal dimension as a parameter.

Samples of soot impacted on the various stages of the Anderson model 2000 cascade impactor were prepared. Thin (approximately 0.3 mm) clear plastic film was used as the collection surface. The film was coated with silicone oil in order to reduce particle bounce as explained in section VI. This surface is expected to have the same collection efficiency as the coated aluminum foil. The coated

plastic is still transparent, so optical microscopy can be used to examine soot impacted on the surface.

A fuel flow rate of 67.5 cc/min was chosen because the soot produced has a very broad distribution. Two samples with different loadings were prepared. The first sample was prepared by diluting the soot with air, (dilution ratio 5:1) then sampling for 10 seconds. The loading of this prepared sample was adequate for stages 3 to 7. A higher loading was required for stages 0 to 2. Direct sampling from the burner for 15 seconds gave the desired loading for the first three stages.

The viewing magnification was varied from 50X to 1500X. The magnified samples were photographed with enough photos taken of different views so a representative sample is obtained. Figures V.16 to V.18 show particles that deposited on stages 1, 3, and 6 respectively. These photos illustrate the width of the size distribution of the impacted soot particles and the difference in sizes for different stages. Geometric mean size distributions for each sample (impactor stage) were measured. In Table V.3, the log mean geometric size and the standard deviation for each stage is given. The log mean geometric size is much greater than the mean aerodynamic diameter expected for a particular stage. The mean aerodynamic diameter is estimated from the geometric mean of the cut-off diameters for the given stage and the stage above it.

Figure V.16. Optical micrograph of soot impacted on stage 1 of the Anderson cascade impactor. The magnification is 200X.

Figure V.17. Optical micrograph of soot impacted on stage 3 of the Anderson cascade impactor. The magnification is 200X.

Figure V.18. Optical micrograph of soot impacted on stage 6 of the Anderson cascade impactor. The magnification is 200X.

Stage	Aerodynamic Diameter μm	Log Mean Size μm	σ_g	Apparent Density g/cc	Mean Aspect Ratio
1	11.0	36.0	1.72	0.094	1.65
2	8.1	26.6	1.66	0.093	1.46
3	4.7	15.9	1.69	0.088	1.66
4	3.0	10.9	1.73	0.076	1.65
5	1.6	6.6	1.68	0.059	1.61
6	0.9	4.2	2.05	0.046	1.97
7	0.5	2.7	1.66	0.034	1.77

Table V.3. Agglomerate size measurements of inertially impacted soot (acetylene flow rate 67.5 cc/min).

Figure V.19 is a histogram for the discrete values of the size distributions for stages 1,3,and 6. It is obvious from the plot that the size overlap between stages is much greater than expected for compact particles where most particles deposited on a stage would fall in essentially one bin.

Figure V.20 shows the aerodynamic mean size plotted against the log mean geometric size on a log-log plot. The line that passes through the data points has a slope of 1.0. Therefore, it appears that the aerodynamic diameter is roughly proportional to the geometric mean diameter for clusters in this size range.

V.5 Electrical Mobility

The differential mobility analyzer (DMA), which is described in section II.2, is an instrument which separates particles into narrow electrical mobility ranges. For a classifier of this arrangement, the mean electrical mobility (Z_{pm}) and width of the mobility (ΔZ_p)is given by (Knutson, 1974)

$$Z_{pm} = \frac{qc \ln (r2/r1)}{2 \pi V L} \qquad (V.1)$$

$$\Delta Z_p = \frac{(qa+qs) \ln(r2/r1)}{4 \pi V L} \qquad (V.2)$$

qc, qa, and qs are the sheath, aerosol, and the monodisperse flow rates in cc/sec. r2 and r1 are the outer cylinder and inner rod

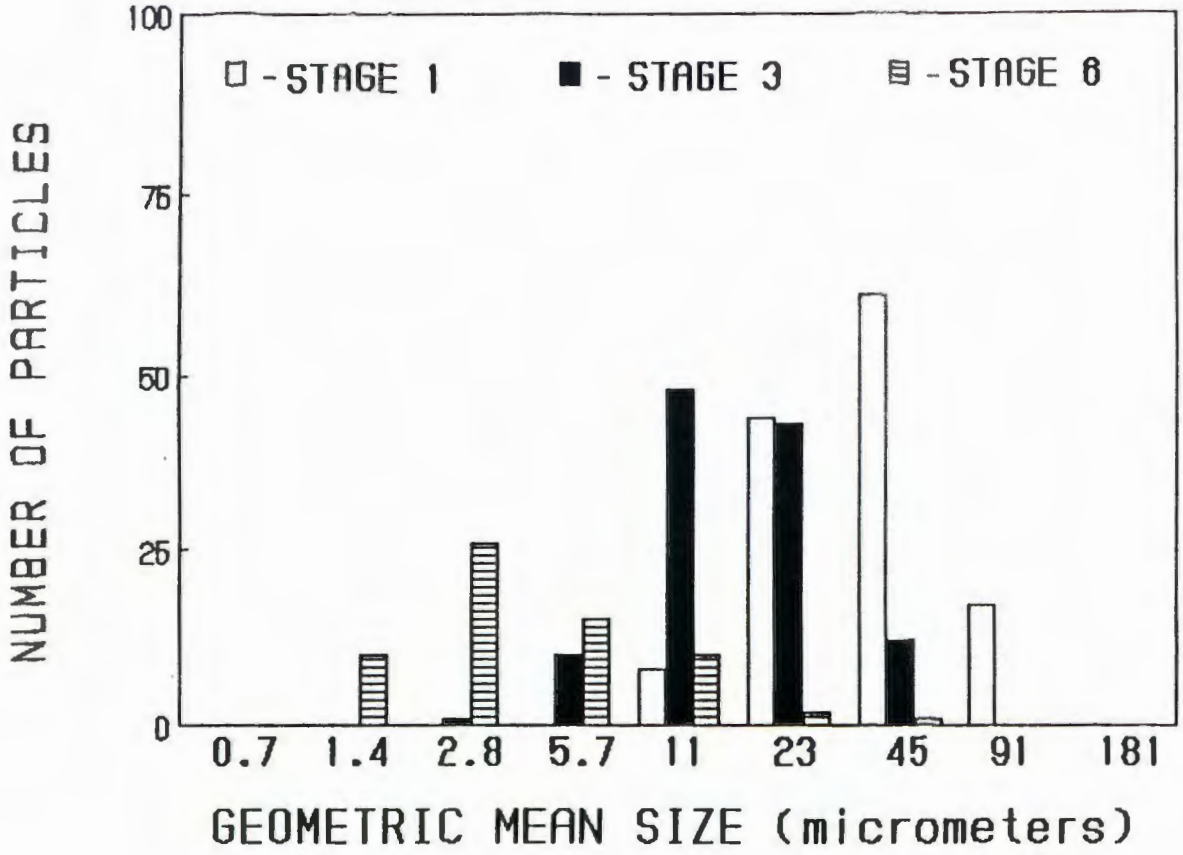

Figure V.19. Geometric mean size distributions of inertially impacted soot agglomerates. Aerodynamic cutoff sizes for stages 1, 3, and 6 are 11.0, 4.7, and 0.7 μm respectively.

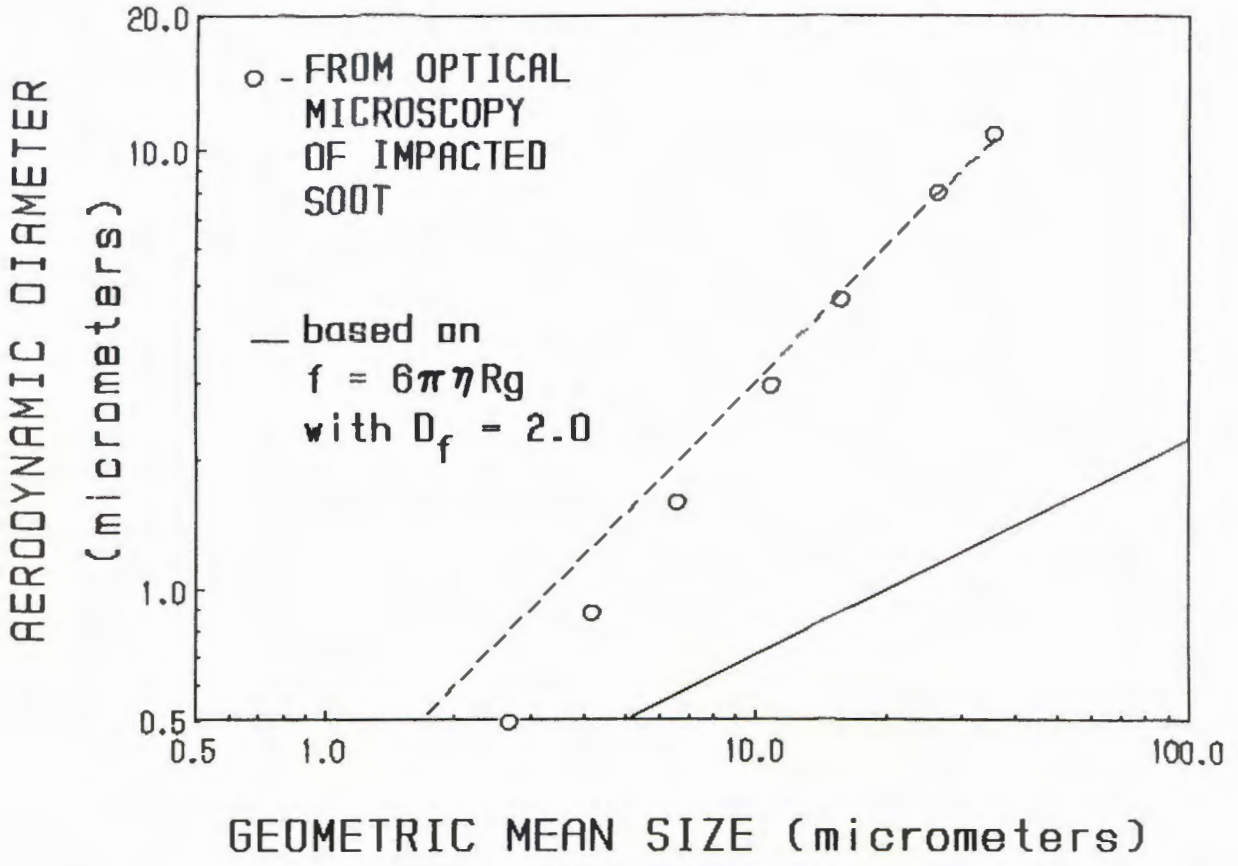

Figure V.20. Aerodynamic diameter versus geometric mean agglomerate size from inertially impacted soot. The dashed line that passes through the data points has a slope of 1.0. The solid line corresponds to a model prediction for the aerodynamic diameter that assumes a fractal dimension of 2.0 for the agglomerates.

diameters. V is the applied voltage and L is the rod length. By measuring the number concentration of the exit aerosol, an electrical mobility distribution of the exit aerosol is obtained. If information on the particle charge distribution is known, the size distribution of the input aerosol can be inverted from the electrical mobility distribution.

When aerosol particles are exposed to a high concentration of bipolar (both positive and negative) ions for a sufficiently long time, the aerosol particles obtain a steady state charge distribution. That is, a certain fraction of particles of diameter dp remain uncharged while some fraction contains ± 1,2,3,... charges. Experimentally, the steady state charge distribution for particles with diameters greater than 0.1 μm follows the so called Boltzmann charge distribution. This charge distribution is a normal distribution about the net charge fraction equal to zero. The ratio of the number of particles carrying ± 1,2,3... charges to the number of neutral particles is given by

$$\frac{N_p}{N_0} = \exp\left\{\frac{-p^2 e^2}{4 \pi dp k T}\right\} \qquad (V.3)$$

where N_p is the number of particles with diameter dp carrying p charges, e is a constant. The fraction of particles carrying p elementary charges (f_p) is given by

$$f_p = \frac{N_p/N_0}{1 + 2 \Sigma N_p/N_0} \qquad (V.4)$$

With particles smaller than 0.1 μm, the experimental charge distribution deviates from the Boltzmann charge distribution (Kousaka, 1985).

The DMA contains a bipolar charging section which consists of Kr_{85} radioactive gas sealed in a tube. At normal operating conditions, the aerosol is exposed to a high concentration of both positive and negative ions, with a residence time sufficiently long for most aerosols to reach a steady state charge distribution.

The size distribution is obtained from the electrical mobility distribution by using Hoppel's inversion algorithm (Hoppel, 1978). The assumption required for this algorithm is that the aerosol essentially contains no particles greater than 1 μm in diameter. This size is the upper limit of measurable electrical mobilities of singly charged particles for the TSI model 3071. Hoppel's inversion method requires dividing the mean electrical mobilities (Z_{pm}) (where concentration readings are taken) so that the ΔZ_p's span the entire mobility range of the instrument. A number concentration is measured with a particle counter for each selected electrical mobility (voltage setting). The first approximation is to assume that all particles extracted at a selected electrical mobility carry +1 charge. The size distribution is given by calculating the fraction of particles carrying +1 charges from equations V.4. The inverse of this number for a given electrical mobility is multiplied by the number concentration recorded for that electrical mobility

setting. Higher order approximations take into account the multiple charged particles with a particle mobility (B) that is equal to the single charge electrical mobility divided by the integer number of charges on the particle. These particles come through at the same electrical mobility setting. The concentration of such particles is subtracted from the first order approximation. In practice, the algorithm converges in less than six iterations.

The DMA flow rates were 2.7 l/min sheath air and excess air, and 0.5 l/min aerosol inlet and outlet. The number concentration was measured with the CNC. The rod voltage was stepped such that the entire mobility range was covered.

The data is plotted as the number concentration from the CNC versus the applied rod voltage. In Figure V.21 and V.22, the number concentration for the four different fuel flow rates are plotted. The log mean electrical mobility for the flow rates 33.5, 39.5, 43.3, 67.5 cc/min are 1.07×10^{-2}, 1.12×10^{-4}, 6.28×10^{-5}, and 5.08×10^{-5} cm^2/volt-sec corresponding to electrical mobility equivalent diameters of 0.014, 0.17, 0.24, 0.29 μm respectively. For the low fuel flow rate, the measured mobilities are sufficiently large enough to assume that the particles have at most one charge. Thus, the number concentration of particles before classification is directly related to the number concentration of particles after classification. The size distribution for these particles is plotted in Figure V.23. For the two separate electrical mobility distributions, log mean particle sizes are estimated to be 0.0139

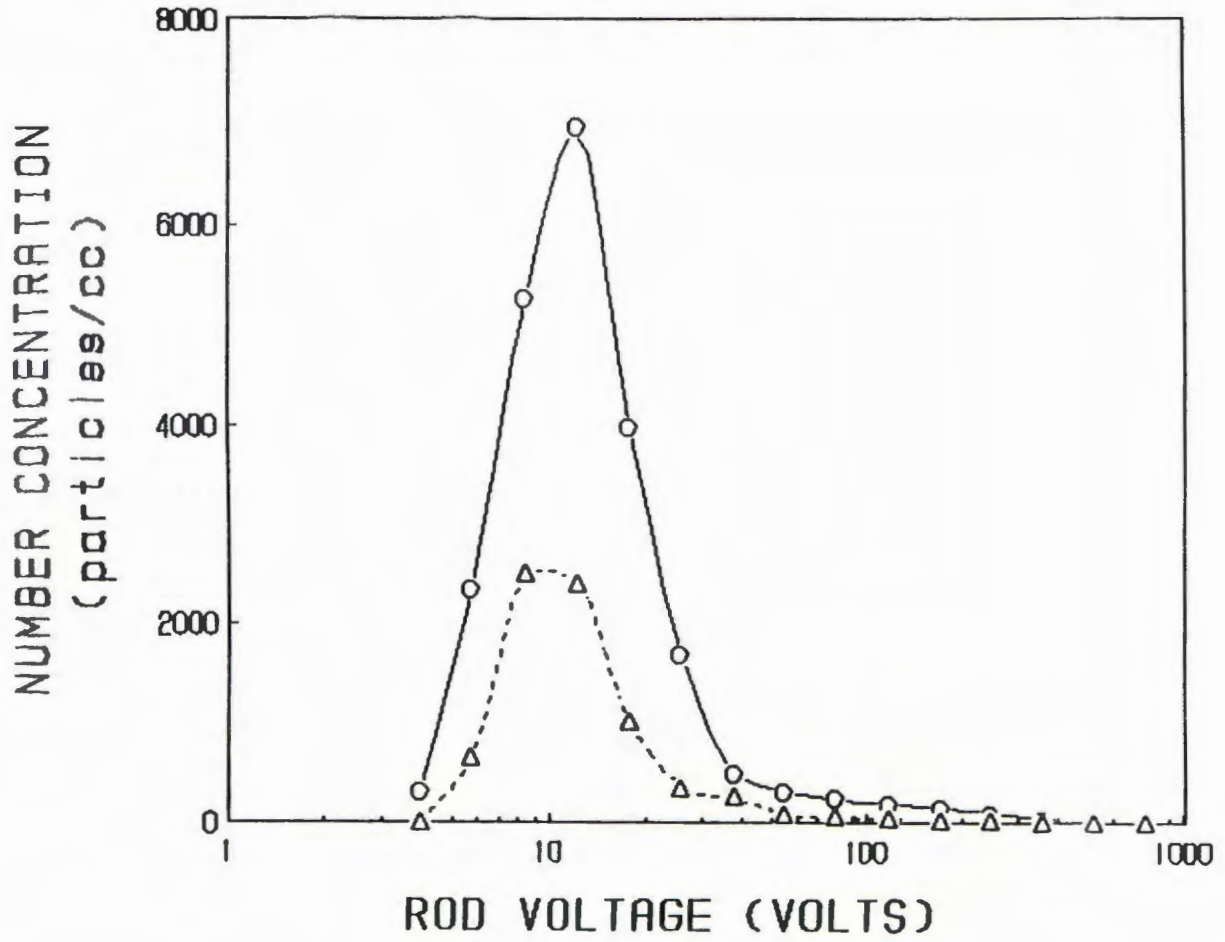

Figure V.21. Electrical mobility distribution of soot particles at an acetylene flow rate of 33.5 cc/min. Circles and triangles correspond to two different data sets with different dilution ratios.

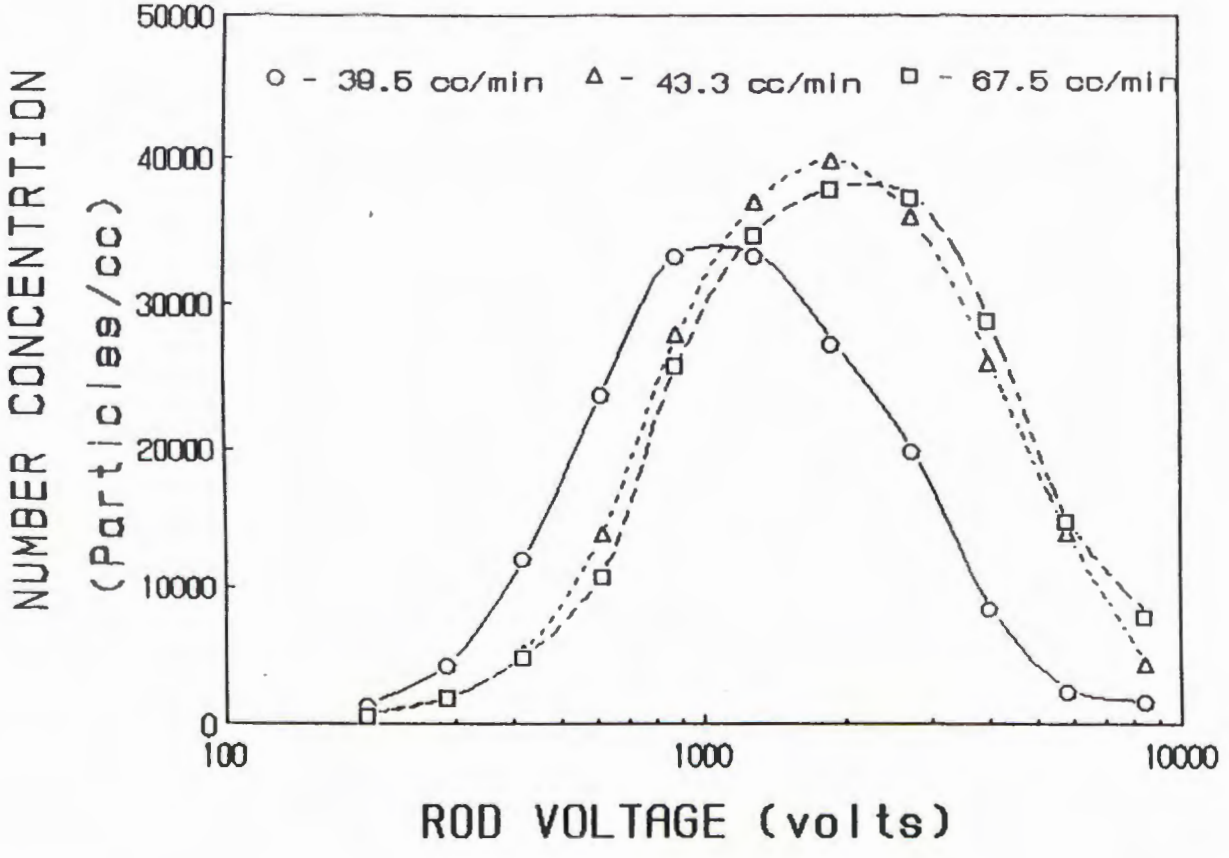

Figure V.22. Electrical mobility distribution of soot particles at three different acetylene flow rates.

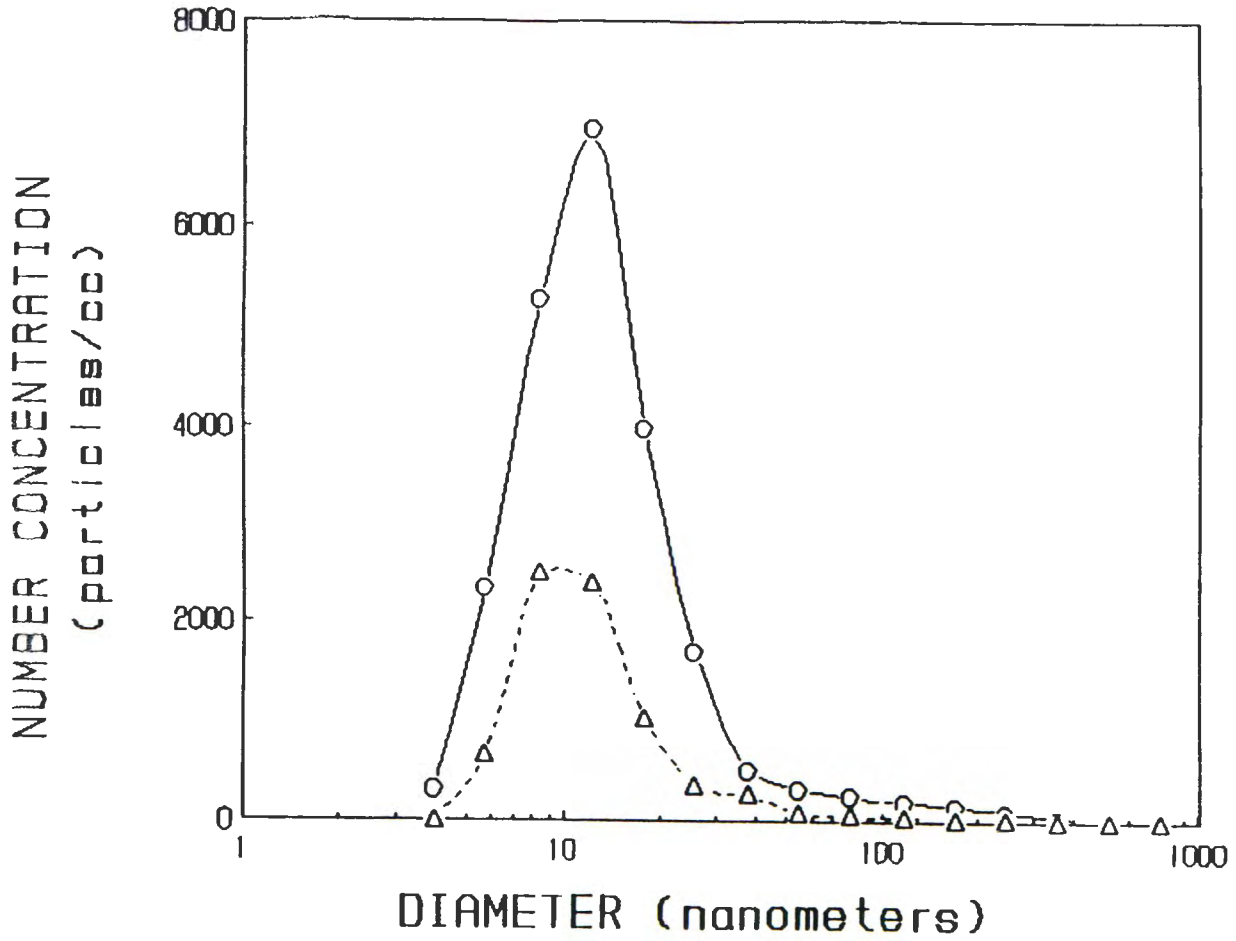

Figure V.23. Size distribution of soot particles at an acetylene flow rate of 33.5 cc/min. Circles and triangles correspond to two different data sets with different dilution ratios.

and 0.0138 μm with σ_g's of 1.33 and 1.26 respectively.

For the particles at the three higher fuel flow rates, there is ambiguity in interpretation of the measurements due to multiple charging. To relate these data to size distributions requires the assumption of charging theories. Since for later analysis, the electrical mobility equivalent size distribution is required, the mobility distributions will be inverted to size distributions by making an assumption of the charge distribution of clusters. Because of the lack of experimental data, the assumption is made that the clusters obtain a steady state charge distribution equivalent to the Boltzmann distribution. The particle diameter used in the charge distribution is the electrical mobility equivalent diameter.

The corresponding size distributions for the three different fuel flow rates are plotted in Figure V.24. The log mean electrical mobility diameters are 0.235, 0.350, 0.390 μm with σ_g's of 1.65, 1.57, 1.68 for the fuel flow rates corresponding to 39.5, 43.3, and 67.5 cc/min.

VI. CASCADE IMPACTOR

A cascade impactor was used to measure mass median aerodynamic diameters of soot particles from different fuel settings. The aerodynamic diameter is defined as the diameter of a spherical particle of with a density of 1.0 g/cc that has the same has the same settling velocity as the particle in question.

An impactor is an instrument that separates particles by inertial forces. For vertical flow impinging on a flat plate, the fluid streamlines follow a curved path. In an impactor the flow exits an orifice and is directed to a surface. Particles suspended in the air stream are subjected to inertial forces and will cross streamlines and may impact on the surface. If it is assumed that the velocity profile from the exit of the orifice is uniform and flat, and that the y component of the velocity profile is a function of y only (no boundary layer), the impactor is said to behave ideally. The ratio of the stopping distance of a particle to the radius of the impactor orifice opening is a dimensionless group known as the Stokes number (Stk). The Stokes number is important in describing impactor behavior. For an ideal impactor, a plot of collection efficiency versus $\sqrt{}$(Stk) yields a step function at a particular Stokes number. For real impactors, the efficiency curve has more of an S shape. The 50% efficiency point (Stk_{50}) defines a particle cut off diameter for a real impactor at a given flow rate. For an impactor stage, 50% of the particles with Stk_{50} will be

deposited on the impactor surface, while 50% will remain suspended.

The flow field, size, and density of the particle control whether it will impact on a surface. The typical impactor has a nozzle or series of nozzles which direct the flow toward an impaction surface. The throat diameter, distance from the exit of the nozzle to the surface, and the Reynolds number influence the flow field of the air stream. For size distribution analysis, impactor data is reduced in the following manner. The net mass collected on each stage is converted to a weight percent of particulates collected on that stage. This is converted to a weight percent less than the stated 50% cutoff diameter of a particular stage. The weight percent less than 50% cutoff diameter is plotted on log probability paper versus the 50% cutoff diameters for each stage. A straight line is drawn through the data points. The intersection of this line and the 50% probability line gives the mass median aerodynamic diameter of the aerosol. If one assumes a log-normal distribution, the standard deviation is given by the size at the 50% probability divided by the size at 15.87% probability. A curve through the data points which has significant tails on either end shows that the size distribution does not fit a log-normal distribution well.

The impactor used in this study is an Anderson model 2000 eight stage cascade impactor with a backup filter. The 50% cutoff diameters stated in the manual (Model 2000, Anderson, Atlanta, Ga.) for an aerosol flow rate of 28.3 l/min are given in Table VI.1. The

Stage	Anderson (μm)	Rao and Whitby (μm)
0	11	-
1	7	11
2	4.7	6
3	3.3	3.7
4	2.1	2.4
5	1.1	-
6	0.7	-
7	0.4	-

Table VI.1. Aerodynamic cutoff diameters of the Anderson model 2000 cascade impactor.

assumption made is that once a particle hits the impaction surface it stays there. But in reality, some of the impacted particles may bounce and be re-entrained in the air stream if they are solid particles. This particle bounce will skew the true size distribution so that the measured size distribution looks smaller than it actually is. Different types of collection surfaces yield different effective cutoff diameters for a give stage. A dry, hard surface increases particle bounce. Glass filter paper will reduce particle bounce, but there may be enhanced particle collection from fibers protruding above the impaction surface. One of the better collection surfaces for solid particles is a surface coated with a sticky substance. Particles landing on the sticky surface will not bounce or re-entrain. In this study, glass filter paper, bare and coated aluminum foil were used and the results compared.

The stages of the Anderson 2000 impactor were independently calibrated by Rao and Whitby (1977) using polystyrene latex spheres of various size. They tested the collection efficiency of different surfaces. The 50% cutoff diameters for stages 1 through 4 using silicone oil coated impaction surfaces are also given in Table VI.1. Stage zero was not calibrated, nor were stages 5-7. These values will be used instead of the manual values for data reduction. An independent calibration of the Anderson impactor was performed. The results indicate that the Whitby cut-off values are more accurate. The details of this calibration are discussed in Appendix II.

A comparison of different collection surfaces shows how the collection surface affects the reported size distribution. Table VI.2 gives the mass median diameter and the σ_g for samples collected on different surfaces with the fuel flow rate being fixed at 43.3 cc/min.

The particles striking the un-coated aluminum foil experience a lot of particle bounce, thus skewing the size distribution to make it look smaller than it really is. The coated foil had a thin layer of viscous silicone oil applied to it. The silicone oil was diluted 10:1 with hexane and applied to the foil and allowed to dry overnight.

The more accurate mass median aerodynamic diameter is closer to 0.3-0.5 μm. The glass filter paper gives the largest mass median diameter. There may be enhanced particle collection due to fibers protruding into the air stream and collecting particles of a smaller size.

A better method of getting an even coating of silicone oil is to use silicone oil in a spray can. There is another parameter in the operation of the impactor and that is collection time. There is an upper limit to the total mass collected on any given plate. The limit stated in the Anderson manual is 10 mg. Above this value, re-entrainment can be a problem. Here, the total mass collected on a given plate is less than 2.0 mg. Above 2 mg, there appears to be re-entrainment of the soot particles. Therefore, a suitable

Collection Surface	Mass Median Diameter (μm)	σ_g
glass fiber	0.80	4.4
glass fiber	0.72	3.7
uncoated alum. foil	0.19	5.3
uncoated alum. foil	0.20	7.3
coated alum. foil	0.51	3.6
coated alum. foil	0.33	4.4
coated alum. foil	0.52	4.5
coated alum. foil	0.31	3.7

Table VI.2. Mass median aerodynamic diameters and geometric standard deviations of impacted soot with different collection surfaces (acetylene flow rate 43.3 cc/min).

collection time is chosen for each fuel flow rate to keep the total mass deposit less than 2 mg per stage.

The mass median aerodynamic diameters and standard deviations for the coated surfaces at different collection times and different fuel flow rates are given in Table VI.3. Figure VI.1 is a plot of the mass median diameter as a function of fuel flow rate. Only data points from soot collected on coated aluminum foil are plotted.

A reason for the range in mass median aerodynamic diameters calculated for a given fuel flow rate could include sampling problems. But, for these experiments the flow arrangement and sampling flow rate were always the same. A probable explanation for the variation in the mass median aerodynamic diameter could be due to slight variations in the fuel flow rate. A rotameter is used to control the fuel flow rate. Accuracy for a setting is probably around $\pm$ 0.25 cm^3/min. This would affect the mass median aerodynamic diameter somewhat. The burner itself is fairly stable, for periods up to an hour or more. Another possible reason for the variation is since the slope of the line passing through the data points on the log-probability plot is steep, small errors can affect the mass median diameter a lot.

From a weakly sooting flame (39.5 cm^3/min) to a heavily sooting flame (67.5 cm^3/min) the mass median aerodynamic diameter ranges from 0.4 to 8.0 μm or a factor of twenty in aerodynamic diameters. Total soot emission ranges for .014 to .074 g/m^3 or about a factor

Fuel Flow Rate (cc/min)	Mass Median Aerodynamic Diameter (μm)	σ_g
39.5	0.28	5.4
-	0.38	5.0
-	0.23	20
-	0.46	10
-	0.24	3.8
43.3	0.56	9
-	0.59	14
-	0.46	8.5
-	0.43	14
51.0	0.72	-
59.0	2.4	-
-	3.8	-
67.5	8.5	-
-	7.2	-
-	9.6	-
-	9.0	-
-	6.4	-
-	8.2	-
-	8.5	-

Table VI.3. Mass median aerodynamic diameters and geometric standard deviation of impacted soot at different fuel flow rates (a dash in the σ_g column signifies that the data does not fit a log-normal distribution well).

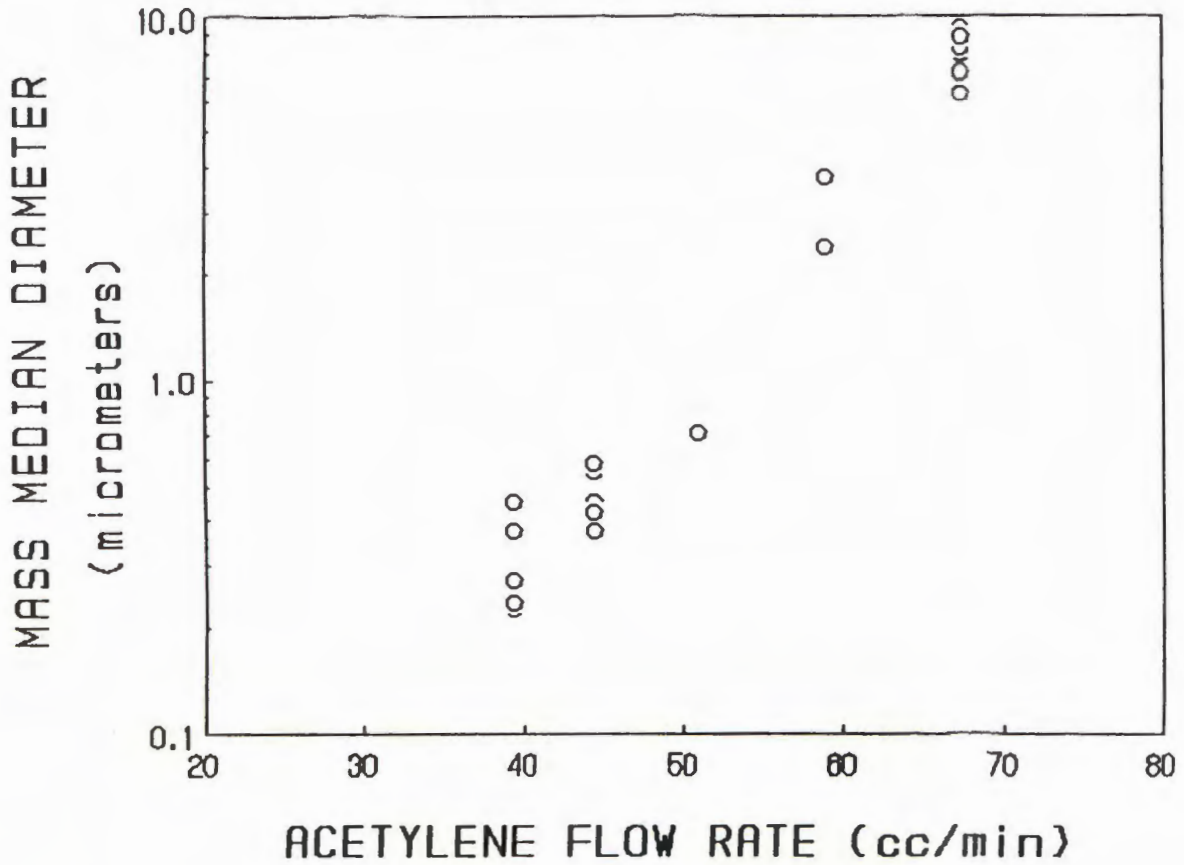

Figure VI.1. Mass median aerodynamic diameters from the cascade impactor versus acetylene flow rate.

of five. Table VI.4 gives the soot emission for measurements at three different fuel flow rates.

In conclusion, the mass median aerodynamic diameter of soot clusters was measured at different fuel settings, and was found to be a strong function of the fuel flow rate. Particle bounce and re-entrainment of soot particles is expected to have an effect on the mass median diameter above loadings of 2 mg per stage. An impaction surface coated with silicone oil appears to limit particle bounce and re-entrainment.

Acetylene Flow Rate (cc/min)	Soot Yield (grams soot/grams fuel)
39.5	0.008
-	0.011
-	0.008
-	0.014
-	0.015
-	0.015
43.3	0.034
-	0.042
-	0.029
-	0.041
-	0.034
-	0.042
67.5	0.080
-	0.085
-	0.069
-	0.080
-	0.072
-	0.062
-	0.070
-	0.074
-	0.088
-	0.077
-	0.069

Table VI.4. Soot yield at different acetylene flow rates.

VII. MEASUREMENTS OF ELECTRICAL MOBILITY CLASSIFIED AGGLOMERATES

In chapter V, the electrical mobility distributions of soot agglomerates formed at different acetylene flow rates were presented. In this chapter measurements of electrical mobility classified agglomerates are presented. These measurements focus on the relationship between the diffusion coefficients, mass equivalent diameter, structural size, and effects of structural changes of mono-mobility agglomerates to the electrical mobility equivalent diameter.

Log mean diffusion coefficients of electrical mobility classified agglomerates were obtained from measurements with the diffusion battery. The acetylene flow rate in this experiment is fixed at 39.5 cc/min. The results indicate that for the selected DMA rod voltages corresponding to electrical mobility equivalent diameters of 0.036, 0.051, 0.07, and 0.108 μm, the log mean diffusion coefficients in terms of equivalent spherical particle diameters are 0.041, 0.061, 0.090, and 0.125 μm respectively.

Mass equivalent diameters of electrical mobility classified agglomerates are obtained from mass concentration and number concentration measurements at three different fuel flow rates, 39.5, 43.3, and 67.5 cc/min. The electrical mobility equivalent diameters ranged from 0.11 to 0.92 μm, while the mass equivalent diameters ranged from 0.12 to 0.42 μm. The results indicate that the electrical mobility equivalent diameter is greater than the mass

equivalent diameter for electrical mobility equivalent diameters greater than 0.35 μm.

Geometric mean sizes (in terms of longest length and width measurements) of electrical mobility classified agglomerates were determined. For singly charged clusters, the average geometric mean sizes were determined to be 0.105, 0.195, 0.490, and 0.685 μm for DMA rod voltages corresponding to electrical mobility equivalent diameters of 0.07, 0.10, 0.20, and 0.40 μm.

Electrical mobility classified agglomerates were subjected to a condensation/evaporation cycle which changes the structure of the agglomerates from a low density structure to a more compact structure. The shift in the electrical mobilities for agglomerates with electrical mobility equivalent diameters of 0.32 and 0.20 μm is measured. The average reduction in the electrical mobility equivalent diameter between the unprocessed and processed agglomerates was 10%.

VII.1 Diffusion Coefficients

In this experiment, the log mean diffusion coefficients of electrical mobility classified agglomerates with fixed electrical mobilities are measured. Measurements of the fractional penetration of the agglomerates through a GCAF diffusion battery at different flow rates through the battery are analyzed to obtain the log mean diffusion coefficient.

Sheath and excess air flow rates through the DMA were 20 l/min, and the aerosol and outlet flow rates were 2.0 l/min. The outlet stream from the DMA was directed to a tee where the flow was split in two. The flow rate to the diffusion battery was controlled by controlling the flow rates at this point. Concentration measurements for flow exiting a stage and the blank were made with the CNC. The acetylene flow rate was fixed at 39.5 l/min. At this fuel flow rate, the soot ribbon is just barely visible. The electrical mobilities were selected such that the electrical mobility equivalent diameters were 0.036, 0.051, 0.070, and 0.108 μm.

The data is presented in the same manner as the data for the unclassified aerosols at pre-sooting conditions. The apparent diffusion coefficient is plotted as a function of penetration. Figures VII.1 to VII.4 are plots of the results. The data points show some scatter, but there is no observed trend in the data. The different symbols correspond to different stages of the diffusion battery. The dashed lines correspond to simulated penetration curves of a monodisperse aerosol with a diameter equal to the electrical mobility equivalent diameter. All the data points fall below these lines owing to the presence of larger multiple charged agglomerates. This results in a mean diffusion coefficient which is smaller than the diffusion coefficient corresponding the electrical mobility equivalent diameter. The log mean diffusion coefficients are estimated by averaging the apparent diffusion coefficients over

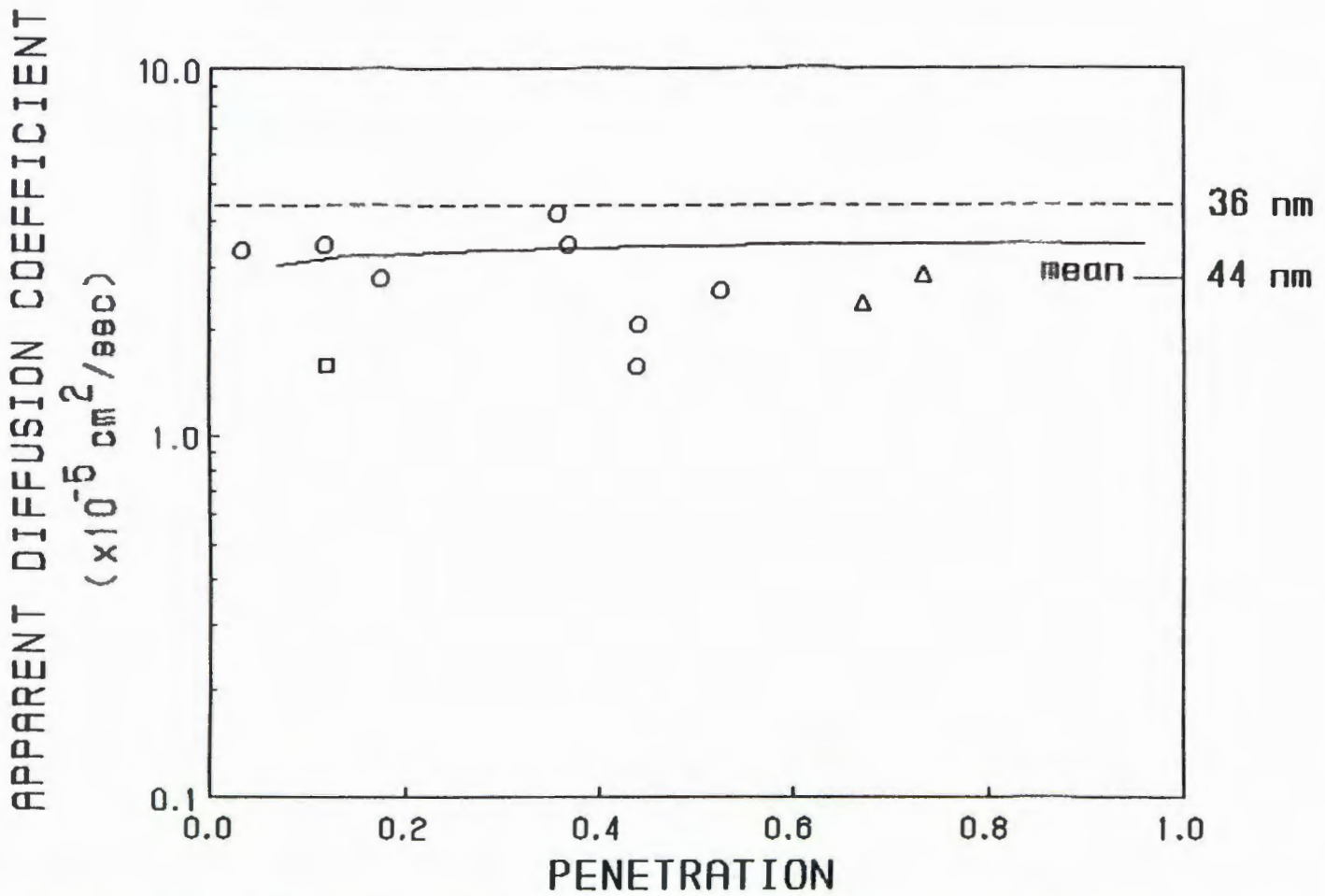

Figure VII.1. Diffusion coefficients of electrical mobility classified agglomerates with an electrical mobility of 1.73×10^{-3} cm^2/volt-sec. The acetylene flow rate was 39.5 cc/min. The dashed line corresponds to the penetration curve of monodisperse particles. The solid line corresponds to a simulated penetration curve.

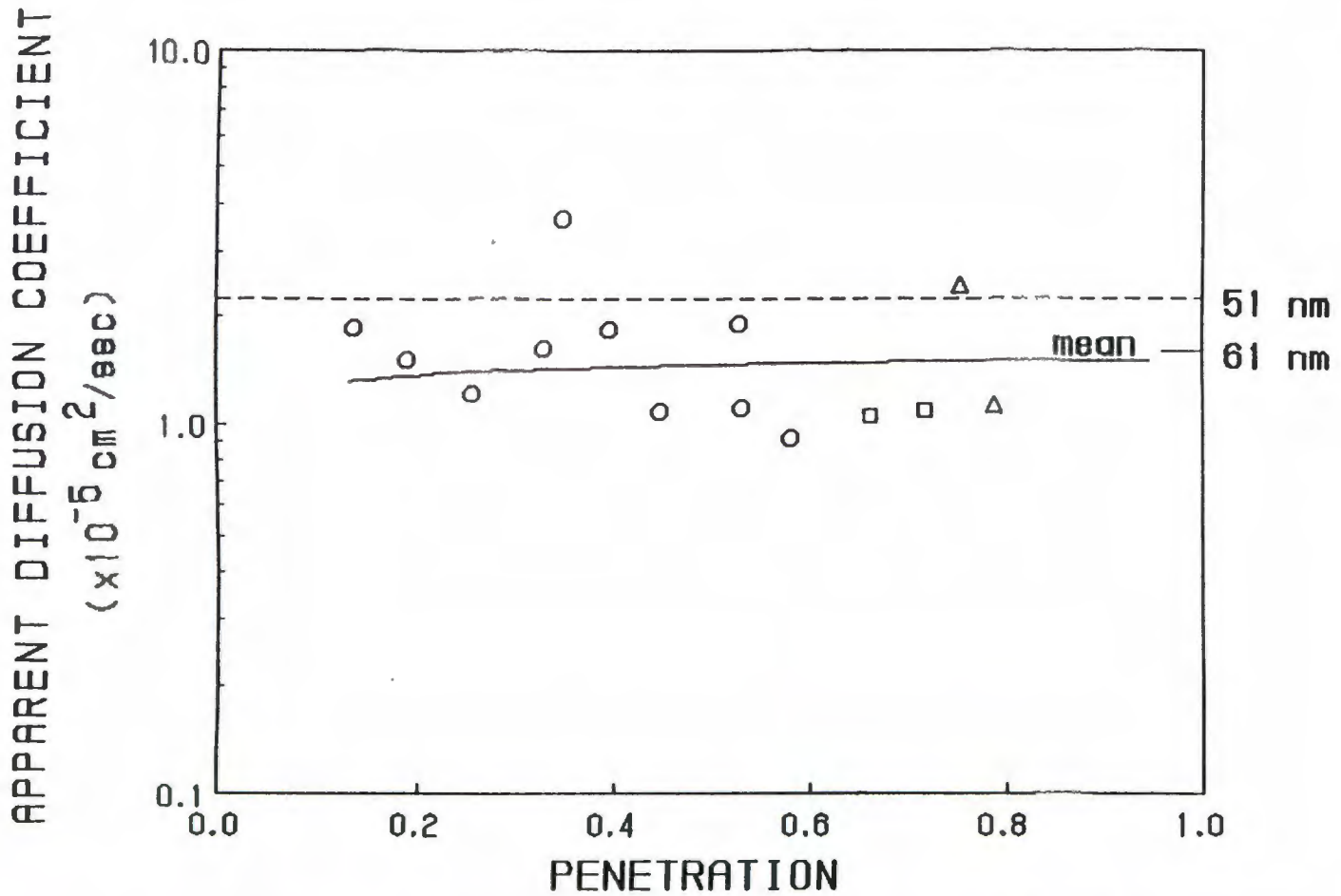

Figure VII.2. Diffusion coefficients of electrical mobility classified agglomerates with an electrical mobility of 9.04×10^{-4} cm^2/volt-sec. The acetylene flow rate was 39.5 cc/min. The dashed line corresponds to the penetration curve of monodisperse particles. The solid line corresponds to a simulated penetration curve.

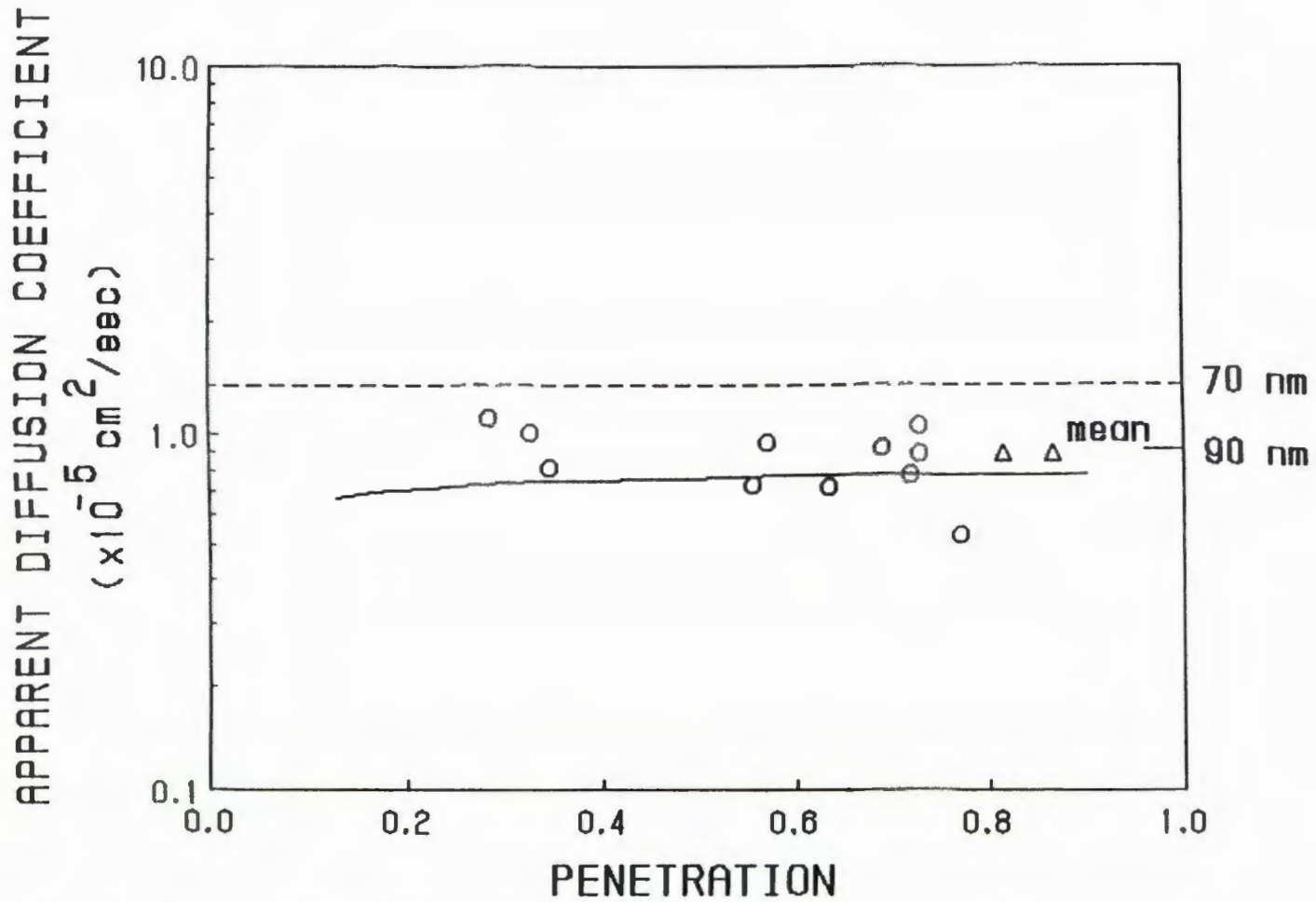

Figure VII.3. Diffusion coefficients of electrical mobility classified agglomerates with an electrical mobility of 5.06×10^{-4} cm^2/volt-sec. The acetylene flow rate was 39.5 cc/min. The dashed line corresponds to the penetration curve of monodisperse particles. The solid line corresponds to a simulated penetration curve.

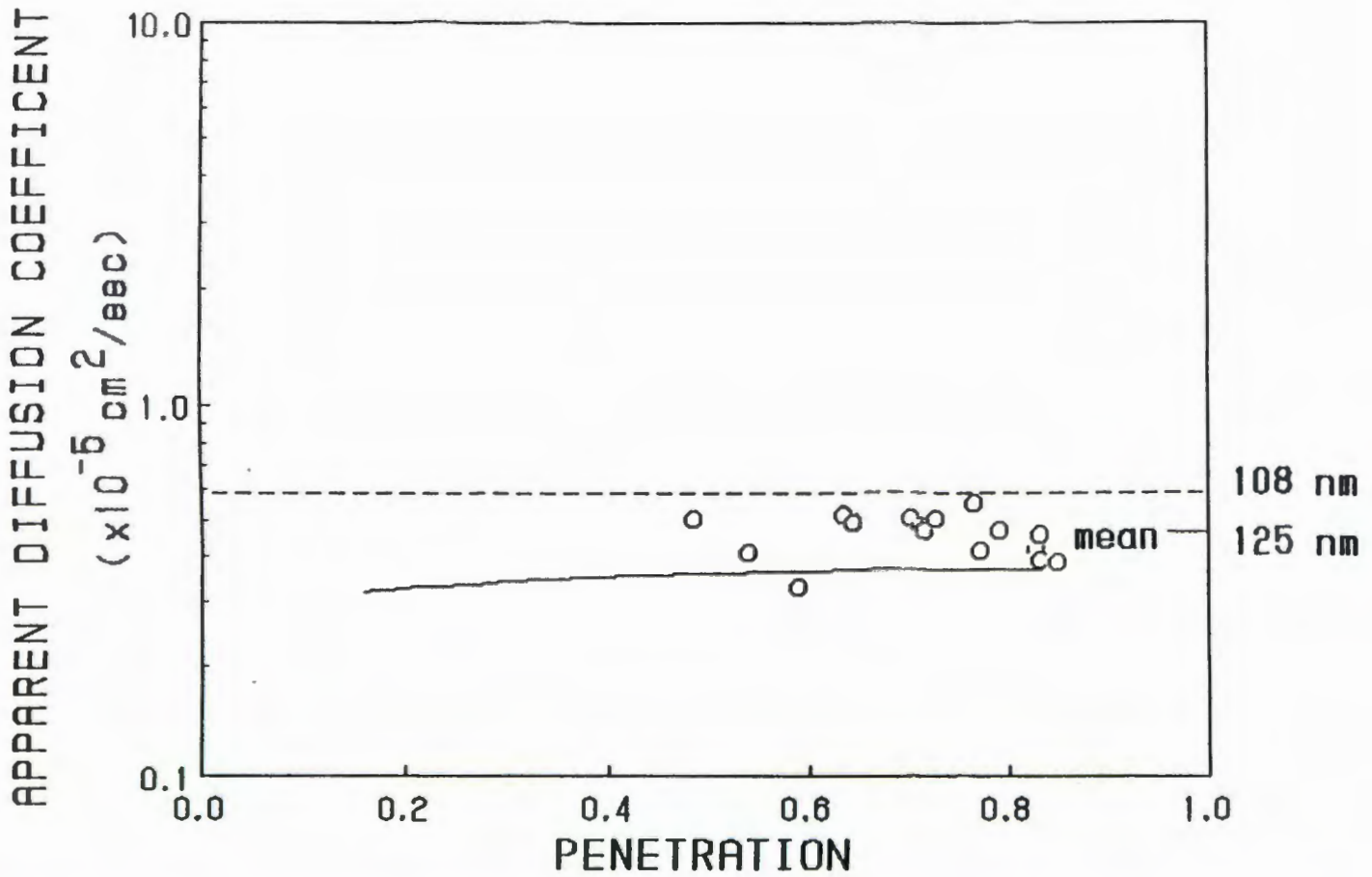

Figure VII.4. Diffusion coefficients of electrical mobility classified agglomerates with an electrical mobility of 2.29×10^{-4} cm^2/volt-sec. The acetylene flow rate was 39.5 cc/min. The dashed line corresponds to the penetration curve on monodisperse particles. The solid line corresponds to a simulated penetration curve.

the range of measured penetrations. For the first three plots, the data points fall within a wide range of penetrations, but for the last plot (electrical mobility equivalent diameter of 0.108 μm) the data points are limited to a narrow range of penetration, thus less confidence is placed on this measurement. The log mean diffusion coefficients in terms of equivalent sphere diameters are 0.041, 0.061, 0.090, 0.125 μm.

VII.2 Mass Mean Equivalent Diameters

The number and mass concentrations of electrical mobility classified agglomerates were measured with the CNC and the microbalance, respectively. Mass mean equivalent diameters are determined as a function of the fuel flow rate and rod voltage from the ratio of the mass concentration to the number concentration. Three fuel flow rates (39.5, 43.3, and 67.5 cc/min) were specified. Sheath and excess air were set at 2.7 l/min, and the aerosol and outlet flow rates were set at 0.5 l/min.

The number concentration measurement for a specified acetylene flow rate and rod voltage was taken immediately after the mass concentration measurement. The sizes of the classified particles were sufficiently large so that the CNC sensing efficiency was near 100%. The average sampling time for a mass concentration measurement was approximately 2 min. It is estimated that the accuracy of the mass concentration measurement from the quartz

crystal microbalance is within 10%, since the instrument resolution is good at the concentrations measured here.

The values for the measured number and mass concentrations are given in Table VII.1. The acetylene flow rate, rod voltage and corresponding electrical mobility equivalent diameter are also given in the Table. The mass mean diameter of the electrical mobility classified agglomerates was calculated assuming a density for compact soot of 1.8 g/cc.

It was found that for agglomerates with an electrical mobility of 8.13×10^{-5} cm^2/volt sec or more (electrical mobility equivalent diameter of 0.21 μm or less), the electrical mobility equivalent diameter is within the experimental uncertainty of the mass mean equivalent diameter. While, for agglomerates with an electrical mobility of 4.43×10^{-5} cm^2/volt sec or less (electrical mobility equivalent diameter of 0.35 μm or more), the electrical mobility equivalent diameter is larger than the mass mean equivalent diameter. The values of the mass mean equivalent diameter are a function of the size distribution of the classified agglomerates. At different fuel flow rates, the size distribution of the agglomerates differs, thus the mass equivalent diameters differ. For example, at a rod voltage of 1000 volts, the electrical mobility equivalent diameter is 0.165 μm, while the mass mean equivalent diameters are 0.161, 0.193, and 0.21 μm for the acetylene flow rates of 39.5, 43.3, and 67.5 cc/min respectively.

Acetylene Flow Rate (cc/min)	Rod Voltage (volts)	Electrical Mobility Equivalent Diameter (μm)	Volume Equivalent Diameter (μm)
39.5	500	0.11	0.117
-	750	0.14	0.141
-	1000	0.165	0.161
-	1500	0.21	0.180
-	3000	0.35	0.230
43.3	1000	0.165	0.193
-	1500	0.210	0.220
-	3000	0.350	0.250
-	5000	0.510	0.302
67.5	1000	0.165	0.210
-	3000	0.350	0.250
-	5000	0.510	0.270
-	7500	0.720	0.36
-	10000	0.920	0.42

Table VII.1. Volume equivalent diameter of electrical mobility classified soot at different rod voltages and acetylene flow rates.

VII.3 Electron Microscopy

Electrical mobility classified agglomerates at different rod voltages were collected by the thermal precipitator on TEM grids. The samples were examined under an electron microscope at a magnification of 15,000X. These samples were collected by Samson, and the size measurement was performed as part of this study. Measurements of the longest length and width of the clusters were used to calculate the geometric mean size of the clusters.

Since the sizes of mono-mobility agglomerates are distributed over a wide range, a criterion for selecting the singly charged agglomerates must be established. Essentially, the agglomerate sizes fall within a range of sizes depending on the agglomerate charge, with the smallest size range corresponding to the singly charged agglomerates. The criterion used in this analysis is that whenever the volume equivalent diameter of an agglomerate is less than the electrical mobility equivalent diameter, the agglomerate is assumed to carry one net charge. Odumade (1983) used this criterion in his analysis of electrical mobility classified propane flame agglomerates. The volume equivalent diameter is calculated from equation I.2 and the estimated average primary particle volume. The average of the geometric mean sizes of the agglomerates for rod voltages corresponding to electrical mobility equivalent diameters of 0.07, 0.10, 0.20, and 0.40 μm are 0.105, 0.195, 0.490, and 0.685 μm respectively.

VII.4 Condensation/Evaporation Processing

In this experiment the change in the electrical mobility of clusters subjected to a condensation/evaporation cycle is measured. In a condensation/evaporation cycle, the structure of the cluster undergoes a rearrangement resulting in a compact structure with a fractal dimension in the range of 2.5 to 3.0 (Mulholland, 1988). This structural change affects the aerodynamic properties of the cluster and the scattering cross section. The change in aerodynamic properties of agglomerates that undergo a structural change is of interest to researchers studying inhalation of agglomerates, where the moisture content in the pathway to the lung is relatively high (van de Vate, 1980). The change in the scattering cross section of the agglomerate is of interest to researchers studying the nuclear winter scenario (Mulholland, 1988).

First the soot is passed through the DMA. The DMA flow rates were set at 8.0 l/min of sheath and excess air, and 1.3 l/min of aerosol inlet and outlet flow rates. The rod voltages were either 4000 or 8000 volts for the different experiments. The electrical mobility classified soot fills up the expansion cloud chamber, which was previously purged with filtered air. The chamber is a 7.5 cm ID PVC tube that is capped with inlet and outlet valves at each end. The volume of the chamber is 9 liters. The inner wall of the chamber is lined with paper that is saturated with water. Once the chamber is filled, the ends are sealed and the chamber is pressurized to 2.74×10^5 Pa (25 psig) with filtered air. A minute or

two is allowed to elapse so that water can diffuse from the walls to the gas phase. A relief valve is opened and the sudden expansion forms a cloud. The soot particles act as condensation nuclei and water droplets form around the soot particles. The aerosol is passed to a diffusion dryer (a tube packed with silica gel) where the water is evaporated leaving the restructured soot particles. This process changes the structure of the soot particles, compacting them into a more dense structure. The processed soot leaves the diffusion dryer and passes back through the DMA, where the electrical mobility distribution is measured.

The experiment was performed with and without the pressurization of the cloud chamber. When the cloud chamber is not pressurized, essentially, the soot passes through the DMA twice with no physical change. The processing stage is a batch process. Since the soot is pushed out of the chamber by incoming clean air, the measured concentration for any given rod voltage will drop in time. Therefore, the measured number concentrations are corrected for this effect.

The results are presented in Figures VII.5 to VII.7. The upper data points corresponds to the unprocessed soot while the lower data points corresponds to processed soot. The shift in the electrical mobility peaks of the unprocessed soot and the processed soot is a measure of the effects the structural change has on the aerodynamic properties of the agglomerates. Table VII.2 gives the electrical mobility equivalent diameters for the processed and unprocessed

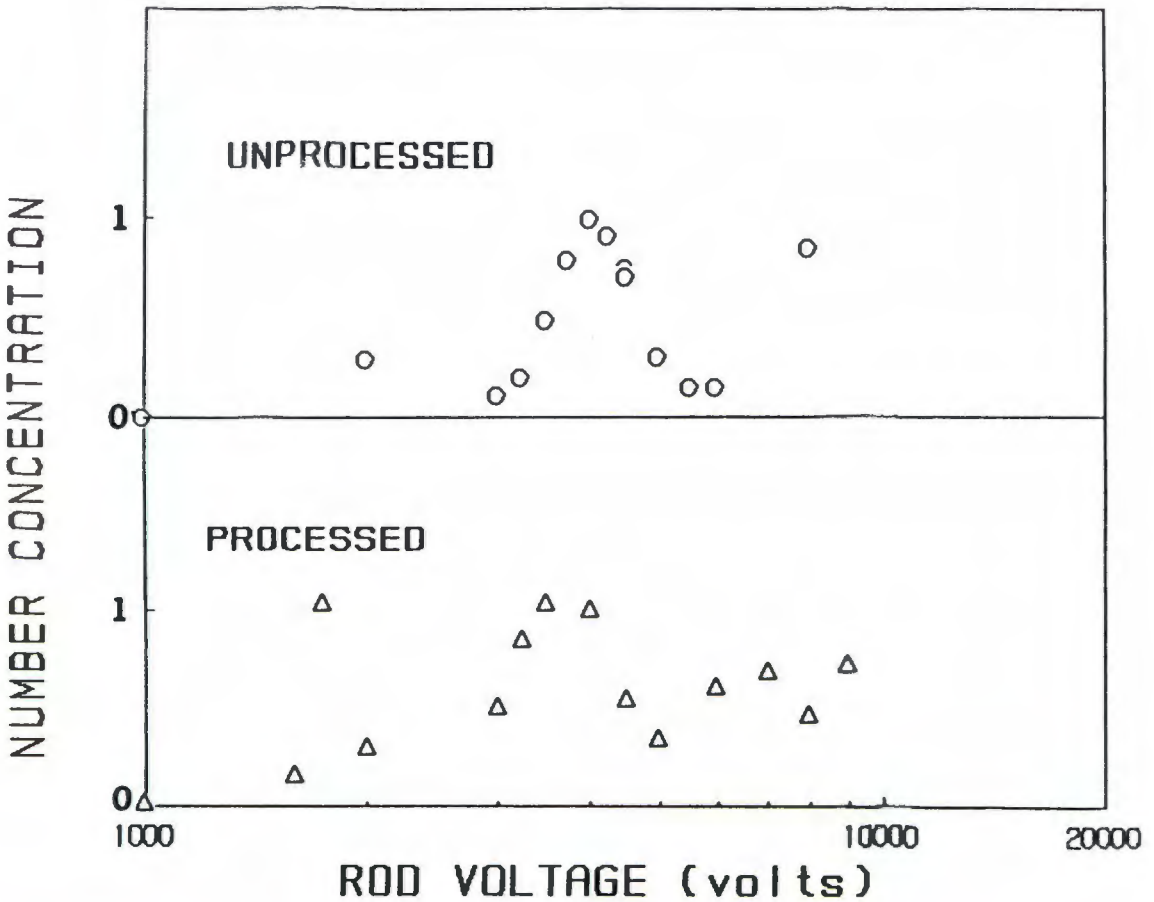

Figure VII.5. Electrical mobility distribution of condensation/evaporation processed soot with an initial rod voltage of 8000 volts, and an acetylene flow rate of 39.5 cc/min. The number concentration has been normalized by the value at 8000 volts.

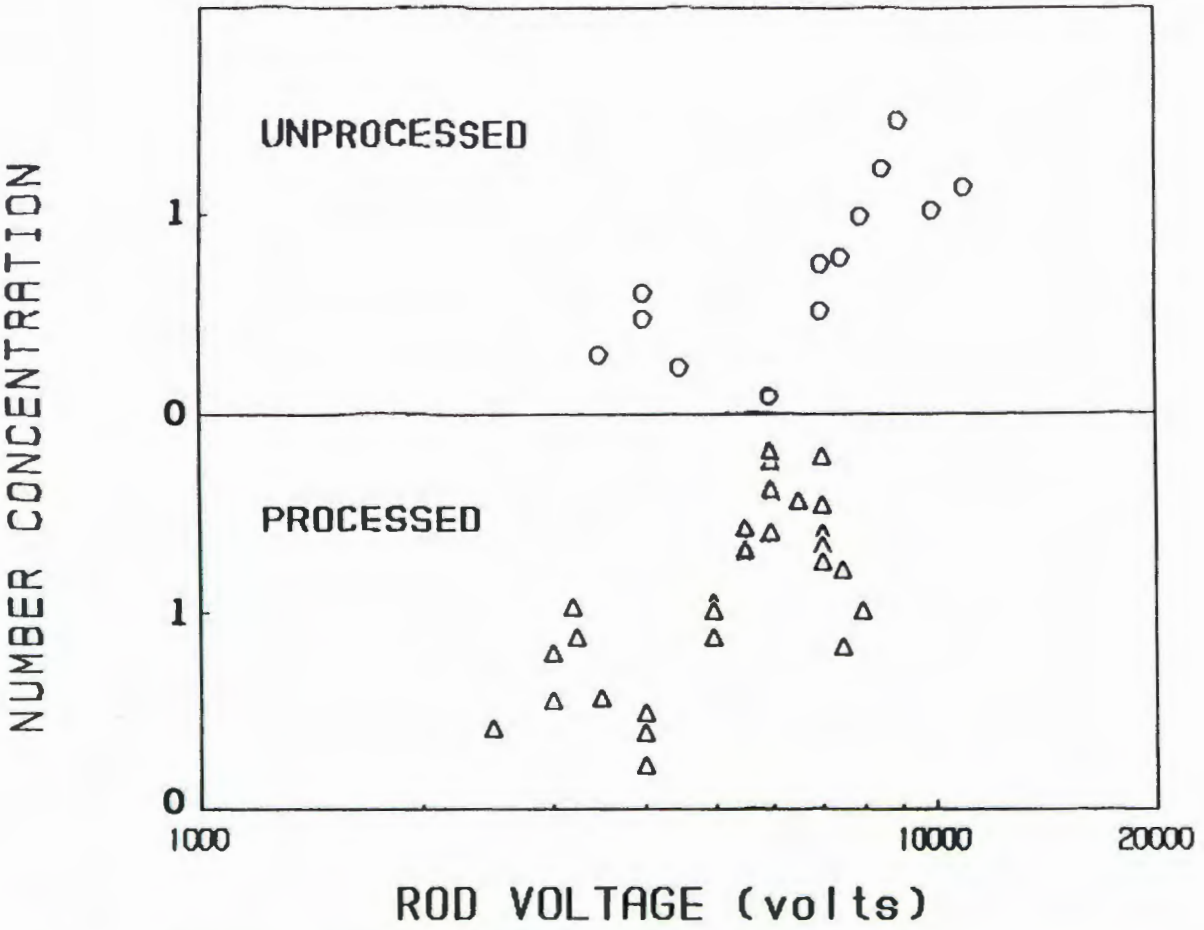

Figure VII.6. Electrical mobility distribution of condensation/evaporation processed soot with an initial rod voltage of 8000 volts, and an acetylene flow rate of 43.3 cc/min. The number concentration has been normalized by the value at 8000 volts.

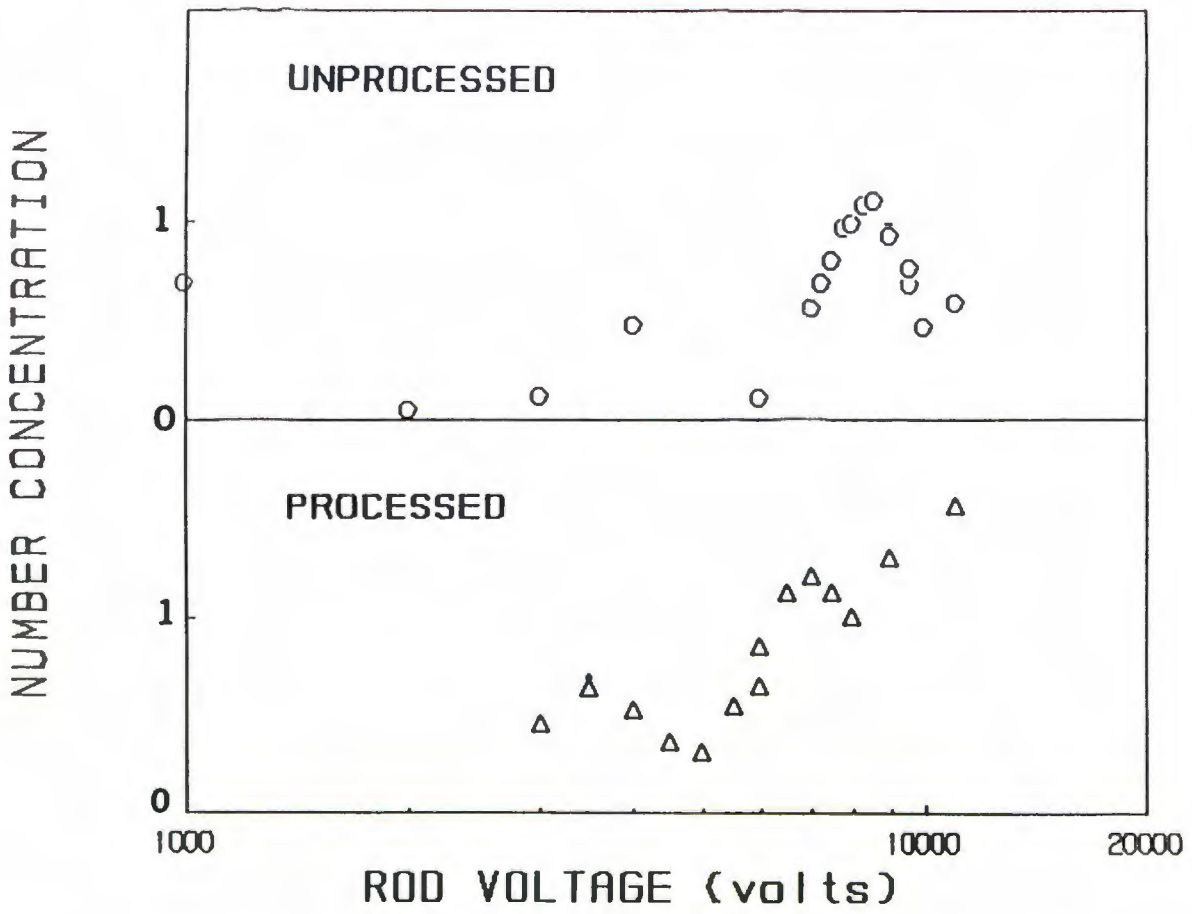

Figure VII.7. Electrical mobility distribution of condensation/evaporation processed soot with an initial rod voltage of 4000 volts, and an acetylene flow rate of 43.3 cc/min. The number concentration has been normalized by the value at 4000 volts.

Acetylene Flow Rate (cc/min)	Rod Voltage (volts)	Unprocessed Equivalent Diameter (μm)	Processed Equivalent Diameter (μm)	% Change
39.5	4000	0.20	0.17	15
-	8000	0.32	0.29	9
43.3	4000	0.20	0.19	5
-	4000	0.20	0.18	10
-	8000	0.32	0.29	9
-	8000	0.32	0.30	6

Table VII.2. Electrical mobility equivalent diameters of condensation/evaporation cycle restructured agglomerates.

soot. The average reduction in electrical mobility equivalent diameter was 10%. The shift in the peak mobility is insensitive to multiple charged particles since the fraction of multiple charged particles is small.

VIII. DISCUSSION

The experimental results that were presented in the previous chapters include measurements of particles over a wide size range. In this chapter, the particle size measurements from different instruments for primary particles formed at pre-sooting conditions of the flame are compared. For the agglomerates, results from the previous chapters are compared to model calculations.

Many theoretical advances for predicting agglomerate properties have been made since the early 1980's with the development of fractal theory for agglomerates. The validity of models based on fractal concepts are tested with measured properties of agglomerates. Comparisons of measured agglomerate friction coefficients with simple models are presented. The agglomerate size distribution from a weakly sooting flame (fuel flow rate 39.5 cc/min) is compared to simulated agglomerate size distributions. The relationship between the aerodynamic diameter of inertially separated agglomerates to the structural size is compared to a simple model for the aerodynamic diameter of agglomerates. Measured log mean diffusion coefficients and mass mean diameters of electrical mobility classified agglomerates are compared to values predicted from size distribution measurements obtained from electrical mobility distributions.

VIII.1 Comparison of Measured Sizes of Primary Particles

Comparisons between the measured sizes of particles formed in the pre-sooting flame conditions are made. The measured size distribution parameters include the log mean diameter measurements from the diffusion battery, the log mean diameter and geometric standard deviation measurements from the DMA, and mass mean diameter from the mass and number concentrations measurements. The fuel flow rate chosen for the comparison is 31.5 cc/min, since measurements were made at this fuel setting for all the instruments above.

The diffusion coefficients measurements indicate that the log mean diffusion coefficients, and thus log mean particle diameters are essentially independent of the fuel flow rate in the pre-sooting region (up to fuel flow rates of 36 cc/min). At a fuel flow rate of 31.5 cc/min, the log mean particle diameter was determined to be 11.0 nm by the diffusion battery (Figure IV.4). From the electrical mobility measurements, the log mean particle diameters were determined to be 13.9 and 13.84 nm with geometric standard deviations, σ_g, of 1.33 and 1.26 respectively for two repeated mobility distributions. From the mass and number concentration data (Figures III.1 and III.2) the mass mean diameter was determined to be 26 nm at this fuel flow rate.

The log mean particle diameters from the diffusion battery and the DMA are both number average means and can be compared directly. The electrical mobility measured log mean diameter is approximately 26 % greater than the diffusion battery measurement. One possibility for this discrepancy is that since the number count of

the mobility classified particles depends on the absolute value of the CNC measurement, the size distribution may be skewed to larger sizes because the particle sensing efficiency of the CNC drops off at small particle diameters (less than 10 nm), thus under-counting the small particles. The diffusion coefficient measurements depend on the ratio of two CNC readings, thus under counting of small particles does not affect measured penetration value. Errors in the flow and voltage meter readings can also affect the log mean size measurements of the DMA, but the errors are probably small. The value for the geometric standard deviation from the electrical mobility measurements should be regarded as an overestimation since particle diffusion in the DMA tends to broaden the measured size distribution of very small particles.

The mass mean diameter of the primary particles is determined from the ratio of the mass concentration to the number concentration measurements. A soot density of 1.8 g/cc was specified for the conversion of average particle mass to diameter. The mass mean diameter was calculated to be 26 nm. This value is much higher than the log mean diameters from the diffusion battery and the DMA. For such a monodisperse aerosol it is expected that the mass mean diameter would be somewhat closer to the number mean diameter. If the values of the log mean diameter and geometric standard deviation from the electrical mobility measurements are used to estimate the mass mean diameter assuming a log-normal distribution, a mass mean diameter of 17 nm is predicted. Possible explanations of the difference between the values include the accuracy of the mass and

number concentration measurements. The number concentration is surely underestimated due to the decrease in the counting efficiency of the CNC at particles sizes below 10 nm, which would lead to some overestimation of the mass mean diameter. The accuracy of the mass concentration measurement is suspect, since the lower limits of the instrument resolution are being approached. The accuracy of the microbalance is probably no better than ± 25% in this region. It can not be ruled out that there is a small number of agglomerates which would account for a large part of the mass.

In conclusion, the best estimate of the log mean particle diameter is from the diffusion battery measurements (11.0 nm). The width of the size distribution is obtained from the DMA measurements. The geometric standard deviation (σg) is estimated to be about 1.3.

VIII.2 Comparison of Measured Log Mean Diffusion Coefficients to Predicted Values

In section VII.2, the log mean diffusion coefficient measurements for electrical mobility classified agglomerates were presented. The fuel flow rate was set at 39.5 cc/min. The apparent diffusion coefficients for a given electrical mobility setting showed no systematic trend over the penetration range of 20 to 80%. The log mean diameters (from the log mean diffusion coefficients) were less than the electrical mobility equivalent diameters due to the effects of multiple charged agglomerates. Simulations of the

DMA and the diffusion battery were performed for an assumed size distribution and compared to the measured values of the log mean diffusion coefficients.

The particle mobilities (B) of the particles exiting the DMA are related to the electrical mobility and net charge. The particle mobility is proportional to the electrical mobility divided by the number of net charges residing on the particle. Thus, the particle mobilities of any ith charged particle is known for a given electrical mobility. The particle mobility is related to the particle diffusion coefficient through the Stokes-Einstein equation. The log mean diffusion coefficient of electrical mobility classified particles is given by

$$\ln D = X1 \ln D1 + X2 \ln D2 + X3 \ln D3 + \ldots \quad \text{(VIII.1)}$$

X_i is the fraction of i charged particles leaving the DMA and D_i is the diffusion coefficient of a particle with i charges. This series is truncated after four terms because the probability of a particle with more than four net charges residing on it are very small for the particle size range considered here.

The values of X_i can be determined when a size distribution and charge distribution are specified. In section V.3 the size distribution was estimated from the electrical mobility distribution of agglomerates, at a fuel flow rate of 39.5 cc/min. It was assumed that the charge distribution of the agglomerates followed the

Boltzmann charge distribution. From the size distribution and the charge distribution, the fraction of particles with an electrical mobility equivalent diameter d_i corresponding to a diffusion coefficient D_i can be calculated from the charge probability and the fraction of particles of size d_i. Now, with the X_i's specified for any particle size, a log mean diffusion coefficient of electrical mobility classified agglomerates can be calculated from equation VIII.1.

The predicted log mean diameters 0.041, 0.065, and 0.095 μm are within 7% of the corresponding measured values of 0.044, 0.061, 0.090 μm, which is a good prediction of the measured values. The agreement between the measured log mean diameter of 0.125 μm and the predicted value of 0.147 μm, for the highest voltage setting is not very good. The fraction of singly charged particles at this electrical mobility appears to be under predicted by the assumed size and charge distributions.

In Figures VII.1 to VII.4 the apparent diffusion coefficients show some scatter but there is no apparent systematic trend. Apparent diffusion coefficients are simulated from the size distribution of the electrical mobility classified agglomerates (acetylene flow rate 39.5 cc/min). The simulated penetration curve is compared to the data points to confirm the lack of a systematic trend with the apparent diffusion coefficients.

The simulated penetration of the electrical mobility classified agglomerates for a given electrical mobility is given by

$$Pt\ (overall) = X1\ Pt1 + X2\ Pt2 + X3\ Pt3 + X4\ Pt4 \ldots . \quad (VIII.2)$$

Pti are the individual fractional penetrations through a stage of the diffusion battery calculated for mono-size particles with a diffusion coefficient D_i. The values are calculated for specified flow rates from the Gormley-Kennedy equations. Different flow rates through the battery are specified such that the entire penetration range (Pt (overall)) is covered. The series is truncated after four terms. The different simulated penetrations and flow rates are treated as raw data. Apparent diffusion coefficients are calculated. The simulated values for the different electrical mobility settings correspond to the solid curves on Figures VII.1 to VII.4. The simulated curves show a very slight systematic trend. At low penetrations, the apparent diffusion coefficients are slightly lower than the mean value. This result is fairly consistent with the measured values, since the small systematic trend would not be detectable because of the scatter in the data.

In conclusion, the simulated log mean diffusion coefficients and penetration curves compare well with three smallest measured values. All predicted log mean diffusion coefficients are smaller than the measured values with the exception of the smallest sized particles. The most questionable assumption made was to assume the agglomerate charge distribution is given by the Boltzmann distribution. The

lack of charging information for clusters requires that some assumption be made and this seemed the most logical choice. Since the simulated values and the measured values are reasonably close for most of the measurements, the validity of this charge distribution assumption can not be refuted. This calculation can be repeated for any charge distribution which may become available as the theory of cluster charge distributions develops.

VIII.3 Friction Coefficients Measurements

The particle diffusion coefficient and electrical mobility are related through particle mobility (B). For spherical particles, the particle mobility is given by equation I.5. The inverse of the particle mobility is termed the friction coefficient (cgs units g/sec). In this section, the measured friction coefficients of electrical mobility classified agglomerates are correlated with physical size measurements, and compared to some simple models.

The structural size measurements, from electron microscopy, of electrical mobility classified agglomerates presented in section VII.3 contain the desired information on the relationship between the friction coefficient and size. From the four electrical mobility equivalent diameters, friction coefficients are calculated. The volume equivalent diameters of classified agglomerates with one net charge are calculated from the average geometric mean size measurements, and the fractal relationship in equation I.2, which gives the number of primaries. For this calculation, it is assumed

the volume mean diameter of the primary particles is 0.03 μm. The range of the electrical mobility equivalent diameters is from 0.07 to 0.4 μm. The friction coefficient versus the volume equivalent diameter is plotted in Figure VIII.1. On this log-log plot, the data points are fitted to a straight line. From the best fit line, the calibration between the friction coefficient (fc) and the volume equivalent diameter is

$$fc = 2.95 \times 10^{-6} \ (Dve)^{2.6} \qquad \text{(VIII.3)}$$

Odumade (1983) made similar measurements of mobility classified agglomerates from a propane flame. He individually sized each primary particle in an electrical mobility classified agglomerate from electron microscopy to get a volume equivalent diameter. The range of electrical mobility equivalent diameters from his data was .1 to .15 μm. From the measurement of the volume equivalent diameter of an agglomerate, he estimated the net charge of the agglomerate. His data set consisted of 25 individual agglomerates.

Odumade's data and the values measured here are plotted on the same Figure. In Figure VIII.2 the volume equivalent diameter is plotted against the electrical mobility equivalent diameter. Odumade's data points are represented by circles while the data points of this study are represented by the squares. The dashed and dotted lines correspond to two limiting models relating the friction coefficient to the volume equivalent diameter of agglomerates.

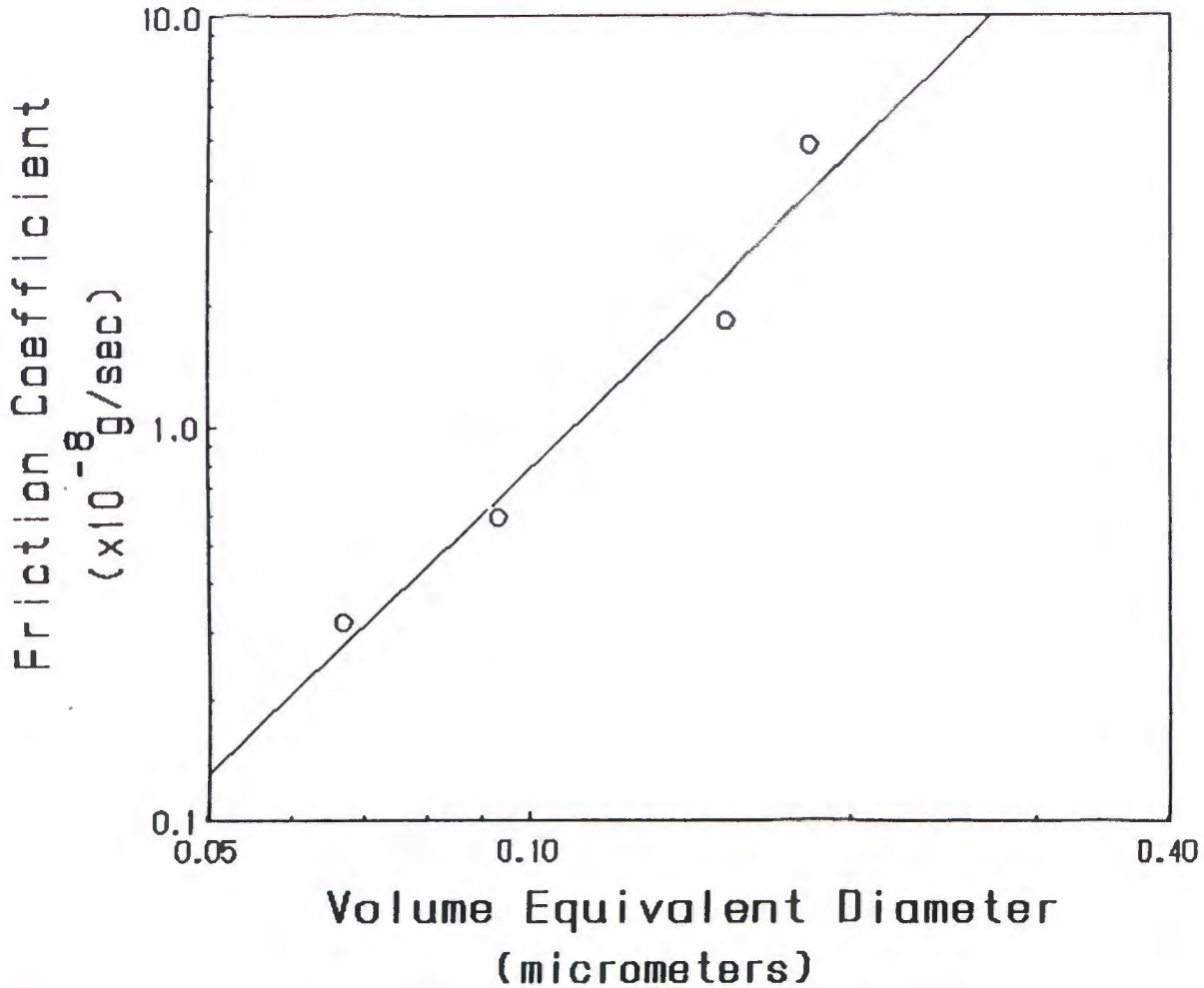

Figure VIII.1. Friction coefficient versus volume equivalent diameter of soot agglomerates. The straight line is a best fit line to the data.

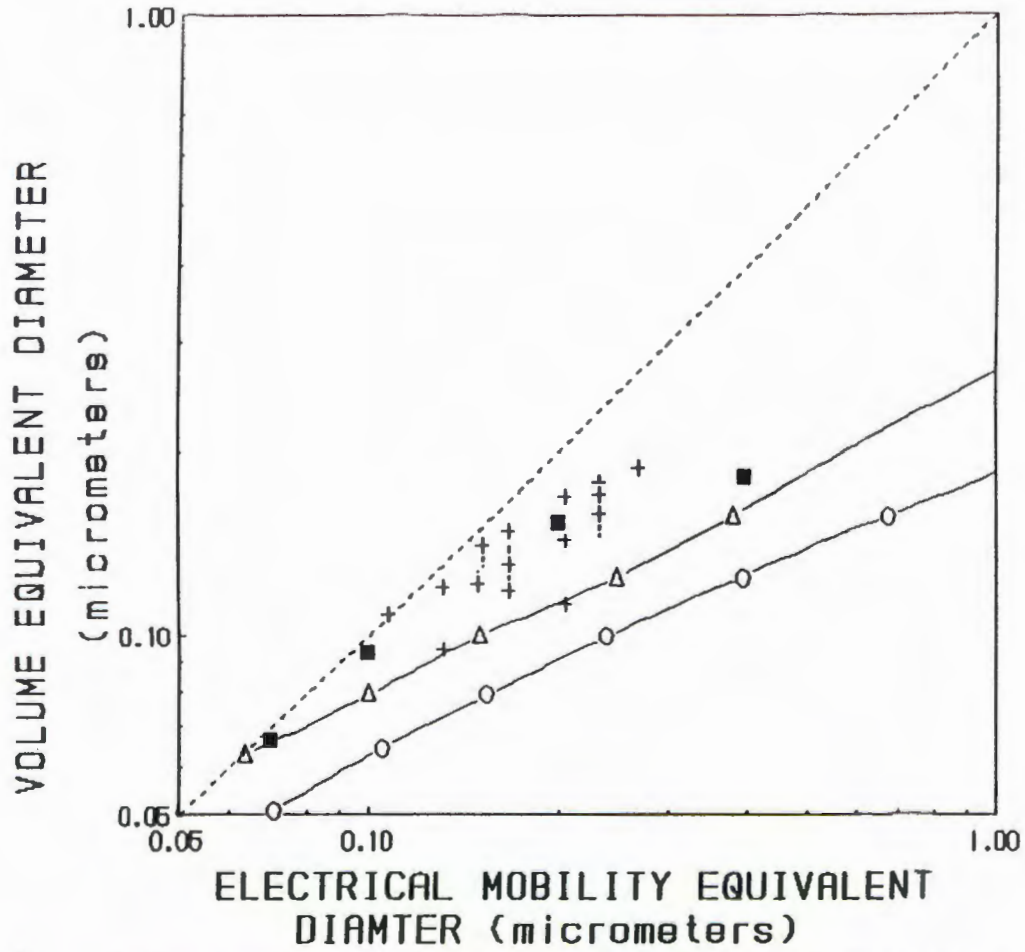

Figure VIII.2. Volume equivalent diameter versus electrical mobility equivalent diameter. The squares represent Samson's data, the crosses represent Odumade's data. The circles represent a free molecular model, where the friction coefficient of the agglomerate is given by the number of primaries times the friction coefficient of a primary particle (dp = 0.03 μm). The triangles represent a continuum flow model, where the radius of gyration of the agglomerate replaces the spherical diameter.

There is good agreement with Odumade's results and results in section VII.3

The first model for the friction coefficients of agglomerates assumes that the friction coefficient is equal to the friction coefficient of the primary particle times the number of primaries in the agglomerate. For both models, the primary particle diameter is assumed to be equal to 0.03 μm in diameter. This means that the Cunningham slip correction is based on the primary particle size. This model is represented by the dashed line in Figure VIII.2 and is based on the assumption of free molecular conditions. The second model assumes that the friction coefficient of the agglomerate is given by replacing the spherical radius in equation I.5 for the particle mobility with the radius of gyration of the agglomerate. This model is represented by the dotted line, and is based on the assumption of hydrodynamic or continuum flow conditions. Both of these simple models do not adequately predict the friction coefficient. In each case the friction coefficient is over-predicted. The first model takes into effect the slip correction of the primary particle, while with the second model, the slip correction of the agglomerate is based on the radius of gyration.

A computer simulation of the momentum transfer of point particles striking simulated fractal agglomerates was performed by Meakin (1989). These simulation results were used here to calculate theoretical values for the friction coefficients of simulated agglomerates. The agglomerates are simulated from a cluster-cluster

aggregation model. The fractal dimension of the simulated agglomerates is 1.95. Point particles representing gas molecules are fired at the agglomerate. The reflection of the point particle is calculated assuming diffuse reflection from the surface. The trajectory of the point particle is calculated and the further collisions are tracked. The angle of the final reflection is used to calculate the momentum transfer. The results are presented as the average net momentum transfer from one point particle for many simulations versus the number of primary particles in an agglomerate.

From these results a particle friction coefficient is calculated based on free molecular conditions. This model assumes that the agglomerates are stationary and the gas molecules strike the agglomerates from one side. The gas molecules are nitrogen molecules, with a mean velocity given by Boltzmann's relationship. The temperature and pressure are fixed at 293 K, and 1 atm. The primary particle diameter is 0.03 μm.

The results for this simulation are plotted on Figure VIII.3. This plot also includes Odumade's results, and a theoretical curve for spherical particles based on Stokes law with slip correction. The results show that the simulation over-predicts the friction coefficients of agglomerates at ambient conditions. There is a lack of experimental measurements of friction coefficient of agglomerates in free molecular conditions which would be expected to compare well with this model.

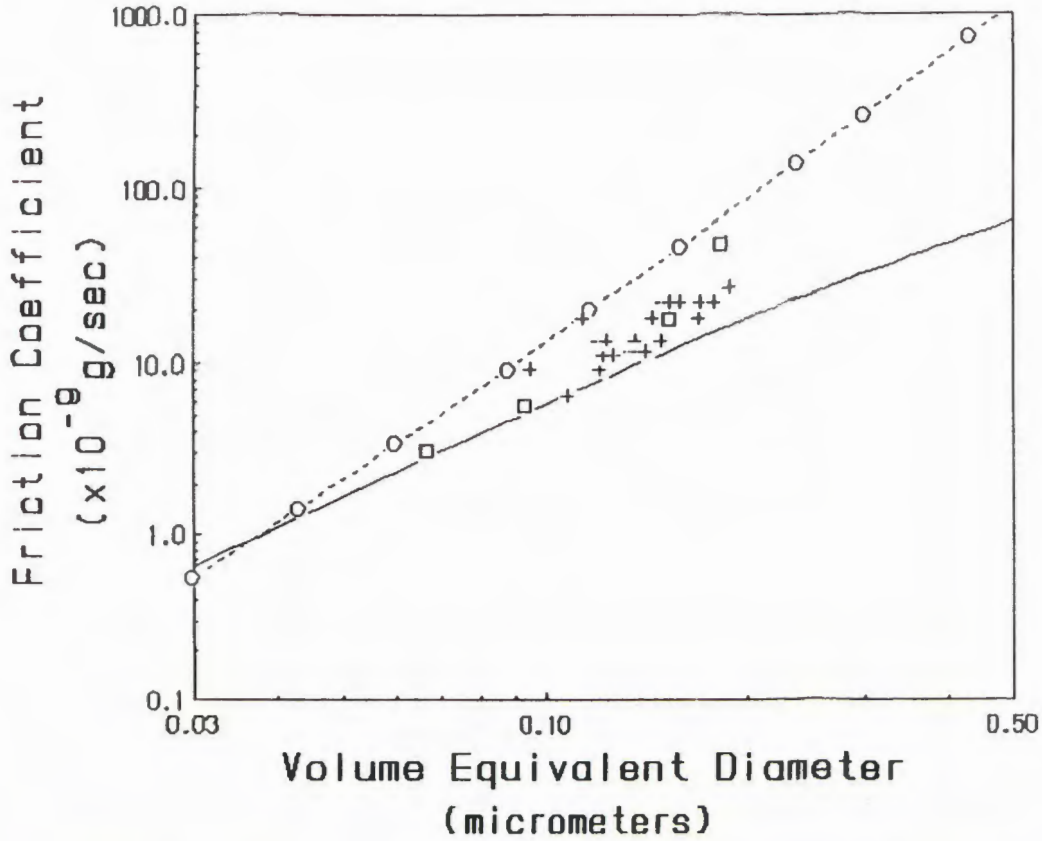

Figure VIII.3. Friction coefficient versus the volume equivalent diameter. The squares represent Samson's data and the crosses represent Odumade's data. The circles represent model predictions for free molecular conditions based on Meakin's simulations. The solid line corresponds to Stokes law with slip correction for spherical particles.

VIII.4 Comparison of Agglomerate Size Distribution to Simulated Cluster Size Distribution Simulations

In this section, the agglomerate size distribution from the electron microscopy of thermally precipitated soot (fuel flow rate 39.5 cc/min) is compared to simulated cluster size distributions. The simulation is described briefly below.

Mulholland et. al. (1988) have simulated the cluster size distribution for the agglomeration of monodisperse particles. Their goal was to simulate the agglomeration process in a flame. At typical flame temperatures (1500 K) the mean free path of the gas molecules is on the order of 300 nm. Under these condition the Knudsen number is small for primary particles with diameters < 30 nm. This particle motion is termed free molecular. The particle dynamics are governed by the Langevin equation

$$d\ (m\ v_x)/dt = -m\ B\ v_x + f_x \qquad \text{(VIII.4)}$$

where m is the particle mass, v_x is the particle velocity, B is the particle mobility, and f_x is a stochastic force satisfying the relationship $\langle f_x \rangle = 2BmkT$, where k is Boltzmann's constant. The model consisted of following the collisions of 8000 primary particles in a box. The individual primaries are randomly dispersed in the box at the beginning of the simulation. At each time step, new trajectories are calculated and agglomeration of particles is

recorded. The rule for agglomeration is that whenever particles touch they stick together and move as a rigid assembly. The friction coefficient of a cluster of k spheres is estimated as k times the friction coefficient of a primary particle. The average fractal dimension of the simulated agglomerates was measured as 1.91. The cluster size distribution is followed for each time step. The results of 5 simulations are averaged.

The cluster size distributions at different times are tested for a self-preserving form. The term self-preserving means that the shapes of the distribution at different times are similar when reduced by a scaling factor. To test for a self-preserving form, the size distributions at different times are plotted in terms of similarity variables ψ and η [Friedlander (1977)] given below.

$$\frac{\Delta n}{\Delta k} = \frac{N_0}{k_{ave}^2} \psi(\eta) \qquad \text{(VIII.5)}$$

$$\eta = k / k_{ave} \qquad \text{(VIII.6)}$$

$\Delta n/\Delta k$ is the cluster size distribution, N_0 is the total number of primary particles, k is the number of primaries in a cluster, and k_{ave} is the average number of primaries in a cluster. The simulation results indicate that the cluster size distribution is consistent with a self-preserving form.

The measured size distribution of the thermally precipitated soot collected at a fuel flow rate of 39.5 cc/min is compared to the simulated size distributions. The measured cluster size distribution is transformed from a function of the geometric mean size to the number of primaries in an agglomerate through equation I.2. With the agglomerate size distribution in terms of the number of primaries, the average agglomerate size in terms of the number of primaries is calculated to be 37. Figure VIII.4 is a plot of two simulated size distributions and the measured size distribution in terms of similarity variables. For the two simulations, the average cluster sizes in terms of primary units are 29 and 98 respectively. It appears that the three size distribution fall on the same curve which would support the conclusions that the model is a good predictor of the agglomerate size distribution from a laminar diffusion flame, and that the size distributions show a self-preserving form.

VIII.5 Comparison of Measured Mass Mean Diameters to Predicted Values

In section VII.1, the mass mean diameters of electrical mobility classified clusters were measured. For a given fuel flow rate and a set electrical mobility, measurements of the mass and number concentration were used to calculate a mass mean diameter. In this section, the relationship between the friction coefficient of an agglomerate and the volume equivalent diameter from VIII.3 is used along with the agglomerate size distributions from the

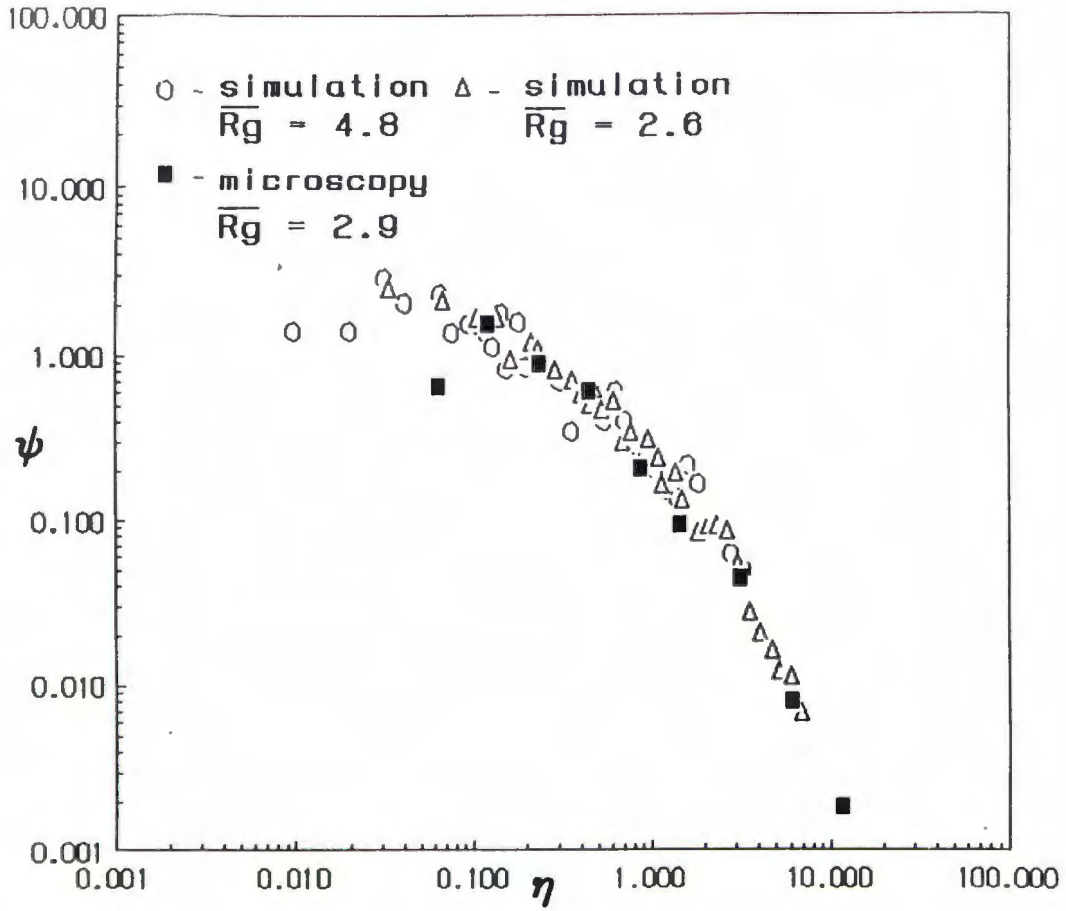

Figure VIII.4. Agglomerate size distribution plotted in terms of similarity variables. The dark squares correspond to the measured size distribution from electron microscopy. The normalized mean radius of gyration for each simulation and the microscopy are given. For Rg = 2.6, 2.9, and 4.8, the corresponding number of primaries are 29, 37, and 98 respectively.

electrical mobility distributions to predict the measured values of the mass mean diameters.

The mass mean diameter of electrical mobility classified soot is given by

$$Dvem(j)^3 = \Sigma\ X(i,j)\ Dve(i,j)^3 \qquad \text{(VIII.7)}$$

Dvem is the mass mean diameter, Dve is the volume equivalent diameter and X(i,j) is the fraction of ith charged particles exiting the DMA. The subscript j indicates different rod voltage and burner fuel flow rate combinations and the subscript i indicates the number of net charges. For a given rod voltage, the electrical mobility of the particles exiting the DMA is known. The friction coefficients of the 1, 2, 3, ... charged particles is known through the relationship between electrical mobility, particle charge and friction coefficient. The volume equivalent diameter (Dve(i,j)) of an agglomerate with a given friction coefficient is determined from the calibration curve from section VIII.3.

The fraction of particles with i charges exiting the DMA for a given rod voltage and burner fuel flow rate is estimated from the size distribution curves of the electrical mobility classified agglomerates. Recall that the electrical mobility distributions for burner fuel settings of 39.5, 43.3, and 67.5 cc/min were measured and size distributions were obtained from the electrical mobility distributions. The assumption that the agglomerate charge

distribution is given by the Boltzmann charge distribution of the electrical mobility diameter was made. The lack of charging information of clusters requires that some assumption be made and this assumption seemed to be a good first approach. The fraction of particles (X(i,j)) of a specific size with i charges exiting the DMA is function of the size distribution and the charge distribution. For a given burner setting and rod voltage, the fraction X(i,j) is given by

$$X(i,j) = f(d_i) \times Pc(d_i) \; / \; \Sigma \, f(d_i) \times Pc(d_i) \qquad \text{(VIII.8)}$$

$f(d_i)$ is the size frequency of a particle with a diameter d from the electrical mobility equivalent diameter size distribution. $Pc(d_i)$ is the charge probability of an agglomerate with an electrical mobility equivalent diameter of d and a net charge of i. Thus, for a given acetylene flow rate and rod voltage, the values of X(i,j) can be calculated.

The series equation VIII.7 is truncated after 4 terms because of the very low charge probability of particles with net charges greater than 4.

Table VIII.1 gives the acetylene flow rate, rod voltage setting, measured mass mean diameter and the predicted mass mean diameter. The results are also presented in a scatter plot. Figure VIII.5 shows the measured values of the mass mean diameter plotted against the predicted values. In almost every case, the calculated values

Acetylene Flow Rate (cc/min)	Rod Voltage (volts)	Measured Dve_m (μm)	Predicted Dve_m (μm)
39.5	500	0.117	0.121
-	750	0.141	0.139
-	1000	0.161	0.151
-	1500	0.180	0.168
-	3000	0.230	0.203
43.3	1000	0.193	0.169
-	1500	0.22	0.19
-	3000	0.25	0.214
67.5	1000	0.21	0.17
-	3000	0.25	0.22

Table VIII.1. Predicted mean volume equivalent diamter (Dve_m) of electrical mobility classified agglomerates.

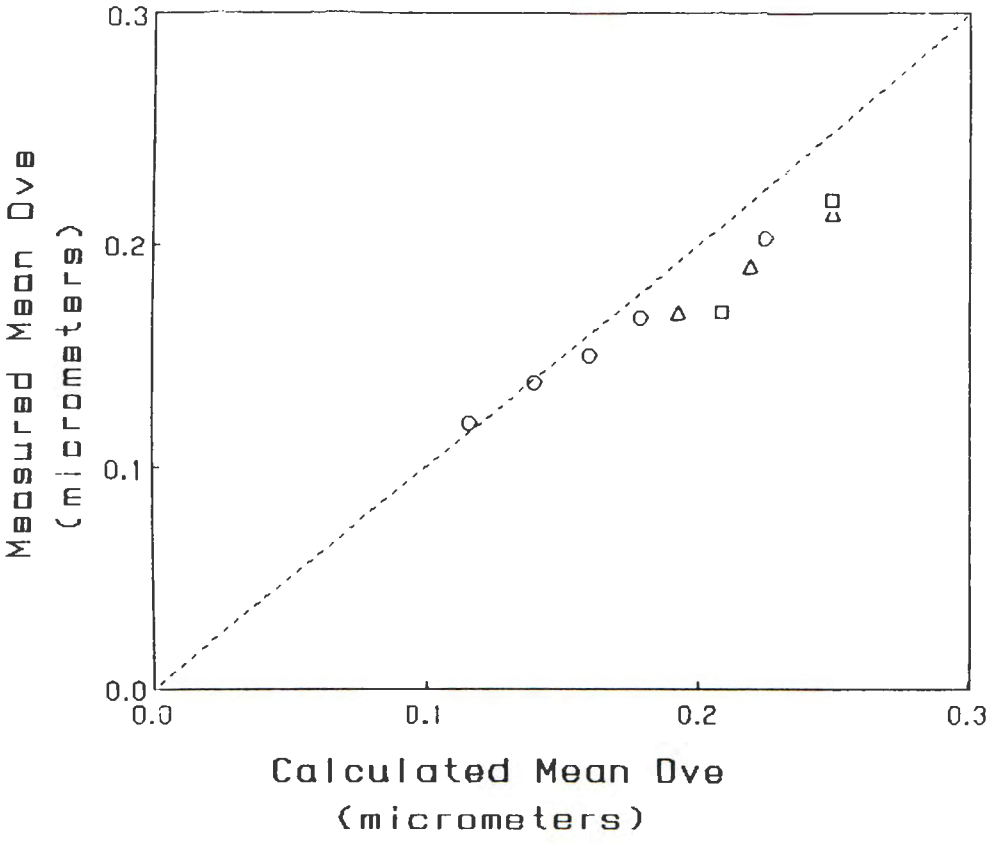

Figure VIII.5. The measured mass equivalent diameter versus the predicted mass equivalent diameter for electrical mobility classified agglomerates. The circles, triangles and squares correspond to acetylene flow rates of 39.5, 43.3, and 67.5 cc/min.

under-predict the measured values. The error from the truncation of the series expression VIII.7 is estimated to be very small due to the extremely small charging probability for particles with five or greater net charges. There is some uncertainty with the calibration curve relating the friction coefficient and the volume equivalent diameter, but it is probably within 15%. Perhaps the largest uncertainty comes from the charge distribution assumption. This calculation can be updated when a suitable charging theory for agglomerates is developed.

VIII.6 Comparison of Measured Aerodynamic Diameters of Soot Agglomerates to Model Predictions

In section V.3, size distributions of soot agglomerates classified by inertial impaction were measured. The average geometric mean size was correlated with the aerodynamic diameter. The results indicate that the aerodynamic diameter is proportional to the geometric mean size raised to the 1.2 power, thus they are roughly proportional to one another. This is a significant result because the apparent density of the agglomerates is less than 0.1 g/cc.

A simple model for the aerodynamic behavior of agglomerates can be compared to the results above. If it were assumed that the geometric mean size could replace the diameter in equation I.5, and that mass of clusters were proportional to the geometric mean size raised to the fractal dimension, then the aerodynamic diameter can

be predicted by relating the calculated cluster relaxation time to the relaxation time of an equivalent spherical particle of unit density. If a fractal dimension of 2.0 is assumed for the agglomerates, the model predicts that the aerodynamic diameter is proportional to the square root of the geometric mean size. This prediction does not compare well with the measured values. The model calculation is plotted on the same Figure (V.15) as the measured values. The solid line is the model prediction while the dashed line passing through the data points corresponds to the measured results.

The apparent density of the impacted soot agglomerates is relatively constant over a wide range of agglomerate sizes. The apparent density decreases somewhat as the agglomerate sizes decrease. The experimental data is consistent with a Stokes drag expression using the agglomerate radius and a constant density of 0.1 g/cc.

IX. RECOMMENDATIONS

The soot generator is ideally suited for characterizing soot particles from a laminar diffusion flame. One improvement to the system would be to use a more accurate acetylene flow metering device, since the soot output and mean agglomerate size are very sensitive to the acetylene flow rate near the sooting point.

It would be interesting if the existence or absence of the nearly monodisperse particles formed at low fuel flow rates (below the sooting point) could be confirmed for other fuels such as ethylene, ethane, etc. The observation of these particles is limited to an acetylene flame. It would also be useful to have an electron micrograph of the primaries. The uniformity of the primary particle size is confirmed from the primary particles that make up individual agglomerates, but a micrograph of the primaries themselves would provide an independent check on the size and uniformity.

Information on relationship between the friction coefficient and the size of agglomerates has been obtained from the examination of electrical mobility classified agglomerates. Measurements have been limited to conditions where the mean free path of the air molecules is close to 0.06 μm. In this region, the agglomerate motion is between free molecular and continuum flow conditions. In order to study free molecular conditions, it could be possible to operate the differential mobility analyzer at low pressure. The mean free path

is inversely proportional to the pressure. If an operating pressure of the DMA is fixed at 0.1 atm, then the mean free path is approximately 600 μm and free molecular conditions are being approached.

In would be useful to investigate the charging of agglomerates to check the validity of assumptions made for the data analysis of the electrical mobility classified agglomerates, and to compare experimental data to proposed models. Experimental measurements of the average charge of electrical mobility classified agglomerates, along with electron microscopy of the agglomerates, would provide useful information on the steady state charge distribution. Odumade (1983) has measured the neutral charge fraction electrical mobility classified propane smoke agglomerates. His results ar a good starting point for the investigation agglomerate charging.

An elutriator could be used to examine the aerodynamic diameters of large agglomerates. An elutriator is made up of many tubes. The flow field is well defined. The agglomerates will settle to the tube surface provided the residence time in the tube is sufficiently long. The agglomerates that penetrate the tubes would give information on the maximum size that can exit for a given residence time, which could be related to the an aerodynamic diameter. The elutriator results and the results from the size distribution of impacted agglomerates could be compared. The particles in the elutriator are not subjected to the high velocities that can be achieved in the impactor orifices.

X. REFERENCES

1. Bartz, H., Fissan, H., and Helsper, C., J. Aerosol Science, 16, n5, 443, 1985.
2. Brown, K.E., Beyer, J., and Gentry, J.W., J. Aerosol Science, 15, n2, 133, 1984.
3. Brown, K.E., and Gentry, J.W., J. Aerosol Science, 15, n3, 252, 1984.
4. Burtscher, H., Schmidt-Ott, A., and Siegmann, H.C., Aerosol Science and Technology, 8, n2, 125, 1988.
5. Cadle, R. D., "The Measurement of Airborne Particles", John Wiley & Sons, New York, 1975.
6. Dobbins, R.A., and Megaridis, C.M., Langmuir, 3, 254, 1987.
7. Friedlander, S.K., "Smoke, Dust and Haze", John Wiley & Sons, New York, 1977.
8. Fuchs, N.A., "The Mechanics of Aerosols", Pergamon, Oxford, 1964.
9. Gormley, R.G., and Kennedy, M., Proc. R. Ir. Acad., 52A, 163, 1949.
10. Hogg, R., and Tanis, E., "Probability and Statistical Inference", Macmillan Publishing Co., New York, N.Y., 1977.
11. Hoppel, W.A., J. Aerosol Science, 9, 41, 1978.
12. Knutson, E.O., and Whitby, K.T., J. Aerosol Science, 6, 443, 1975.
13. Kops, J., Dibbets, G., Hermans, L., and van de Vate, J.F., J. Aerosol Science, 6, 329, 1975.

14. Mandelbrot, B.B., "The Fractal Geometry of Nature", W.H. Freeman & Co., New York. N.Y., 1983.

15. Meakin, P., Donn, B., and Mulholland, G.W., Langmuir, in press.

16. Mountain, R.D., Mulholland, G.W., and Baum, H., J. Colloid Interface Sci., 114, 67, 1986.

17. Mulholland, G.W., private communication.

18. Mulholland, G.W., Samson, R.J., Mountain, R.D., and Ernst, M.H., Energy & Fuels, 2, n4, 481, 1988.

19. Odumade, O.A., Ph.D. Dissertation, University of Minnesota, 1983.

20. Kousaka, Y., Okuyama, K., and Adachi, M., Aerosol Science and Technology, 4, 209, 1985.

21. Park, Y.O., King, W.E., and Gentry, J.W., I&EC Product Research & Development, 19, 151, 1980.

22. Penner, J.E., and Molenkamp, C.R., Aerosol Science and Technology, 10, n1, 51, 1989.

22. Ranade, M.B., Werle, D.K., and Wasan , D.T., J. Colloid Interface Sci., 56, 42, 1976.

23. Rao, A.K., and Whitby, K.T., J. Aerosol Science, 9, 87, 1978.

24. Reist, P.C., Introduction to Aerosol Science, Macmillan Publishing Co., N.Y., New York, 1984.

25. Samson, R.J., Mulholland, G.W., and Gentry, J.W., Langmuir, 3, 272, 1987.

26. Santoro, R.J., Semerjain, H.G., and Dobbins, R.A., Combustion and Flame, 51, 203, 1983.

27. Santoro, R.J., and Miller, J.H., Langmuir, 3, n2, 244, 1987.

28. Small, J.A., Retorick, D.C., and Flethcer, R.A., American Association of Aerosol Research meeting , Seattle, Wash. 1987.

29. van de Vate, J.F., van Leeuwen, W.F., Plomp, A., and Smit, H., J. Aerosol Science, 11, 67, 1980.

30. Vomela, R.A., and Whitby, K.T., J. Colloid and Interface Sci., 25, 568, 1967.

31. Whitlaw-Gray, R., and Patterson, H.S., "Smoke", Arnold, London, 1932.

32. Yu, C.P., and Xu, G.B., J. Aerosol Science, 18, n4, 419, 1987.

APPENDICES

1. Diffusion Battery Data.

The following physical parameters are specified for the given diffusion battery stage. Each stage is identified by the nominal value in the leftmost column.

nominal	length (cm)	capilarry daimeter (μm)	number of capillaries
13X5X50	0.055	50	20200
25X20X50	0.20	50	116000
13X5X25	0.055	25	121000
25X10X50	0.10	50	115000
25X5X10	0.055	10	4280000

The following table lists the apparent diffusion coefficients for particles from the glass burner assembly.

Fuel (cc/min)	GCAF	Q (cc/sec)	Pt	ϕ	D (cm^2/sec)
22.5	13X5X25	22.7	.453	.164	1.78e-4
		26.0	.502	.137	1.70e-4
		30.2	.525	.125	1.81e-4
		34.0	.545	.116	1.88e-4
		13.4	.200	.386	2.47e-4
		17.2	.318	.259	2.13e-4
		24.8	.467	.156	1.85e-4
		28.3	.523	.126	1.71e-4
		34.0	.547	.115	1.87e-4
		41.0	.568	.105	2.06e-4
		22.7	.424	.181	1.97e-4
		26.5	.471	.154	1.95e-4
		30.2	.510	.133	1.92e-4
		34.0	.532	.122	1.98e-4
		17.2	.316	.262	2.15e-4
		24.8	.460	.160	1.90e-4

Fuel (cc/min)	GCAF	Q (cc/sec)	Pt	ϕ	D (cm^2/sec)
22.5	13X5X25	34.0	.540	.118	1.92e-4
		41.0	.579	.101	1.97e-4
	13X5X50	5.0	.549	.113	1.63e-4
		11.5	.690	.0591	1.95e-4
		17.2	.766	.0360	1.77e-4
		26.5	.847	.0179	1.36e-4
		32.2	.885	.0113	1.04e-4
		41.0	.902	.0088	1.03e-4
		34.0	.893	.0101	9.81e-5
		28.3	.875	.0130	1.06e-4
		22.7	.836	.0201	1.31e-4
		17.2	.787	.0308	1.52e-4
		11.8	.802	.0273	9.22e-5
		11.5	.668	.0663	2.18e-4
		5.0	.516	.130	1.86e-4
		5.0	.536	.120	1.72e-4
		11.5	.701	.0556	1.83e-4
		17.2	.754	.0392	1.93e-4
		22.7	.857	.0161	1.04e-4
		26.5	.866	.0145	1.10e-4
		32.2	.902	.0088	8.08e-5
		34.0	.919	.0065	6.31e-5
		37.5	.926	.0056	6.04e-5
		41.0	.907	.0081	9.48e-5
	25X10X50	37.5	.308	.268	2.78e-4
		34.0	.266	.308	2.90e-4
		28.3	.195	.394	3.09e-4
		24.8	.137	.490	3.37e-4
		41.0	.337	.244	2.77e-4
		32.2	.245	.331	2.94e-4
27.0	13X5X25	11.5	.142	.480	2.64e-4
		13.4	.184	.409	2.61e-4
		17.2	.296	.279	2.29e-4
		20.9	.385	.208	2.08e-4
		22.7	.424	.182	1.97e-4
		24.8	.448	.167	1.98e-4
		26.5	.473	.153	1.93e-4
		28.3	.471	.154	2.08e-4
		30.2	.498	.139	2.00e-4
		34.0	.521	.127	2.07e-4
		35.3	.554	.112	1.89e-4
		37.5	.577	.102	1.82e-4
		38.8	.568	.105	1.96e-4
		41.0	.588	.0967	1.90e-4
	13X5X50	30.2	.891	.0104	9.03e-5
		37.5	.908	.0079	8.50e-5
		26.5	.891	.0104	7.93e-5
		20.9	.838	.0200	1.18e-4
		17.2	.782	.0321	1.58e-4
		13.4	.713	.0520	1.99e-4

Fuel (cc/min)	GCAF	Q (cc/sec)	Pt	ϕ	D (cm^2/sec)
		11.5	.654	.0711	2.34e-4
		5.0	.503	.136	1.95e-4
		41.0	.908	.0793	9.31e-5
		37.5	.935	.0046	4.92e-5
		34.0	.887	.0110	1.07e-4
		32.2	.895	.0098	9.02e-5
		26.5	.894	.0099	7.54e-4
		22.7	.862	.0152	9.85e-5
		17.2	.791	.0300	1.47e-4
		11.5	.668	.0663	2.19e-4
		7.8	.619	.0842	1.87e-4
		5.0	.516	.130	1.86e-4
	25X10X50	41.0	.353	.231	2.62e-4
		30.2	.234	.343	2.87e-4
31.5	13X5X50	5.0	.532	.122	1.75e-4
		11.5	.674	.0643	2.12e-4
		17.2	.791	.0299	1.47e-4
		26.5	.878	.0124	9.44e-5
		31.7	.912	.0074	6.70e-5
		38.8	.927	.0055	6.16e-5
		37.5	.923	.0060	6.42e-5
		35.3	.920	.0064	6.47e-5
		19.7	.928	.0054	3.03e-5
		22.7	.880	.0121	7.87e-5
		17.2	.812	.0251	1.24e-4
		13.4	.759	.0380	1.45e-4
		5.0	.489	.144	2.06e-4
		5.0	.515	.130	1.87e-4
		7.8	.608	.0885	1.97e-4
		11.5	.705	.0544	1.79e-4
		17.2	.817	.0240	1.18e-4
		22.7	.874	.0131	8.51e-5
		26.5	.899	.0092	6.98e-5
		32.2	.918	.0066	6.09e-5
		34.0	.909	.0078	7.59e-5
		37.5	.921	.0062	6.69e-5
		41.0	.931	.0050	5.91e-5
	13X5X25	32.2	.570	.104	1.61e-4
		37.5	.631	.0796	1.43e-4
		30.2	.500	.138	1.99e-4
		28.3	.511	.132	1.79e-4
		26.5	.491	.143	1.81e-4
		22.7	.442	.170	1.85e-4
		17.2	.321	.257	2.11e-4
		13.4	.220	.360	2.31e-4
		11.5	.158	.451	2.48e-4
		22.7	.425	.181	1.96e-4
		24.8	.444	.169	2.01e-4
		26.5	.472	.153	1.94e-4
		28.3	.490	.143	1.94e-4
		30.2	.512	.132	1.91e-4

Fuel (cc/min)	GCAF	Q (cc/sec)	Pt	ϕ	D (cm^2/sec)
		32.2	.527	.124	1.91e-4
		11.5	.170	.431	2.37e-4
		13.4	.236	.341	2.18e-4
		17.2	.349	.234	1.92e-4
		22.7	.460	.160	1.74e-4
	25X10X50	32.2	.280	.294	2.62e-4
		34.0	.313	.264	2.48e-4
		35.3	.323	.255	2.49e-4
		37.5	.343	.239	2.48e-4
		38.8	.359	.226	2.43e-4
37.0	25X10X50	13.4	.0963	.586	2.17e-4
		22.7	.198	.389	2.44e-4
		30.2	.284	.290	2.42e-4
		41.0	.375	.215	2.44e-4
	13X5X25	22.7	.488	.144	1.57e-4
		20.9	.442	.171	1.71e-4
		17.2	.402	.196	1.61e-4
		13.4	.260	.315	2.01e-4
		24.8	.485	.146	1.73e-4
		26.5	.506	.135	1.71e-4
		28.3	.525	.125	1.70e-4
		30.2	.537	.120	1.72e-4
		32.2	.563	.108	1.66e-4
		34.0	.583	.0990	1.61e-4
		35.3	.585	.0980	1.65e-4
		41.0	.604	.0900	1.76e-4
	13X5X50	41.0	.902	.0087	1.02e-4
		37.5	.912	.0074	7.96e-5
		32.2	.875	.0129	1.19e-4
		28.3	.894	.0099	8.06e-5
		24.8	.850	.0174	1.24e-4
		20.9	.829	.0216	1.29e-4
		17.2	.781	.0323	1.59e-4
		13.4	.716	.0509	1.95e-4
		11.5	.662	.0684	2.25e-4
		5.0	.549	.114	1.63e-4
		41.0	.925	.0057	6.74e-5
		37.5	.939	.0041	4.46e-5
		34.0	.845	.0183	1.78e-4
		26.5	.886	.0111	8.47e-5
		22.7	.846	.0181	1.18e-4
		17.2	.783	.0318	1.56e-4
		11.5	.667	.0667	2.20e-4
		7.8	.621	.0834	1.86e-4
		5.0	.527	.124	1.78e-4
Brass burner configuation					
22.5	13X5X25	22.7	.213	.369	4.00e-4
		32.2	.288	.287	4.41e-4
		37.5	.301	.274	4.92e-4
		15.2	.095	.590	4.28e-4
	13X5X50	41.0	.732	.0464	5.45e-4

Fuel (cc/min)	GCAF	Q (cc/sec)	Pt	ϕ	D (cm^2/sec)
		32.2	.681	.0620	5.71e-4
		22.7	.570	.104	6.78e-4
		22.7	.623	.0826	5.37e-4
		44.3	.744	.0430	5.47e-4
		49.8	.807	.0262	3.74e-4
		55.0	.790	.0301	4.75e-4
		19.0	.557	.110	6.00e-4
		14.3	.513	.131	5.39e-4
		9.5	.514	.131	3.56e-4
		5.0	.269	.305	4.37e-4
		22.7	.222	.358	3.88e-4
28.0	13X5X25	32.2	.303	.273	4.19e-4
		37.5	.331	.249	4.46e-4
		15.2	.098	.582	4.22e-4
		22.7	.115	.538	5.84e-4
		22.7	.113	.543	5.89e-4
		17.7	.0761	.651	5.50e-4
		17.7	.0798	.638	5.39e-4
		13.3	.0342	.870	5.55e-4
		13.3	.352	.862	5.50e-4
		9.5	.0071	1.30	5.91e-4
		9.5	.0069	1.31	5.94e-4
		5.0	.00034	2.13	5.10e-4
		41.0	.732	.0464	5.45e-4
	13X5X50	32.2	.681	.0620	5.71e-4
		22.7	.570	.104	6.78e-4
		22.7	.671	.0653	4.24e-4
		44.2	.776	.0335	4.26e-4
		49.8	.762	.0371	5.30e-4
		55.0	.827	.0220	3.45e-4
		19.0	.579	.100	5.47e-4
		14.3	.523	.126	5.18e-4
		9.5	.514	.131	3.56e-4
		5.0	.280	.294	4.21e-4
		22.7	.249	.326	3.54e-4
31.5	13X5X25	32.2	.303	.273	4.19e-4
		37.5	.365	.222	3.98e-4
		15.2	.110	.550	3.99e-4
		22.7	.158	.450	4.88e-4
		22.7	.148	.470	5.09e-4
		32.0	.276	.298	4.56e-4
		32.0	.274	.301	4.60e-4
		17.7	.0987	.580	4.90e-4
		17.7	.0980	.582	4.92e-4
		15.2	.0654	.692	5.02e-4
		15.2	.0667	.687	4.98e-4
		13.3	.0361	.855	5.45e-4
		13.3	.0349	.865	5.51e-4
		11.5	.0211	1.00	5.51e-4
		11.5	.0200	1.02	5.59e-4
		9.5	.0094	1.22	5.56e-4

Fuel (cc/min)	GCAF	Q (cc/sec)	Pt	ϕ	D (cm^2/sec)
		9.5	.0091	1.23	5.60e-4
		27.5	.214	.368	4.84e-4
		27.5	.211	.372	4.89e-4
	13X5X50	41.0	.789	.0304	3.57e-4
		32.2	.748	.0419	3.87e-4
		22.7	.631	.0800	5.17e-4
		22.7	.698	.0565	3.67e-4
		44.3	.791	.0299	3.80e-4
		49.8	.775	.0338	4.82e-4
		55.0	.830	.0213	3.35e-4
		19.0	.605	.0900	4.88e-4
		14.3	.566	.106	4.36e-4
		9.5	.545	.116	3.16e-4
		5.0	.300	.275	3.94e-4
33.5	13X5X25	22.7	.237	.340	3.68e-4
		32.2	.301	.274	4.22e-4
		37.5	.365	.222	3.98e-4
		15.2	.110	.550	3.99e-4
	13X5X50	41.0	.783	.0318	3.74e-4
		32.2	.703	.0550	5.07e-4
		22.7	.580	.100	6.50e-4
		22.7	.668	.0663	4.31e-4
		44.3	.747	.0422	5.36e-4
		49.8	.785	.0313	4.47e-4
		55.0	.783	.0318	5.01e-4
		19.0	.558	.110	5.97e-4
		14.3	.508	.134	5.49e-4
		9.5	.501	.137	3.74e-4
		5.0	.283	.291	4.17e-4
36.0	13X5X25	22.7	.236	.341	3.70e-4
		32.2	.268	.306	4.71e-4
		37.5	.282	.292	5.24e-4
		15.2	.164	.441	3.20e-4
		22.7	.178	.418	4.53e-4
		22.7	.178	.418	4.53e-4
		32.0	.291	.283	4.34e-4
		32.0	.299	.276	4.23e-4
		17.7	.148	.468	3.96e-4
		17.7	.135	.494	4.17e-4
		15.2	.145	.474	3.44e-4
		15.2	.128	.508	3.68e-4
		13.3	.114	.539	3.44e-4
		13.3	.120	.526	3.36e-4
		11.5	.0749	.655	3.60e-4
		11.5	.0636	.700	3.85e-4
		9.5	.0482	.776	3.53e-4
		5.0	.0225	.985	2.36e-4
		5.0	.0208	1.00	2.41e-4
	13X5X50	41.0	.714	.0516	6.07e-4
		32.2	.789	.0304	2.80e-4
		22.7	.673	.0646	4.20e-4

Fuel (cc/min)	GCAF	Q (cc/sec)	Pt	ϕ	D (cm^2/sec)
		22.7	.697	.0568	3.69e-4
		44.3	.835	.0203	2.57e-4
		49.8	.801	.0276	3.93e-4
		55.0	.849	.0175	2.77e-4
		19.0	.665	.0674	3.67e-4
		14.3	.620	.0838	3.44e-4
		9.5	.600	.0917	2.50e-4
		5.0	.289	.286	4.09e-4

2. Impactor Calibration

A calibration of the NIST Anderson model 2000 cascade impactor was performed using a vibrating orifice aerosol generator (VOAG, model 3450, TSI, St. Paul, Minn.) with oleic acid particles tagged with a fluorescein tracer. A solution containing 400 ml of isopropyl alcohol , 0.25 ml of oleic acid, and 115mg of fluorescein was prepared. This solution will produce particles around 4 μm in diameter. The 20 μm orifice was used with the frequency set at 46.25 kHz. The particles produced are monodisperse. The particles were independently sized using a gravitational settling chamber. The settling time for a specified distance gives the terminal settling velocity which is related to the particle diameter. The mean settling time corresponds to a 3.8 μm in diameter particle. The particles from the VOAG were sent to the impactor. Sampling time was one hour and the impaction surface was un-coated aluminum foil. The mass concentration on each stage was determined by washing the stage with a known volume of weak sodium hydroxide solution. The light transmittance of the solution was recorded with a spectrometer and compared to a calibration curve. This data was reduced using both Whitbys and the Anderson values for the 50% cutoff diameters. Figure A.1 shows the results plotted on log probability paper. The mass median diameter obtained from the 50% probability line is 3.95 μm using Whitbys cutoff diameters and 3.45 using the Anderson cutoff diameters. Whitbys values agree much better with the measured particle diameter of 3.8 μm. A small

fraction of particles may have coalesced which would account for the slight overestimation of the monodisperse size.

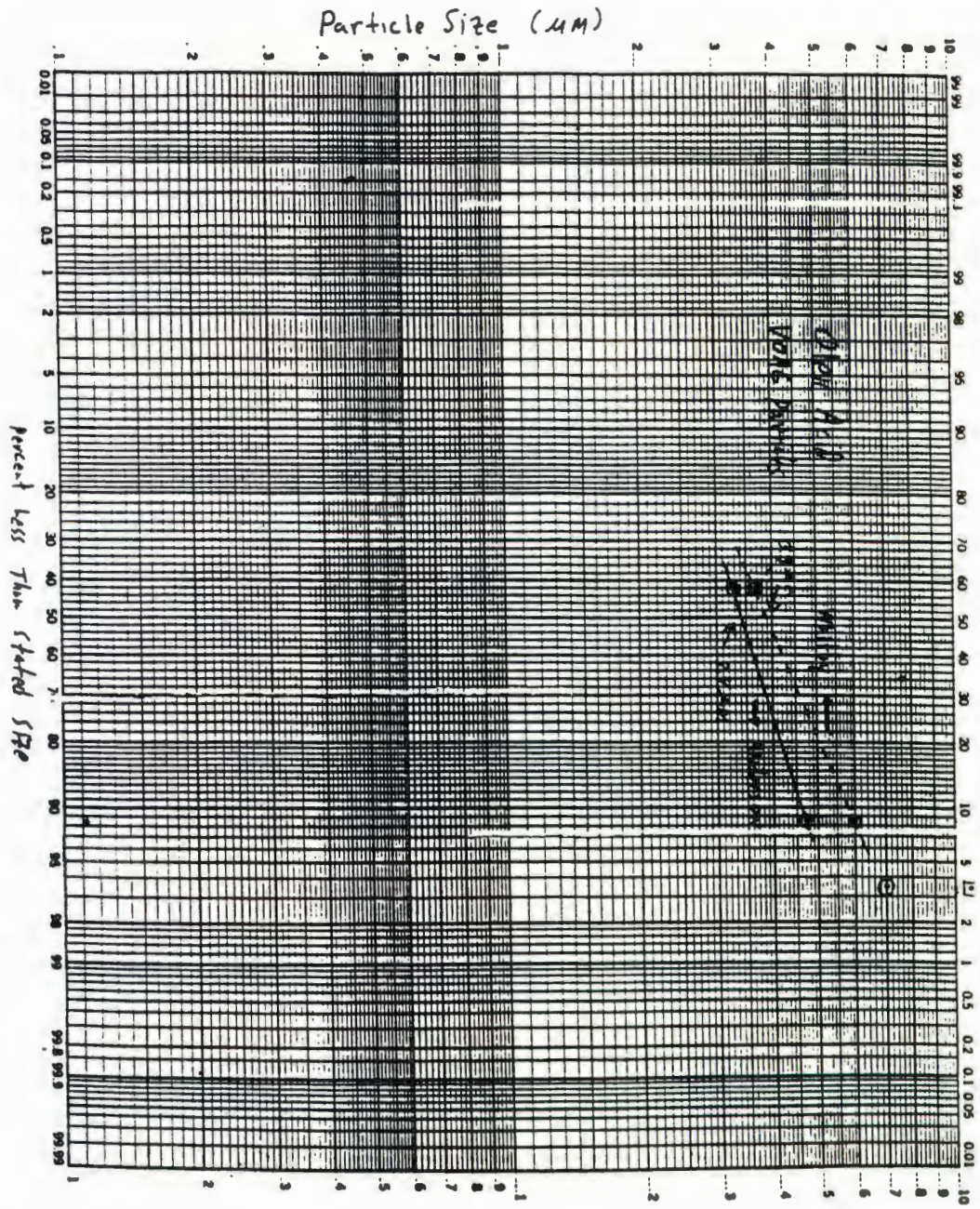

Figure A.1 50% cutoff size vs. the mass percent less than the stated size. Upper line is Whitbys values, lower line Anderson values.